UC Irvine
UC Irvine Electronic Theses and Dissertations

Title
Microfabricated Platforms for Microassembly of Inorganic/Organic/Biological System

Permalink
https://escholarship.org/uc/item/8rz3k9dj

Author
Zhou, Tuo

Publication Date
2022

Supplemental Material
https://escholarship.org/uc/item/8rz3k9dj#supplemental

Peer reviewed|Thesis/dissertation

eScholarship.org Powered by the California Digital Library
University of California

UNIVERSITY OF CALIFORNIA,
IRVINE

Microfabricated Platforms for Microassembly of Inorganic/Organic/Biological System

DISSERTATION

submitted in partial satisfaction of the requirements
for the degree of

DOCTOR OF PHILOSOPHY

in Engineering

by

Tuo Zhou

Dissertation Committee:
Professor Lorenzo Valdevit,Co-chair
Professor Lawrence Kulinsky,Co-chair
Professor James Earthman

2022

Photographs in Introduction © CRC Press
Chapter 2 © American Chemical Society
Chapter 3,4,5 © MDPI
© 2022 Tuo Zhou

DEDICATION

To

my parents and friends

Table of Contents

LIST OF FIGURES vi

LIST OF TABLES ix

ACKNOWLEDGEMENTS x

VITA xi

ABSTRACT OF THE DISSERTATION xvi

Chapter 1 1

Background 1

1.1 Carbon Allotropes 1

1.2 Carbon MEMS 5

1.3 Photolithography 7

1.4 Microassembly 12

1.5 Dielectrophoresis (DEP) 14

1.6 Electroosmosis (EO) 16

Chapter 2 17

Guided Electrokinetic Assembly of Polystyrene Microbeads onto Photopatterned Carbon Electrode Arrays 17

2.1: Introduction 17

2.2 Materials and Methods 18

2.3 Results 21

2.31 Steps of Template Electrokinetic Assembly. 21

2.32: Movement of 5 µm Beads under DEP. 25

2.33: Movement of 1 µm Beads under the Influence of Electro-osmosis 26

2.34: Template Electrokinetic Microassembly of 5 µm Beads inside Windows. 29

2.35. Permanent Entrapment of the Beads with Polypyrrole. 30

2.36 The Entrapment of Fluorophore Conjugated Beads 33

Chapter 3 35

Characterization of the Positive and Negative Dielectrophoretic Ranges of Applied Frequency 35

3.1: Introduction. 35

3.2 Materials and Methods 37

3.21 Interdigitated Electrode Fabrication 37

3.22 Experimental Setup 38

3.3. Software Architecture and Methodology 40

3.31 Architecture Overview 40
3.32 Particle Detection and Feature Extraction 41
3.33 Particle Movement Determination 42
3.34: Feedback Control Design 44
3.4 Results 45
3.41 Particle Detection 45
3.42 Bulk Cloud Behavior 48
3.43 Individual Particle Behavior 50
3.44. Correlation of Bead Cloud Behavior and Individual Bead Position 53
3.441. Bulk Motion 53
3.442 Regions of DEP Influence 54
3.45 Beads to Bead Interaction 55
Chapter 4 57
Step-Wise Deposition Process for Dielectrophoretic Formation of Conductive 50-micron-Long Carbon Nanotube Bridges 57
4.1 Introduction 57
4.2 Materials and Methods 58
4.21. Fabrication of IDEAs 58
4.22 Preparation of Carbon Nanotube Suspension 60
4.23.Preparation of Pyrrole Solution 60
4.24. Deposition of CNT bridges, Resistance Measurement, and Heat Treatment 61
4.25 Polypyrrole (PPy) Deposition 61
4.26: Finite Element Analysis Multiphysics Simulation 62
4.3 Results and Discussion 63
4.31 Continuous vs. Step-wise CNT Bridge Formation 63
4.32. Applied Frequency Influence on the Morphology of CNT Bridges 66
4.33 Influence of Postdeposition Heat Treatment on Resistance of CNT Bridges 69
4.34 PPy Deposition over CNT Bridges 73
Chapter 5 76
Guided Healing of Damaged Microelectrodes via Electrokinetic Assembly of Conductive Carbon Nanotube Bridges 76
5.1 Introduction 76
5.2 Materials and Methods 77
5.21 Fabrication of Carbon Electrodes 77

5.22: Preparation of Carbon Nanotube Suspension 79
5.23: Experimental Setup and Deposition of Carbon Nanotube Suspension........ 79
5.24 Preperation of Pyrrole Solution........ 80
5.25. Polypyrrole Deposition........ 81
5.26. Stress-Testing of Carbon Nanotube (CNT) Bridges........ 82
5.27. Finite Element Analysis of Electric Field Magnitude........ 82
5.3 Results........ 83
5.31. CNT Bridges across 20, 30 and 40 μm Electrode Gaps........ 83
5.311. Assembly of CNT Bridges 83
5.312: Resistance of CNT Bridges 85
5.313: Electric Field Strength Simulation........ 87
5.314. CNT Bridge across the Fractured Electrode 88
5.315. Deposition of Polypyrrole 89
5.32. Results of the Stress Testing of the Formed CNT Bridges........ 92
5.321. Thermal Cycling 92
5.322: Placing the Healed Microelectrodes under Running Water 93
5.323: Exposure of the Healed Microelectrodes to Blasts of Compressed Nitrogen Gas........ 93
Chapter 6........ 95
Conclusion........ 95
6.1: Guided Microassembly of Latex Microbeads 95
6.2: Automatically Determination of the Cross-over Frequency........ 96
6.3: Step-wise Deposition of CNT........ 97
6.4: Guided healing of damaged microelectrode via assembly of CNT 98
Bibliography 100

LIST OF FIGURES

FIGURE 1: CRYSTAL STRUCTURE OF THE MAIN ALLOTROPES OF CARBON [6] 2
FIGURE 2: STRUCTURAL MODELS DESCRIBING THE STRUCTURE OF GLASSY CARBON[13]: (A) FRANKLIN MODEL; (B) RIBBON-LIKE MODEL[14]; (C) BAN MODEL [15]; (D) CLOSED-LIKE GRAPHITIC STRUCTURE[16]; (E) (F)THE FULLERENE-RELATED STRUCTURAL MODEL [17]; 3
FIGURE 3: SCHEMATIC REPRESENTATIONS OF THE FORMATION (A) AND STRUCTURE OF CNT (B)[10]. 4
FIGURE 4: THE PROCESS OF CONVENTIONAL PHOTOLITHOGRAPHY[44]. 8
FIGURE 5: (A) SCHEMATICS OF THE IDEA CHIP WITH POLYMER CAGE CREATED FROM DOUBLE-STICK TAPE AND COVERED BY THE GLASS SLIDE; (B) SKETCH OF THE INTERDIGITATED ELECTRODE ARRAYS; (C) OPTICAL MICROGRAPH OF THE ELECTRODE FINGERS COVERED WITH SQUARE WELLS OPENED IN THE PHOTORESIST[81]. 19
FIGURE 6: PROCESS OF TEMPLATE ELECTROKINETIC ASSEMBLY (TEA) OF (A) 5 μM AND (B) 1 μM POLYSTYRENE MICROBEADS[81]. 23
FIGURE 7: (A) PATTERNS FORMED BY 5 μM PARTICLES UNDER THE EFFECT OF NDEP UNDER 1 MHZ, 4 VPP AC BIAS; (B) COMSOL SIMULATION RESULTS REFLECT THE COMBINATION OF GRAVITATIONAL SEDIMENTATION AND NDEP ON POLYSTYRENE BEADS AND EXPLAINS THE FORMATION OF THE OBSERVED INITIAL BEAD PATTERN[81]. 24
FIGURE 8: (A) 1 MM POLYSTYRENE BEADS ARE PUSHED TOGETHER UNDER THE INFLUENCE OF ELECTRO-OSMOSIS INSIDE THE WELLS AT 3 VPP AS THE APPLIED FREQUENCY IS DECREASED FROM 10 KHZ TO 50 HZ. (B) FREQUENCY AND VOLTAGE DEPENDENCE OF THE 1 MM POLYSTYRENE BEAD CLUSTERS IN 100 μM WINDOWS. (C) COMSOL MODEL OF EO STREAMLINES AROUND THE RESIST WINDOW[81]. 28
FIGURE 9: (A) COMSOL SIMULATION RESULT DEMONSTRATING TWO AREAS OF HIGH ELECTRIC FIELD GRADIENTS: AROUND THE EDGES OF RESIST WINDOWS AND AROUND THE PARTICLE CLUSTER INSIDE THE WINDOW; (B) A SERIES OF OPTICAL MICROGRAPHS TRACING THE MOVEMENT OF 5 μM BEAD TOWARD THE CLUSTER OF 5 μM BEADS INSIDE THE WELL UNDER 1 KHZ, 3 VPP BIAS. (C) COMSOL MODEL OF EO STREAMLINES AROUND THE RESIST WINDOW AND CLUSTER OF THE BEADS INSIDE THE WINDOW; (D) ATTRACTION OF 5 μM PARTICLES BY THE CLUSTER OF 1 μM PARTICLES INSIDE THE WELLS[81]. 31
FIGURE 10: MECHANISM OF THE GUIDED ELECTROKINETIC ASSEMBLY FOR 5 μM MICROPARTICLES. THE SCHEMATICS REPRESENTS A CROSS-SECTION OF THE IDEA CHIP WHERE THE CARBON ELECTRODES ARE BLACK, RESIST IS GRAY, AND THE DEP FORCES ARE REPRESENTED BY RED ARROWS AND ELECTRO-OSMOTIC FORCES BY BLUE ARROWS. (A) CLUSTERING OF THE 5 μM BEADS UNDER THE INFLUENCE OF N-DEP FORCES. (B) SCHEMATICS OF THE BEADS' MOTION UNDER P-DEP FORCES AND ELECTRO-OSMOTIC (EO) FORCES THAT BECOME SIGNIFICANT UNDER THE LOW APPLIED FREQUENCY. ZONE 1 IS THE LOCAL MAXIMUM OF IDEP FORCES AT THE INNER EDGE OF THE RESIST WELL, ZONE 2 IS THE LOCAL MAXIMUM OF IDEP FORCES AROUND THE OUTER EDGE OF THE RESIST WELL, WHEREAS ZONE 3 IS THE LOCAL MAXIMUM FOR IDEP FORCES BECAUSE OF CLUSTERING OF THE POLYSTYRENE BEADS INSIDE THE WELLS[81]. 32
FIGURE 11: ENTRAPMENT OF BEADS BY PPY DEPOSITION. (A) OPTICAL IMAGE OF THE IDEA WITH THE POLYSTYRENE BEADS ENTRAPPED BY PPY; (B) SCANNING ELECTRON MICROSCOPY (SEM) IMAGE OF 1

μM BEAD AGGLOMERATE COVERED WITH PPY; (C) CLOSE-UP OF THE WELL WITH PPY-ENTRAPPED 1 μM BEADS; (D) CLOSE-UP OF THE WELL WITH PPY-ENTRAPPED 5 μM BEADS[81]. 33
FIGURE 12: ENTRAPMENT OF FLUOROPHORES CONJUGATED BEADS BEFORE (A) AND AFTER (B) ATTRACTION; (C) THE ABSOLUTE VALUE OF CORRECTED TOTAL CELL FLUORESCENCE (CTCF) BEFORE AND AFTER ENTRAPMENT. 34
FIGURE 13: THE SCHEMATIC OF THE IEDA. THE GOLD ELECTRODE FINGERS (LIGHT AGAINST THE DARK BACKGROUND OF THE SUBSTRATE) HAVE THE SPACING BETWEEN THE ADJACENT FINGERS OF 70 μM. 38
FIGURE 14: SKETCH OF THE EXPERIMENTAL SETUP INCLUDING IDEAS CONNECTED TO A FUNCTION GENERATOR. 39
FIGURE 15: ARCHITECTURE OF THE FEEDBACK CONTROL SYSTEM DESIGN 41
FIGURE 16: EXAMPLES (A) AND (B) OF BEAD DETECTION USING THE HOUGH CIRCLE DETECTION FUNCTION OF THE OPENCV PACKAGE. THE RECOGNIZED BEADS ARE CIRCLED IN RED. THE GREEN LINES IDENTIFY THE FRAME WINDOW NEARLY COINCIDENT WITH THE EDGES OF THE ELECTRODES 46
FIGURE 17: DIFFERENT BEAD DETECTION EFFICACY BETWEEN SAMPLES (A) AND (B) DEPENDED ON BEAD SIZE AND ILLUMINATION CONDITIONS. 47
FIGURE 18: AVERAGE ABSOLUTE DISTANCE FROM CENTER BY FRAME (TRIAL 1). 48
FIGURE 19: AVERAGE ABSOLUTE DISTANCE FROM CENTER BY FRAME (TRIAL 2). 49
FIGURE 20: INDIVIDUAL BEAD MOVEMENT DURING TRIAL 2 FROM FRAMES 195 TO 298. 50
FIGURE 21: INDIVIDUAL BEAD MOVEMENT DURING TRIAL 2 FROM FRAMES 300 TO 340. 51
FIGURE 22: INDIVIDUAL BEAD MOVEMENT DURING TRIAL 2 FROM FRAMES 570 TO 685. 52
FIGURE 23: INDIVIDUAL BEAD MOVEMENT DURING TRIAL 2 FROM FRAMES 735 TO 812. 52
FIGURE 24: PEARL CHAIN FORMATION AS A RESULT OF BEAD-TO-BEAD INTERACTION. 56
FIGURE 25: EXPERIMENTAL SETUP (LEFT) AND INTERDIGITATED ARRAY OF CARBON ELECTRODE FINGERS 120 MICRON WIDE WITH 120 MICRONS INTER-ELECTRODE SPACING (RIGHT). 59
FIGURE 26: CAD DRAWINGS OF THE INTERDIGITATED ELECTRODE ARRAYS (IDEA) USED IN COMSOL SIMULATION: SIDE VIEW (A) AND TOP VIEW (B). 63
FIGURE 27: COMPARISON BETWEEN THE CNT BRIDGES FORMED BY STEP-WISE PROCEDURE (A) AND THE CNT BUNDLES ATTRACTED BY THE ONE-STEP PROCEDURE (B). BOTH DEPOSITION PROCEDURES USED AN AC 5 VPP BIAS AT 100 KHZ. 65
FIGURE 28: COMSOL SIMULATION OF ELECTRIC FIELD INTENSITY AROUND THE END OF CNTS IN THE STEP-WISE CNT BRIDGE FORMATION PROCESS. (A) FIELD DISTRIBUTION NEAR AN INDIVIDUAL CNT BUNDLE (B) RESULTS OF THE SIMULATION SHOW THAT DURING BRIDGE FORMATION, REGIONS OF HIGHEST FIELD INTENSITY SHIFT FROM THE EDGES OF ELECTRODES TO THE ENDS OF THE CNT BRIDGES. 65
FIGURE 29: CNT BRIDGES DEPOSITED UNDER 5 VPP AC BIAS AT 1 KHZ, 10 KHZ, 100 KHZ, 1 MHZ, AND 10 MHZ APPLIED FREQUENCIES. 67
FIGURE 30: THE SEM IMAGES OF CNT BRIDGES DEPOSITED UNDER 100 KHZ FREQUENCY. (A, B) SEM IMAGES OF ELECTRODES AT 1530 AND 1525 MAGNIFICATION, RESPECTIVELY; (C) SEM IMAGE OF THE EDGE OF ELECTRODE AT 5000 MAGNIFICATION. 68
FIGURE 31: THE FLOW CHART OF THE EXPERIMENTAL PROCEDURE. 71
FIGURE 32: THE RESISTANCE OF CNT BRIDGES OF SAMPLE 1 (A) AND SAMPLE 2 (B) AS FUNCTION OF DEPOSITION PARAMETER AND POSTDEPOSITION HEAT TREATMENT INCLUDING AFTER CNT DEPOSITION

(R1), drying on hot plate for 20 min at 200 °C (R2), after polypyrrole deposition (R3), and after final drying on hot plate for 20 min at 200 °C (R4)35 72
Figure 33: The illustration of the influence of postdeposition heat treatment on CNT bridges. (a) Remaining droplets present after blow drying keep CNTs separated; (b) Evaporation of remaining solvent after heat treatment and the resulting changes in surface tension act to pull CNTs together, improving CNT-CNT contact. 73
Figure 34: The CNT bridges after electrodeposition of PPy. 74
Figure 35: The illustration of the influence of heat treatment on CNT bridges after PPy deposition. (a) PPy deposition envelops CNT bridges with remaining solvent after blow drying (b) Less dramatic changes in resistance were observed before and after the final heat treatment. This is attributed to the PPy layer which prevents complete evaporation of solvent. 75
Figure 36: (a) Carbon nanotube (CNT) electrokinetic assembly experimental setup design. (b) Dimensions of the carbon electrodes. 80
Figure 37: Electrodes with 20 μm gap (a) before CNT deposition; (b) after 2 μL of CNT suspension; (c) after 4 μL of CNT suspension; (d) after 5 μL of CNT suspension. 83
Figure 38: Electrodes with 30 μm gap (a) before CNT deposition; (b) after 3 μL of CNT suspension; (c) after 7 μL of CNT suspension; (d) after 10 μL of CNT suspension. 84
Figure 39: Electrodes with 40 μm gap (a) before CNT deposition; (b) after 5 μL of CNT suspension; (c) after 7 μL of CNT suspension; (d) after 10 μL of CNT suspension. 84
Figure 40: Scanning electron microscope (SEM) pictures of the CNT bridges formed across (a) 20 μm electrode gap (b) 30 μm electrode gap (c) 40 μm electrode gap. 85
Figure 41: Plot of the measured resistance of the healed electrodes as function of CNT bridge length. 86
Figure 42: Simulation across electrode gap lengths of (a) the electric field strength (b) the gradient of the square of the electric field strength. 88
Figure 43: Fractured electrode (a) before CNT deposition; (b) after deposition of 7 μL of CNT suspension; (c) after 15.5 μL of CNT suspension; (d) after 19 μL of CNT suspension; and (e) after 23 μL of CNT suspension. 89
Figure 44: Results of polymer polypyrrole (PPy) deposition over the CNT bridge spanning 20 mm electrode gap without switching the polarity of 0.9 Vpp DC bias captured at approximately (a) 25% completion (b) 50% completion (c) 100% completion. 90
Figure 45: Results of PPy deposition over the CNT bridge spanning 20 mm electrode gap (a) prior to PPy application; (b) after the PPy deposition from the side of the top electrode reached roughly half-way through the CNT bridge and the polarity of the 0.9 Vpp DC bias was switched; (c) completion of PPy deposition over the CNT bridge. 91
Figure 46: Results of the PPy deposition onto the CNT bridge of the healed electrode that contained a wide fracture (a) after the initial PPy deposition from the bottom electrode at 0.9 Vpp DC bias; (b) after the polarity of the DC bias was reversed. 91

LIST OF TABLES

TABLE 1: PSEUDO CODE GOVERNING THE CONTROL LOOP 45
TABLE 2: RESISTIVITIES OF SAMPLES 1 AND 2 SHOWING MEAN VALUES AND STANDARD DEVIATION AFTER CNT DEPOSITION (CNT), DRYING ON HOT PLATE FOR 20 MIN AT 200 °C (CNT + HT), POLYPYRROLE DEPOSITION (CNT + HT + PPY), AND FINAL DRYING ON HOT PLATE FOR 20 MIN AT 200 °C (CNT + HT + PPY + HT). 70
TABLE 3: RESISTANCE MEASURED ACROSS THE ELECTRODE WITH 30 μM GAP AFTER DEPOSITION AND DRYING OF EVERY TWO 0.5 μL DROPLETS OF CNT SUSPENSION. 85
TABLE 4: RESISTANCE OF MICROELECTRODE BEFORE AND AFTER FRACTURE AND RESISTANCES OF HEALED 20, 30, AND 40 μM GAP ELECTRODES. 86
TABLE 5: RESISTANCE MEASUREMENTS BEFORE AND AFTER THERMAL CYCLING 92
TABLE 6: RESISTANCE MEASUREMENTS BEFORE AND AFTER PLACING THE HEALED ELECTRODES UNDER THE DEIONISED WATER (DI) WATER STREAM. 93
TABLE 7: RESISTANCE MEASUREMENTS BEFORE AND AFTER BLOWING COMPRESSED NITROGEN OVER THE SAMPLES OF HEALED MICROELECTRODES. 93

ACKNOWLEDGEMENTS

I want to take this opportunity to express my deepest appreciation to my research advisor, Professor Lawrence Kulisnsky, who has provided me with his continual guidance and research mentorship, helped me publish many well-received publications, and aided me in earning two prestigious scholarships. Without him, it would be impossible for me to advance to my PhD.

I also want to thank my committee members, Professor Lorenzo Valdevit and Professor James Earthman, who provided valuable advice and inspired me to succeed in my research. This work has been made stronger by their support and critical suggestions.

In addition, I want to express my most profound appreciation to my parents, whose unconditional support is why I wanted to do research in the first place. They never asked me to do what they believed was good for me. Instead, they let me decide what I wanted to do. They are the greatest parents in the world, and I'm so proud of them.

Support for the microassembly-related studies is provided by the National Science Foundation (NSF) grant (Award CMMI-1661877). I also would like to thank the UC Irvine Material Research Institute (IMRI) for giving me access to their characterization equipment and to thank UC Irvine Integrated Nanofabrication Research Facility (INRF)/ BiON for enabling me to perform the required microfabrication in their fantastic clean-room facility.

I appreciate the American Chemical Society for granting me permission to reuse and incorporate my work "Guided Electrokinetic Assembly of Polystyrene Microbeads onto Photopatterned Carbon Electrode Arrays," published in ACS Appl. Mater. Interfaces, into this dissertation, the co-authors listed in this publication are Jingyuan Chen and Ethan Kropp. The text of chapter two of this dissertation is a reprint of this publication.I also want to thank MDPI for letting me reuse and incorporate my works published on Micromachines. The first one is "Step-Wise Deposition Process for Dielectrophoretic Formation of Conductive 50-Micron-Long Carbon Nanotube Bridges", the co-authors listed in this paper are Jingyuan Chen and Ethan Kropp, chapter four of this dissertation a reprint of this publication. The second one is "Guided Healing of Damaged Microelectrodes via Electrokinetic Assembly of Conductive Carbon Nanotube Bridges", the co-authors listed in this paper is Matthew Michaels, chapter five of this dissertation a reprint of this publication. The third one is "Artificial Intelligence Algorithms Enable Automated Characterization of the Positive and Negative Dielectrophoretic Ranges of Applied Frequency", the co-authors listed in this paper are Matthew Michaels, Shih-Yuan Yu, and Fangzhou Du, chapter two of this dissertation a reprint of this publication.

VITA

TUO ZHOU

SUMMARY

Highly motivated researcher and successful teaching assistant with a research background in material science, micro/nanofabrication, and micro/nanomanufacturing, skilled in time management and critical analysis.

EDUCATION

University of California, Irvine Sep.2018-Ongoing GPA: 3.756/4.0
PhD student in Material and Manufacturing Technology

University of California, Irvine Sep.2016-Jun. 2018 GPA: 3.456/4.0
Master of science in Material Science and Engineering

Iowa State University Sep.2012-Jun.2016
GPA:3.010/4.0
Bachelor of science in Material Science and Engineering

SKILLS

- **Software:** COMSOL, AutoCAD, Microsoft Office, SolidWorks, Python
- **Experimental:** SEM, AFM, TEM, Micro-electromechanical System (MEMS), Photolithography, E-beam Evaporation, Lift-off Process, Mask Aligner, Electrospinning, 4 years of clean room experience
- **Languages:** Mandarin (native), English (fluent)

RESEARCH AND TEACHING

Research Assistant, University of California, Irvine

(Sep.2018-Ongoing)

- Conducted 3 National Science Foundation (NSF) sponsored research projects
- Published 6 journal papers and 3 peer-reviewed conference papers
- Presented at 2 international conferences
- Filed for 2 patents
- Received 2 fellowships

Teaching Assistant, University of California, Irvine

(Jan.2019-Ongoing)

- Assisted four courses, including *Theory of Mechanics and Mechanism, Introduction to viscous and compressible flow, Introduction to thermodynamic, and Introduction to thermodynamic*
- Conducted discussion sessions and office hours and designed homework for more than 400 students in two years

Research Supervisor, UCI KULINSKY BINOM (BIO-NANO-MICRO-MANUFACTURING) Lab

(Sep.2018-Ongoing)

- Guided more than ten undergraduate students and helped them publish one journal paper in Journal of Micro and Nano-Manufacturing and one conference paper in Third World Congress on Micro and Nano Manufacturing

RESEARCH PROJECTS

Automated Characterization of the Dielectrophoretic Properties via Artificial Intelligence (AI) Algorithms

(Funded by National Science Foundation, award number 1661877) (Sep.2020-Ongoing)

- Presented in the 2021 Third World Congress on Micro and Nano Manufacturing and published a conference paper
- Published a journal paper in Micromachines
- ➢ Developed an AI-enabled platform capable of automatically determining the Dielectrophoretic properties

Development and Characterization of the Novel Guided Electrokinetic Microassembly Method

(Funded by National Science Foundation, award number 1661877)
(Sep.2018-Ongoing)

- Published a first-author journal paper in ACS APPLIED MATERIALS & INTERFACES
- Presented in the Third World Congress on Micro and Nano Manufacturing and published a conference paper
- Filed one patent (US20210348289A1)
- ➢ Developed a novel platform using photolithography that guided electrokinetic micro-assembly of polystyrene microparticles with different sizes onto specific

locations of patterned carbon microelectrodes

Development of Novel Method of Guided Healing of Damaged Microelectrodes via Electrokinetic Assembly of Conductive Carbon Nanotube Bridges
(Jan.2021-Jun.2021)

- Published a first-author journal paper in Micromachines
- ➢ Demonstrated that electrically conductive CNT bridges could be assembled across large electrode gaps to heal the electrodes using dielectrophoretic step-wise deposition of carbon nanotubes from suspension

Development of Novel Process for Dielectrophoretic Formation of Conductive Carbon Nanotube Bridges

- Published a first-author journal paper in Micromachines (Sep.2019-Jan.2020)
- Filed one patent (US20210309869A1)
- ➢ Developed a novel step-wise process that incorporates electrokinetic phenomena to deposit and form long chains of CNTs along the electrical field lines of an external AC field
- ➢ Demonstrated for the first time the creation of conductive CNT bridges over 50 μm in length

Fabrication of Polyacrylonitrile (PAN) -derived Carbon Nanowire (NWs)

(Funded by National Science Foundation, award number 1449397)
(Sep.2016-Sep.2018)

- Published a journal paper with a multinational research team of 11 (USA, Mexico, and China)
- ➢ Designed and built an innovative nearfield electrospinning-based carbon nanowire patterning platform
- ➢ Developed a scalable nanomanufacturing platform capable of fabricating graphene-coated carbon nanowires less than 50nm in diameter

Optimization of Composition of the Alkali Silicon Low Temperature Ceramics

(Funded by 3M) (Jun.2015-Jun.2016)

- ➢ Determined the optimized composition of the Alkali Silicate Low Temperature ceramic with the lowest amount of liquid binder that exhibited the maximum compressive strength
- ➢ Maximized the compressive strength further by comparing different

fabrication methods, such as slurry molding and die pressing

AWARD&HONOR

- Recipient of DTEI (Division of Teaching Excellence and Innovation) Fellowship in recognition of my dedication as an outstanding TA who helped instructors improve their courses
- Recipient of UCI's Henry Samueli Endowed Fellowship in recognition of my achievements as an outstanding graduate student

PATENTS

- Patent Title: Step-wise fabrication of conductive carbon nanotube bridges via dielectrophoresis
  Patent/Application Number: 17223459

  Issue Date: 10/7/2021
- Patent Title: Guided template-based electrokinetic micro-assembly
  Patent/Application Number: 20210348289

  Issued Date: 5/7/2021

SOCIAL MEDIA

Google Scholar

PUBLICATIONS

Journal Papers

- T. Zhou, M. Michaels, and L. Kulinsky, "Guided Healing of Damaged Microelectrodes via Electrokinetic Assembly of Conductive Carbon Nanotube Bridges," *Micromachines*, vol. 12, no. 4, p. 405, 2021.
- T. Zhou, J. Chen, E. Kropp, and L. Kulinsky, "Guided Electrokinetic Assembly of Polystyrene Microbeads onto Photopatterned Carbon Electrode Arrays," *ACS Applied Materials & Interfaces*, vol. 12, no. 31, pp. 35647–35656, 2020.
- T. Zhou, E. Kropp, J. Chen, and L. Kulinsky, "Step-Wise Deposition Process for Dielectrophoretic Formation of Conductive 50-Micron-Long Carbon Nanotube Bridges," *Micromachines*, vol. 11, no. 4, p. 371, 2020.

- Michaels, Matthew, et al. “Artificial Intelligence Algorithms Enable Automated Characterization of the Positive and Negative Dielectrophoretic Ranges of Applied Frequency.” *Micromachines*, vol. 13, no. 3, 2022.
- J. Cortez, K. Damyar, R. Gao, T. Zhou, and L. Kulinsky, “Electrokinetic Propulsion of Polymer Microparticulates Along Glassy Carbon Electrode Array,” *Journal of Micro and Nano-Manufacturing*, vol. 8, no. 2, 2020.
- D. George, A. Garcia, Q. Pham, M. R. Perez, J. Deng, M. T. Nguyen, T. Zhou, S. O. Martinez-Chapa, Y. Won, C. Liu, R. C. Lo, R. Ragan, and M. Madou, “Fabrication of patterned graphitized carbon wires using low voltage near-field electrospinning, pyrolysis, electrodeposition, and chemical vapor deposition,” *Microsystems & Nanoengineering*, vol. 6, no. 1, 2020.

Conference papers

- T. Z. Zhou, S.-Y. Yu, M. Michaels, F. Du, L. Kulinsky, and M. A. Al Faruque, “Establishing Digita Recognition and Identification of Microscopic Objects for Implementation of Artificial Intelligence (AI) Guided Microassembly,” in *arXiv preprint arXiv*.
- T. Zhou, Y. Lu, S. H. Zad, Y. Zhou, L. Zhao, and L. Kulinsky, “Dielectrophoresis-driven Assembly of Polymer Microbeads and Carbon Nanotubes Upon Fabricated Carbon Microelectrodes,” in *Proceedings of the World Congress of Micro-and NanoManufacturing*.
- J. Cortez, K. Damyar, R. Gao, T. Zhou, and L. Kulinsky, “Electrokinetic movement of the microparticulates between high resistance microelectrodes under the influence of dielectrophoretic force,” in *Proceedings of the World Congress of Micro-and NanoManufacturing*.

ABSTRACT OF THE DISSERTATION

Microfabricated Platforms for Microassembly of Inorganic/Organic/Biological System
by

Tuo Zhou

Doctor of Philosophy in Engineering

University of California, Irvine, 2022

Professor Lorenzo Valdevit, Co-chair

Professor Lawrence Kulinsky, Co-chair

Assembly of microdevices from constituent parts usually relies on serial steps via assembly processes such as pick and place operations. These serial assembly processes are slow and produce insufficient yield as parts size decreases from millimeters to microns. The present work introduces an electrokinetic assembly process that acts on micro- and nano-parts via a guided, noncontact, scalable process capable of selectively attracting specific types of microparts by varying the frequency and potential of the applied AC signal. The Photolithography and Carbon-MEMs (CMEMs) processes are utilized in creating interdigitated electrode arrays (IDEAs) that are used as substrates for the discussed electrokinetic guided micro and nano assembly. Electrokinetic forces under consideration include dielectrophoresis (DEP) and electroosmosis (EO).

The work starts with outlining the current state-of-the-art in the field of micro- and nano-assembly and progresses to describe the fabrication and experimental setup of the electrokinetic assembly platform. The IDEAs are coated with a layer of lithographically

patterned resist so that when an AC electric field is applied to the IDEA, microparticles suspended in the aqueous solution are attracted to the open regions of the electrodes not covered by photoresist. The interplay between AC electro-osmosis and dielectrophoretic forces guides polystyrene beads of different sizes to assemble in regions, or "wells," uncovered by photoresists atop the electrodes. This is followed by the results and discussion of the electrokinetic assembly of 1 micron and 5 micron polymer (polystyrene) beads at specific locations on glassy carbon interdigitated electrode arrays. One application proposed for this microassembly technique is the post-amplification of chemical and biological assays by collecting the fluorescent beads into the wells for enhancement of the fluorescent signal of the test.

The work subsequently introduces an Artificial Intelligence (AI) based approach that supplements the electrokinetic handling of the microbeads. The visual feed from the digital camera is digitally processed to recognize the interfaces of the beads, and the AI algorithms are then used to determine if the beads are attracted to or are repelled from the electrodes. This process is used to automatically determine the dielectrophoretic cross-over frequency, a critical property for studying dielectrophoresis of micro- and nano- parts. In this study, a Feedback Control System first uses a digital camera and a microscope to capture microbeads' motion. And then, the OpenCV software package analyzes the relative positions of microbeads in consecutive frames to determine the direction of the microbeads' movement for the characterization of frequency ranges for positive and negative DEP.

Finally, a step-wise process using DEP force is presented. This step-wise process is used to deposit the carbon nanotube bridges along the applied electric field lines between two

neighboring electrodes, and its application on healing damaged microelectrodes and the performance of the healed microelectrode are discussed.

Chapter 1

Background

1.1 : Carbon Allotropes

Since its discovery, carbon has been the element that revolutionized science and technology due to its remarkable properties. The ability to form bonds with other elements has made it a valuable candidate for various applications, influencing many fields of research. For example, due to their excellent electric properties and biocompatibility, carbon materials have been of the interest of electronics and biological applications, such as transistors and bio sensors. The attractive properties of carbon materials include but are not limited to 1) they exist in many types of forms, 2) they have a wide electrochemical stability window, 3) they have excellent biocompatibility, 4) they are low cost, 5) chemically inert [1]. Carbon and its allotropes have been the building blocks of organic chemistry.

Carbon has been found in the forms of many allotropes, such as diamond, graphene, graphite, carbon nanotubes (CNT), fullerenes, and glassy carbon[2][3][4][5][6]. The discovery of those carbon allotropes and the attempts to study their unique properties have initiated and advanced many new research areas on their applications.

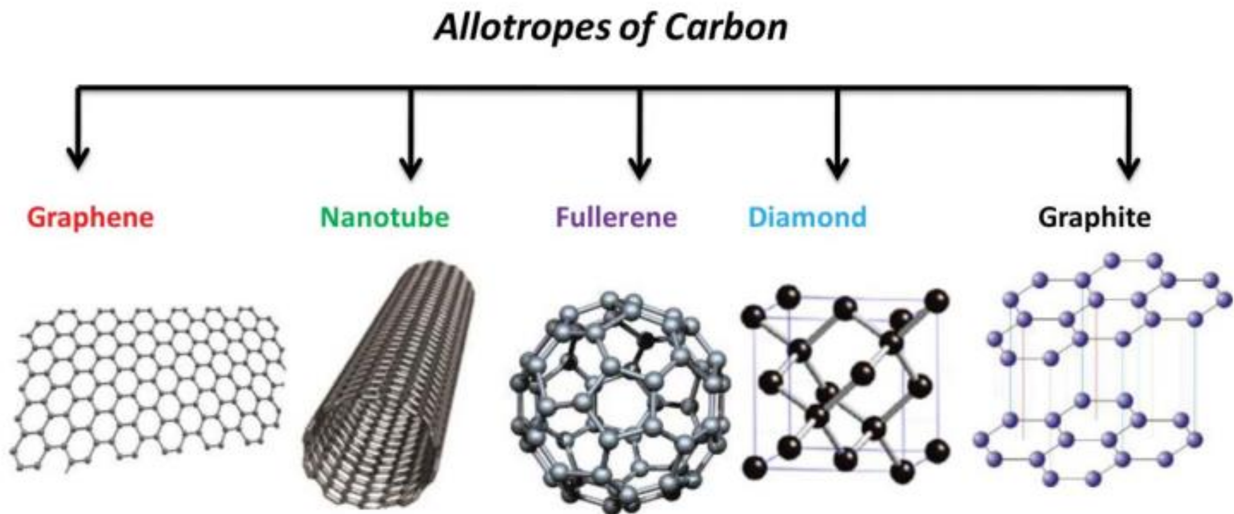

Figure 1: Crystal structure of the main allotropes of carbon [6].

Synthesized by extracting from bulk graphite in 2004 for the first time [7][2], graphene is perhaps the most important one of these allotropes of carbon. Graphene's 2-D structure consists of hexagonal carbon rings. Figure 1 indicates that each individual carbon is held together by sp^2 -hybridized bonds. Graphene is the structural unit of other allotropes of carbon, including carbon nanotube (CNT), which is the curled sheet of the graphene layer, and fullerene, which is in the form of a fully or partially closed mesh[6].

Unlike other allotropes with organized patterned structures, Glassy carbon is derived from the pyrolysis of organic precursors, such as phenolic resins, polyfurfuryl alcohols, and polyvinyl chloride. Owing to its excellent mechanical, chemical, thermal, and electrical properties, glassy carbon has an extremely wide spectrum of applications ranging from biomedical to the energy sector. Therefore, since its discovery, it has attracted increasingly attention from industry and academia.

It's noteworthy that glassy carbon has proved to be a suitable candidate for the electrodes for electrochemical applications due to its chemical inertness and good electrical conductivity. The unique properties of glassy carbon are attributed to its structure. The electric properties of GC vary with the variation in structure parameters, including the number of graphene layers, the thickness of the layers, and the type of helicity. Therefore, they can be used as metals and semiconductors [8][9][10][11][12].

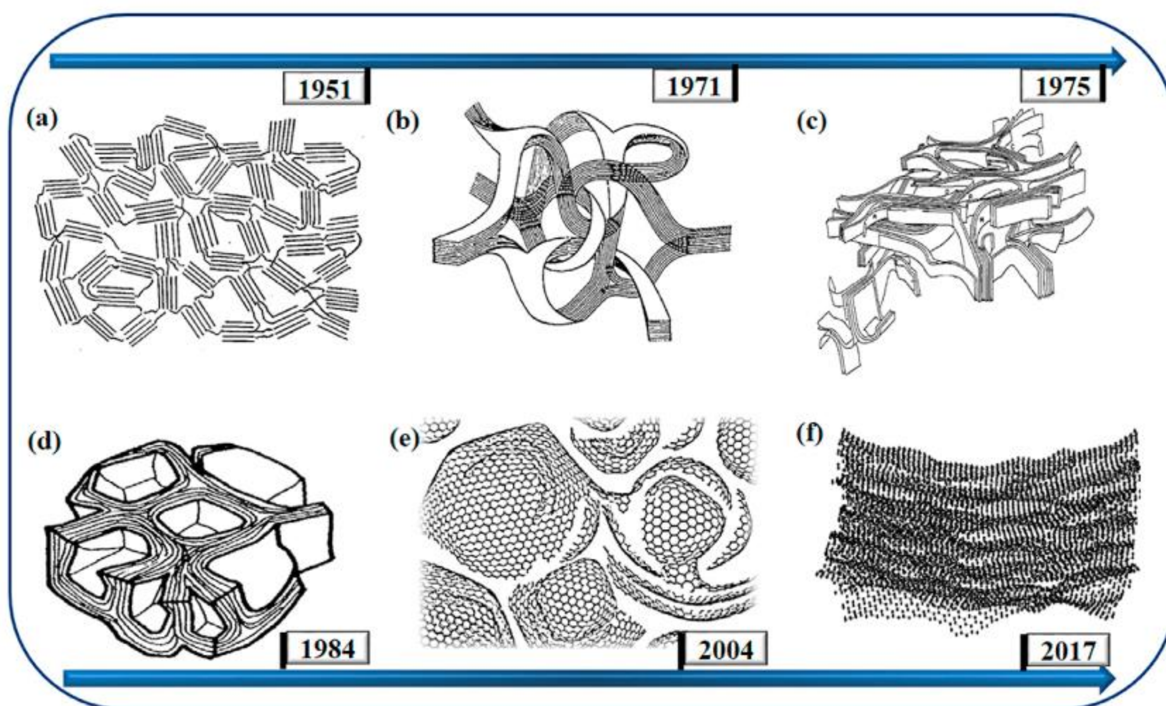

Figure 2: Structural models describing the structure of glassy carbon[13]: (a) Franklin model; (b) ribbon-like model[14]; (c) Ban model [15]; (d) closed-like graphitic structure[16]; (e) (f)The fullerene-related structural model [17];

There are many models proposed by different groups describing the structure of glassy carbon, as figure 2 indicates, such as Franklin model[18], ribbon-like model by Jenkins[19], and the fullerene-related structural model by Harris[17]. Despite the differences among

those models, it's believed that glassy carbon consists of disorganized graphitic sheets of sp^2 carbon atoms arranged in hexagonal patterns [13].

CNT has been regarded as another most studied carbon allotrope owing to its exceptional properties, such as remarkable tensile strength and good thermal conductivity [3][5][20], and thus various applications including nanoelectronics, energy storage, and optics. Basically, CNT is the form of rolled-up graphene sheets. In general, it can be classified into two single-walled nanotube (SWCNTs) and multi-walled nanotube (MWCNTs), depending on the number of layers rolled up to form the CNT.

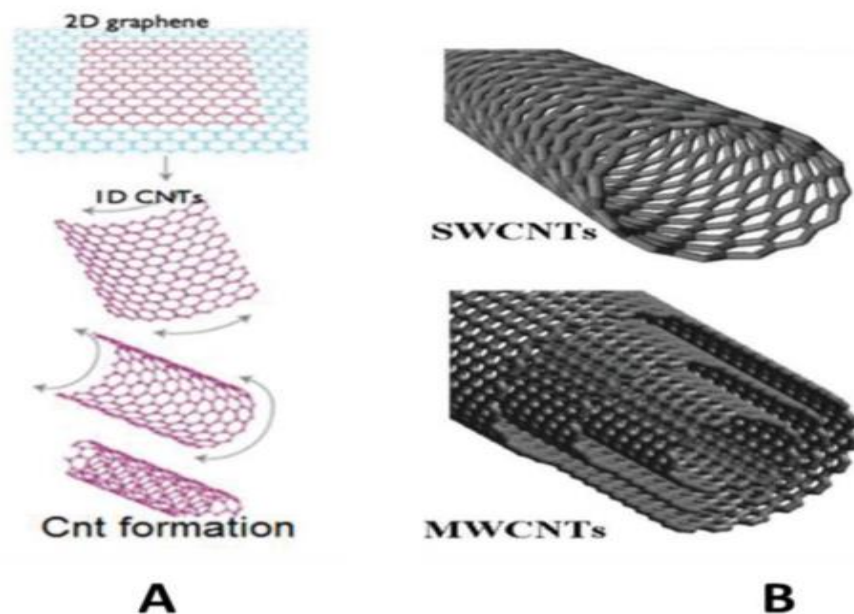

Figure 3: Schematic representations of the formation (A) and structure of CNT (B)[10].

As Figure 3 shows, MWCNTs are produced by rolling up multiple graphene layers. On the contrary, SWCNTs are by one layer.

1.2 : Carbon MEMS

Carbon -MEMS refers to the process and microfabrication techniques that carbonize the pre-patterned resist (precursor) at various temperatures and atmospheres. Many methods have been used to directly machine the carbon materials, although they are difficult to machine, including focused ion beam (FIB)[21], thermochemical etching[22], and laser machining[23]. However, people found out those methods are either time-consuming or expensive. For example, FIB is slow and needs expensive high vacuum systems. On the contrary, Polymer, as a popular candidate for precursor, is easier to be machined or pre-patterned by various tools and techniques compared to carbon materials that are brittle and hard. Common polymeric precursors include but are not limited to resins of furfuryl alcohol, phenol-formaldehyde, acetone-furfural, or furfuryl alcohol-phenol copolymers. More importantly, high-quality commercial precursors, such as SU-8 photoresists, always used when fabricating structures with a high aspect ratio[24], and standardized procedures and tools are crucial for the reproducibility of the fabrication process. The essence of C-MEMS is selecting an appropriate precursor, most likely polymers, followed by being machined or pre-patterned, then converting it to carbon[1]. For example, Whitesides's group fabricated free-standing glassy carbon by patterning poly (furfuryl alcohol) using soft lithography and then carbonizing it at 500-100 °C under argon[24].

The choice of techniques to pattern the precursor is determined by complexity, dimensions, and the quality of the resulting carbon part. Many well-developed patterning techniques include polymer molding and casting, electrospinning, and electron beam lithography. But

the most common one is conventional photolithography, which will be discussed in the following sections.

As the final part of C-MEMS, carbonization is the process through which the resulting carbon structure is produced from the polymeric precursor, usually by pyrolysis in an inert atmosphere. Therefore, the parameters of the process, including temperatures, rpm, and dwelling time, dictate the important properties of resulting carbon materials. In the case of C-MEMS, the concerned properties usually are conductivity, shrinkage, and carbon content.

The furnace is the tool for pyrolysis, and nitrogen is required to keep an inert atmosphere. Pyrolysis includes three main steps, each of which features a different temperature, rpm, and dwelling time. The first step usually needs the temperature to be raised to 300°C at 10°C and a subsequent 30 mins dwelling period to eliminate the residual solvent in precursors and remove oxygen in the furnace chamber. The second stages increase the temperature further to 900°C-1000°C at 10°C/min, followed by a 1 to 4-hour dwelling time. The last step is cooling down to room temperature naturally [1].

It is worth mentioning that the shrinkage of the original patterned shape happens during carbonization because it is a significant factor to consider before designing the carbon structure.

Many groups have studied the effects of carbonization parameters on the extent of shrinkage. The higher temperature from 600°C to 1000°C caused severer shrinkage than lower temperature[25][26]. Pyrolysis atmosphere was also believed to play an important role in shrinkage. For example, nitrogen leads to more shrinkage than a vacuum atmosphere[27].

Moreover, many studies have found out the geometry and shape of original precursors also influence the shrinkage, especially height and aspect ratio[28][29][30][31][32].

Many applications of C-MEMES have been demonstrated. Some studies proved that C-MEMS microfabrication processes could be used to build 3D battery architecture[33][34]. Other groups applied C-MEMS in the fabrication of supercapacitors[35][36] and sensors[37][38]. Since carbon materials exhibit excellent biocompatibility, the device fabricated by C-MEMS has been widely used as the scaffold to grow and differentiate cells[39][40]. Although many applications use C-MEMS, people are still expanding the spectrum of its applications.

1.3 : Photolithography

Many forms of lithography could be used as patterning techniques, such as electron-beam lithography[41], x-ray lithography[42], and extreme ultraviolet lithography[43]. Photolithography is the most widely used one among various lithography techniques. It's believed that pattern transfer from a mask to a thin film is achieved almost exclusively through photolithography. Generally, photolithography, invented in 1959, was used to describe the process which employs high-intensity light sources to transfer the pattern on the photomask onto the thin film of light-sensitive photoresist deposited on the substrate. Figure 5 shows the important steps of the conventional photolithography process in the case of using a negative photoresist and silicon wafer as a substrate. The performance of a photolithographic process can be judged by various parameters, including the resolution, defined by the minimum produced features, and throughput, which is the number of wafters transferred per hour[1].

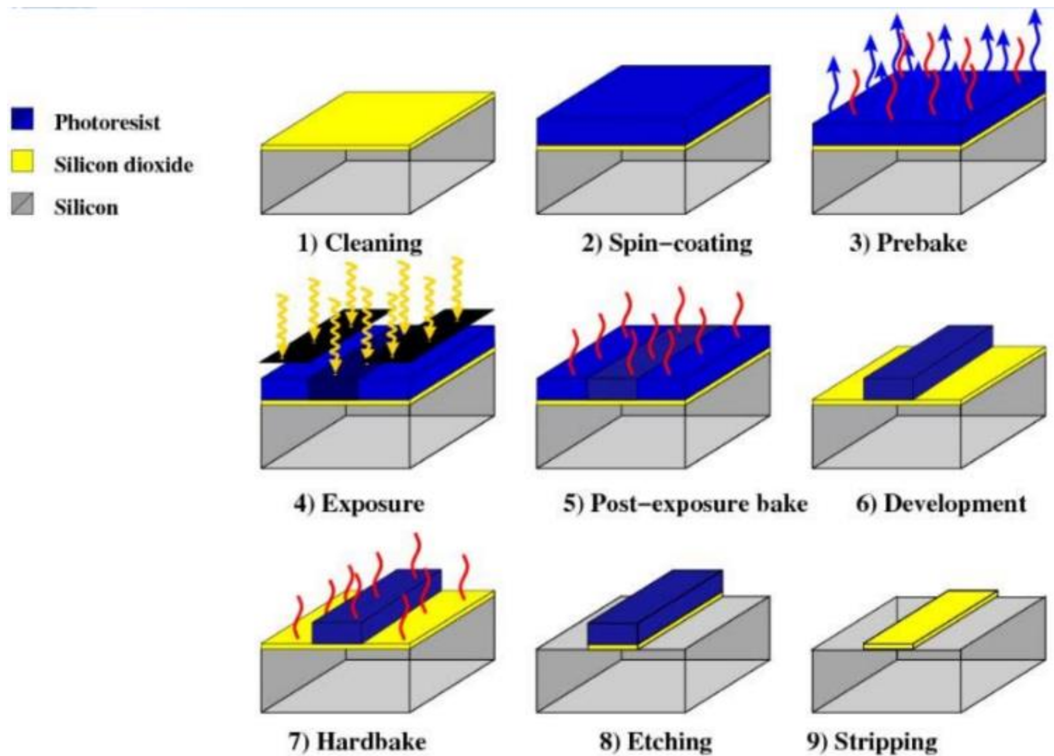

Figure 4: The process of conventional photolithography[44].

The first important step, even for all forms of lithography, is the cleaning of wafers. Contaminants, including dust, solvent stains, and particles, could cause defects in the resulting structure and possible damage photomask. Since it is a scientific discipline in its own right, various method of wafer cleaning has been invented. The most famous ones are RCA 1 and RCA 2, which employ mixtures of hydrogen peroxide and other acids to rinse wafers [45]. Others include dry methods, such as thermal treatments and plasma or glow discharge techniques[46], and mechanical methods, such as ultrasonic cleaning[47].

The second step, as figure 5 shows, is spin-coating. It's believed that photoresist deposition is the most expensive step with photolithography because this step usually comes with wasting a huge amount of photoresist. Spin coating, the most well-known deposition

technique, is usually applied to deposit thin photoresist (≤1 μm) to fabricate the planar or short 3-D structures. After cleaning the wafer, a thin layer of photoresist is deposited on the surface of the wafer. Then resist spinner is used to dispense the photoresist until it is covered the whole surface uniformly. Usually, an initial speed of 500 rpm is used to spread out the photoresist. And then, a secondary high speed, ranging from 500rpm to 6000rpm in the case of SU-8, to which the spinner needs to accelerate within a short period of time, is achieved for the further thinning of the photoresist to a desired thickness. There is an empirical expression that could be used to predict the final thickness.

$$T = \frac{KC^{\beta}\eta^{\gamma}}{\omega^{\alpha}} \quad [1]$$

Where T is the final thickness, K is the calibration constant, C is the photoresist's polymer concentration, η the photoresist's viscosity, ω the number of rotations per minute (rpm), and β,α, γ are the empirically determined constants.

As a result, photoresist properties and the spinner's rotational speed determine the final thickness.

If the greater thickness or high aspect ratio feature is needed, casting [48]and thick sheets of dry photoresist[49] could be alternatives to spin-coating. Resist spraying[50] and electrodeposition [51]are used for covering photoresists onto the prefabricated structures. Readers can find more information about deposition techniques in Professor Madou's book [52].

Soft baking or prebaking is usually carried out on a hot at 60°C-85° for 1the to 3 minutes to evaporate the remaining solvent in the photoresist, enhancing adhesion between the

photoresist and substrate. Failure to do so would result in unwanted resist profiles and delamination of resist from the substrate[53]. Besides the hot plate, conventional ovens, microwave heating, and IR lamps have proved effective in conducting soft baking [54].

The exposure step involves masks and incident radiations. Radiation initiates, but the post-bake completes the chemical reaction that changes the solubility of the exposed area of the photoresist. The photoresist consists of three components: resin (polymer), solvent, and sensitizer. The polymeric structure change under exposure to radiation is the main reason the solubility is altered, as the photosensitizer is responsible for the photochemical reaction[55][28]. The photoresist can be classified into two groups regarding whether the exposed areas are being preserved or dissolved. For the negative photoresists, the exposed areas remain after development owing to the strengthening of the polymer by cross-linking its main and side chains. On the contrary, the exposed areas of the positive photoresist dissolve because of the scission of the main and side chains[52]. Interested readers can find more information about resist tone in chapter 1 of Professor Madou's book [44].

SU-8, an acid-catalyzed negative tone photoresist, is composed of EPON® SU-8 resin as its main component, the organic solvent in which the resin is dissolved, and 10 wt% of triarylsulfonium hexafluoroantimonate salt as the photo-initiator[55]. The most common organic solvents are propylene glycol methyl ether acetate (PGMEA), cyclopentanone, and gamma-butyrolactone (GBL). The differences amongst commercial SU-8s are the choices and amount of organic solvents used[29][56].

The structure of a SU-8 monomer before and after crosslinking can be found in the reference[57]. A single molecule contains 8 epoxy rings, explaining why it's dubbed SU-8 and

demonstrating high epoxide functionality per molecule[57]. As a result, the unique structure of the SU-8 molecule makes a high degree of cross-linkage possible. The first step in the crosslinking process is the protolysis of triarylsulfonium hexafluorantimonium, resulting in the decomposition of the photoinitiator and generation of hexafluoroantimonic acid[58]. As the first reaction, UV exposure is necessary for pyrolysis reaction. The photoacid generated in the first protolysis step induces the polymerization of SU-8 by opening the epoxy rings as the second reaction[58]. The last step is a series of reactions initiated by the oxonium ions and completed by applying heat through the post-exposure bake[58].

In the case of photoresists like SU-8, exposure only initiates the crosslinking process. Therefore, the postexposure bake (PEB) is of great importance for cross-linking completion. It has been proved that the temperature of PEB and the baking time determine the performance of the final structure. The data sheet provided by the SU-8 manufacturer suggests 95°C for 2-5 minutes. However, many studies found out lower temperatures (55°C to 75°C) for longer baking time and slow heating or cooling rate should be considered for reducing internal stress, which is the main cause of defects [59][60] [61].

After the post-baking, in the context of negative photoresist SU-8, the unexposed areas are dissolved in the development step. As a result, a topography, used as either a mold or a permanent structure, appears after the development. Generally, there are dry and wet developments, but in the case of SU-8 development, the latter is more likely to be used. During the development, the uncrosslinked portions of the SU-8 are dissolved after being Immersed in the Propylene glycol methyl ether acetate (PGMEA) solution. Mild agitation

provided by the rotator is suggested to increase the efficiency. After the development, the residue of the developer is rinsed with isopropanol (IPA).

Hard baking is recommended if the SU-8 pattern is used as the final device or subjected to a thermal process. Hard baking is generally carried out on a hot plate at 150C- 200C for 5 to 30 minutes. During the hard baking, solvent residues are evaporated, hardness of the structure is improved. Therefore, hard baking is not suggested in the application requiring resist removal, as the last one in Figure 4.

Photoresist stripping should be incorporated into the SU-8 lithography process if the resist was sacrificial material and the device need to be undamaged by the stripper. The standard wet strippers include H2SO4 and Piranha, which only attack SU-8 and is unreactive with silicon and silicon oxide. Unlike wet stripping, dry stripping is believed to be more controllable and produce less dangerous chemicals. Common dry tripping includes plasma stripping, UV stripping, and reactive plasma stripping.

1.4 : Microassembly

Microassembly or micro-device assembly refers to the groups of techniques that can implement the assembly of micro-sized devices and parts. Microassmeby techniques can fabricate complex devices whose fabrication involves incompatible processes and different materials, which conventional MEMS techniques are inadequate to complete. In general,

microassembly can be categorized into serial pick and place microassembly and parallel microassembly[62].

The former requires tools, such as a microgripper and operator, to handle micro-parts individually. The advantage of pick-and-place assembly is the precise placement of the micro-parts into the desired locations. However, there are many complexities associated with it. The most important among them is the scaling effects, which makes the forces negligible in the macro become dominating in the micro world. For example, the adhesive forces between the surfaces of the gripper and the parts become stronger than the gravitational force, resulting in difficulty in putting down parts into target locations[62]. Another imperfection of pick and place is the used tools' complex and relatively expensive fabrication processes. For example, Reference[63] introduced a micro-tweezer fabricated by the High aspect molded polysilicon (HexSil) Process, which involves plasma etching, conformal low-pressure chemical vapor deposition, and conventional surface micromachining[63]. In addition, the tweezer needs to mount on a cantilever connecting to a computer-controlled system[64].

In contrast to the pick and place, the parallel microassembly can manipulate an ensemble of micro-parts simultaneously, which can usually be achieved by either transferring patterns between wafer-to-wafer or taking advantage of some forces. The wafter-to-wafter transfer process resembles rubber stamping. For example, a research group demonstrated wafer-to-wafer transfer by transferring shells fabricated by HexSil from one handle wafer to another[65]. In this case, the tethers by which the shells are anchored on the handle wafer are broken by heating[65].

Magnetic and electric fields and their associated forces have been exploited to be incorporated into parallel microassembly systems. One group takes advantage of the dielectrophoretic force, an electrokinetic force discussed in detail in the following chapters, to assemble a bunch of particles to the surface of gold electrodes[66]. However, unlike the pick and place, this one failed to achieve precise placement of nanoparticles.

1.5 : Dielectrophoresis (DEP)

Generally, electrokinetics is the term used to describe the motion of particles suspended in fluid due to the application of electric fields. The common electrokinetic motions include electrorotation[67][68][69], electrophoresis, and dielectrophoresis (DEP)[69]. In this study, DEP is discussed in detail.

Dielectrophoresis (DEP) refers to the motions of particles generated by the interaction between a non-uniform electric field and the induced dipole moment of the particles. If a uniform electric field is applied, the charges will redistribute equally on either side of a dielectric particle. As a result, there is no movement due to the zero net charges and net forces.

Therefore the first criterion for generating DEP is the non-uniform electric field. In this case, the net charges accumulated on either side of the dielectric particle are different, so the non-zero net force is generated, and the movement will be discovered.

The second criterion for the generation of DEP is the polarizability difference between the dielectric particle and the medium. If the particle is more polarizable than the medium, more

charges are induced in the particle, and the direction of the induced dipole moment is the same as the applied electric field. As a result, the particle will move toward the regions where the electric field is stronger (positive DEP). On the contrary, if the medium is more polarizable than the particle, more charges will be accumulated in the medium, resulting in a movement away from where the electric field is stronger (negative DEP)[69]. The magnitude and direction of the DEP force can be determined analytically by the equation below[70]:

$$\langle \boldsymbol{F_{DEP}} \rangle = 2\pi r^3 \varepsilon_m Re\{CM(\omega)\} \nabla |\boldsymbol{E}|^2 \qquad [2]$$

$$CM = \left\{ \frac{\varepsilon_p^* - \varepsilon_m^*}{\varepsilon_p^* + 2\varepsilon_m^*} \right\} \qquad [3]$$

$$\varepsilon^* = \varepsilon_r + i\frac{\sigma}{\omega} \qquad [4]$$

where $\nabla |\boldsymbol{E}|^2$represents the magnitude-squared of the electric field, r the radius of the particle, ε_m the relative permittivity of the medium, and ε_m^* and ε_p^* the complex permittivities of the fluid medium and particle, respectively. CM refers to Clausius-Mossotti factor, which determines the direction of DEP force when an ac electric field is applied. When CM is bigger than zero, a positive DEP is induced. When CM is smaller than zero, a negative DEP is induced. A special case of zero CM needs to be noted. Under this condition, there is no DEP force, and the associated frequency at this point is called cross-over frequency.

1.6 : Electroosmosis (EO)

AC electro-osmosis describes the nonlinear flow around a polarized surface caused by interactions between an external AC electric field and ionic charges accumulated in the diffuse double layer on an electrode surface[71]. AC electro-osmosis generated with coplanar bar electrodes has been studied extensively[72][73]. For ACEO, the velocity of the flow is primarily dependent on both the applied frequency and the magnitude of the field's strength[74]. The velocity of the flow is negligible at extremely low frequencies and gradually grows with increasing frequency. As the frequency is increased, the velocity of the flow has the propensity to increase sharply until a maximum flow is reached, marked by some critical frequency (generally below 10 kHz). From this critical frequency, the velocity of the flow continues to decrease with increasing frequency until another minimum is reached. Generally, for cases in which the double layer is thin, in quasi-equilibrium (where ω is comparable to (σ/ε)), and on a perfectly polarizable metal electrode, the velocity of the flow can be quantitatively analyzed with the Helmholtz–Smoluchowski equation[75]:

$$u = -\frac{\varepsilon}{\eta}\Delta\phi_d \frac{\partial\phi}{\partial x} = \frac{\varepsilon}{\eta}\Delta\phi_d E_x \qquad [5]$$

where u is the velocity of the fluid, ε the permittivity of the fluid, η the fluid's viscosity, ϕ the potential of the field outside the diffuse double layer, and $\Delta\phi_d$ the difference in potential between the outer layer of the diffuse double layer ϕ, and the potential of the inner portion of the diffuse double layer, Ψ.

Chapter 2

Guided Electrokinetic Assembly of Polystyrene Microbeads onto Photopatterned Carbon Electrode Arrays

2.1: Introduction

In this article, we report a novel guided microassembly technique that possesses the speed of self-assembly techniques while still maintaining the precision of direct-assembly techniques. This new technique utilizes a combination of guided dielectrophoresis (DEP) and AC electro-osmosis (ACEO) in conjunction with glassy carbon interdigitated electrode arrays (IDEAs). The IDEAs are further patterned with a layer of photoresist to define "windows", or exposed regions where microparticulates are to be positioned. In this study, polymer microbeads are suspended in deionized (DI) water and are guided by ACEO and DEP to assemble within the wells on top of the microelectrodes. Once microparts are attracted into their predetermined locations on the electrodes, they are permanently attached via the electropolymerization of a thin layer of the conducting polymer polypyrrole (PPy)[76][77][78]. Because the discussed guided assembly process is not serial in nature, it can be scaled up to achieve simultaneous assembly of a great number of micro- and nanoparts.

The guided electrokinetic assembly of microparticles based on photopatterned insulating templates is described and discussed here for the first time. Although polymer microbeads are used in the discussion of the assembly process, the use of such templates can be extended

to the assembly of parts or particles of various materials such as metals, organic, and nonorganic matter, and may be employed for nanoparticles as well. Therefore, this guided electrokinetic template-based assembly process has a wide range of possible applications, from the creation of a surface enhanced Raman spectroscopy (SERS) array, to the fabrication of biochips with deposited and entrapped cells[79][80].

2.2: Materials and Methods

The glassy carbon IDEAs used in the experiments were fabricated through conventional lithography techniques from SU-8 photoresist and were subsequently pyrolyzed38 to convert the organic resist into carbon. The IDEAs were fabricated on 4 in. diameter silicon wafers covered with a 1 μm thick layer of thermal oxide (University Wafer, MA, USA). SU-8 2025 photoresist (Microchem Corp. Ltd., MA, USA) was spin-coated onto the wafer at an initial speed of 500 rpm for 10 s, followed by an increase in the angular velocity of the spinner to 4000 rpm for 30 s using a Laurell photoresist spinner (Laurell Technologies, PA, USA). Following the spin cycle, the wafer was soft baked to 95 °C for 5 min on a Dataplate Pmc 732 hot plate (Dataplate Pmc 732 Series, IA, USA). Next, the wafer was exposed through a plastic mask (CadArt, OR, USA) to UV light with a UV flood exposure system (Oriel Instrument, Newport Corp, CA, USA) for 6 s at an energy intensity of 10 mW/cm2 to create the IDEA pattern. The wafer was postbaked on the hot plate at 65 °C for 1 min, and then at 95 °C for 5 min. SU-8 developer (Microchem Corp. Ltd., MA, USA) was utilized to etch out the uncross-linked regions of the photoresist. The wafer was then hard baked at 95 °C for 45 min. Lastly, the IDEA was carbonized inside a furnace (Thermo Fisher Scientific, Thermo Scientific, MA,

USA). After the pyrolysis process, the heights of the glassy carbon IDEA fingers were measured with a Dektak 3 profilometer (Veeco Instrument Inc., NY, USA) and found to be between 1.5 and 2.0 μm in height and 120−126 μm in width.

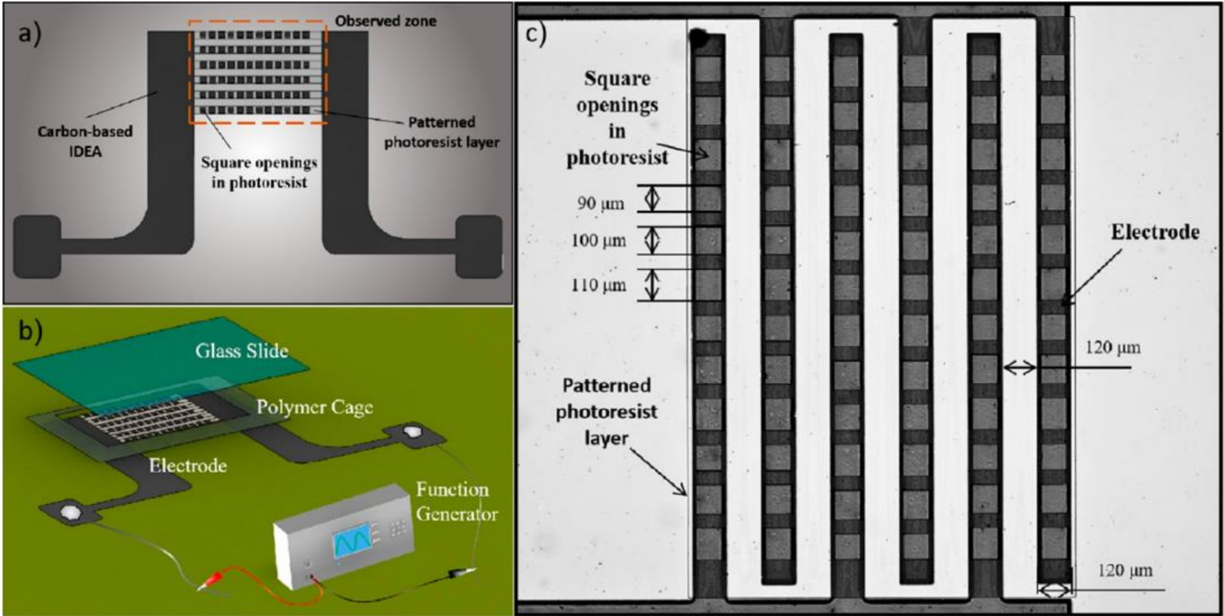

Figure 5: (a) Schematics of the IDEA chip with polymer cage created from double-stick tape and covered by the glass slide; (b) sketch of the interdigitated electrode arrays; (c) optical micrograph of the electrode fingers covered with square wells opened in the photoresist[81].

A layer of SU-8 photoresist was then coated over the IDEAs and lithographically patterned to form an array of wells in the resist layer. Figure 5 a−c presents the schematics and the optical micrograph of the IDEAs where each 120 μm wide electrode finger is separated by a 120 μm gap between the adjacent fingers. The design of the patterned photoresist layer consists of an array of alternating well sizes (90 × 90 μm, 100 × 100 μm,110 × 110 μm). These wells were produced via conventional lithography techniques utilizing an iron oxide mask (Front Range Photomask, AZ, USA) and a MA 56 mask aligner (Karl Suss, Germany). The thin

layer of SU-8 2002 photoresist was spincoated on the surface of the IDEA, and the subsequent soft-bake, exposure, and postexposure bake processes were all adjusted depending on the desired height of the resist layer. For a photoresist layer height of 3 μm, the resist was soft baked for 2 min at 95 °C, exposed for 4 s at an energy intensity of 10 mW/cm2 using the MA56 mask aligner's embedded light source, and postbaked for 3 min. The wafer was then hard baked at 95 °C for 45 min. For a resist height of 6 μm, the photoresist was soft baked for 3 min at 95 °C and exposed for 6 s with the same masker aligner and light source as before. The second layer was then postbaked for 5 min at 95 °C. Afterward, the un-cross-linked regions of the photoresist were etched away using the same SU-8 developer for 5 min. Lastly, the second layer was hard baked at 95 °C for 45 min.

Aqueous solutions of 1 and 5 μm diameter carboxyl-modified latex (CML) polystyrene beads (Thermal Fisher Scientific, Invitrogen, MA, USA), both possessing a weight percent of 4 wt % in their original media, were segregated and diluted to a new concentration of 0.39 wt % in DI water by placing the original solutions in a centrifuge (Eppendorf, Germany) for 10 min at 1500 rpm. The supernatant was removed with a pipet and the beads were mixed with the appropriate amount of DI water to achieve a 0.39 wt % solution.

After the IDEAs were fabricated, wires were soldered to the carbon contact pads of the IDEA chips using indium, and double-stick tape (3M, MN, USA) was cut to construct the fluidic chamber around the electrodes as presented in Figure 5a.

A 20 μL droplet was pipetted on top of the electrodes, and a glass cover slide (Thermal Fisher Scientific, Fisherbrand, MA, USA) was placed over the chip to facilitate microscopic observation and reduce evaporation of the fluid. A Nikon eclipse microscope (Nikon, Japan)

and SPOT Basic video editing program (SPOT Imaging, MI, USA) were used to observe and record the motion of the particles. The IDEA chip was connected to a function generator (Stanford Research System, CA, USA) to produce the AC field with any desired frequency and peak-to-peak voltage. Photos of the IDEA chip and lab setup are presented in Figure 5 b and c.

After the beads are attracted in the designated locations, they can be permanently entrapped via electropolymerization in the mixed solution of 0.1 M pyrrole monomers and 0.1 M NaDBS (sodium dodecylbenzene-sulfonate). The 100 μL polymerization solution is mixed with 1 mL of the bead suspension, and placed in an ultrasonic vibrator (Emersion Electric Co., MO, USA) for 30 min to prevent the colloid from flocculating. For each trial, 20 μL of the mixture was deposited onto the fingers of the electrodes and a glass lid was placed to cover the solution and IDEA. The electrodeposition of polypyrrole from the mixture was initiated by applying a 0.9 V DC offset for 60 s after the microbeads were positioned inside the wells after the guided assembly process.

2.3: Results

2.3.1: Steps of Template Electrokinetic Assembly.

The goal of the template electrokinetic assembly (TEA) process under study is to collect 1 and 5 μm polystyrene microbeads into specific locations where the carbon electrodes are exposed. These locations, or “wells,” are shown in Figure 5 a−c. Within the positive DEP regime, such as at an applied frequency of 1 kHz, 1 μm beads immediately gathered inside

the wells as Figure 6 shows. However, when the same frequency was used for the 5 μm bead suspension, most of the microbeads did not travel toward the wells. This can be explained by the fact that the viscous drag for the 5 μm beads is significantly greater than that for the 1 μm beads. The influence of particle size is demonstrated with Stokes law, which describes the viscous drag, Fd, that is experienced by a spherical particle of radius R moving through a fluid medium[82]. Because the larger drag forces experienced by the 5 μm beads prevent them from being positioned inside the wells upon initial application of a pDEP force, a two-step process incorporating both pDEP, nDEP, and EO flow is needed. For the first step, nDEP is applied to the beads using an AC field of 1 MHz applied frequency and 4 Vpp (peak-to-peak). Under these conditions, the initially homogeneous suspension of 5 μm particles is forced into three areas: the trenches between the electrodes, the gaps between the wells, and the centers of the wells as seen in Figure 7 a. Although this pattern was observed for all experiments with 5 μm beads during the described nDEP step, the 1 μm particle suspension under the same conditions remained homogeneously dispersed throughout the medium. The larger 5 μm beads gravitationally settle down to the level of the electrodes in a few minutes after the particle suspension is pipetted onto the electrodes.

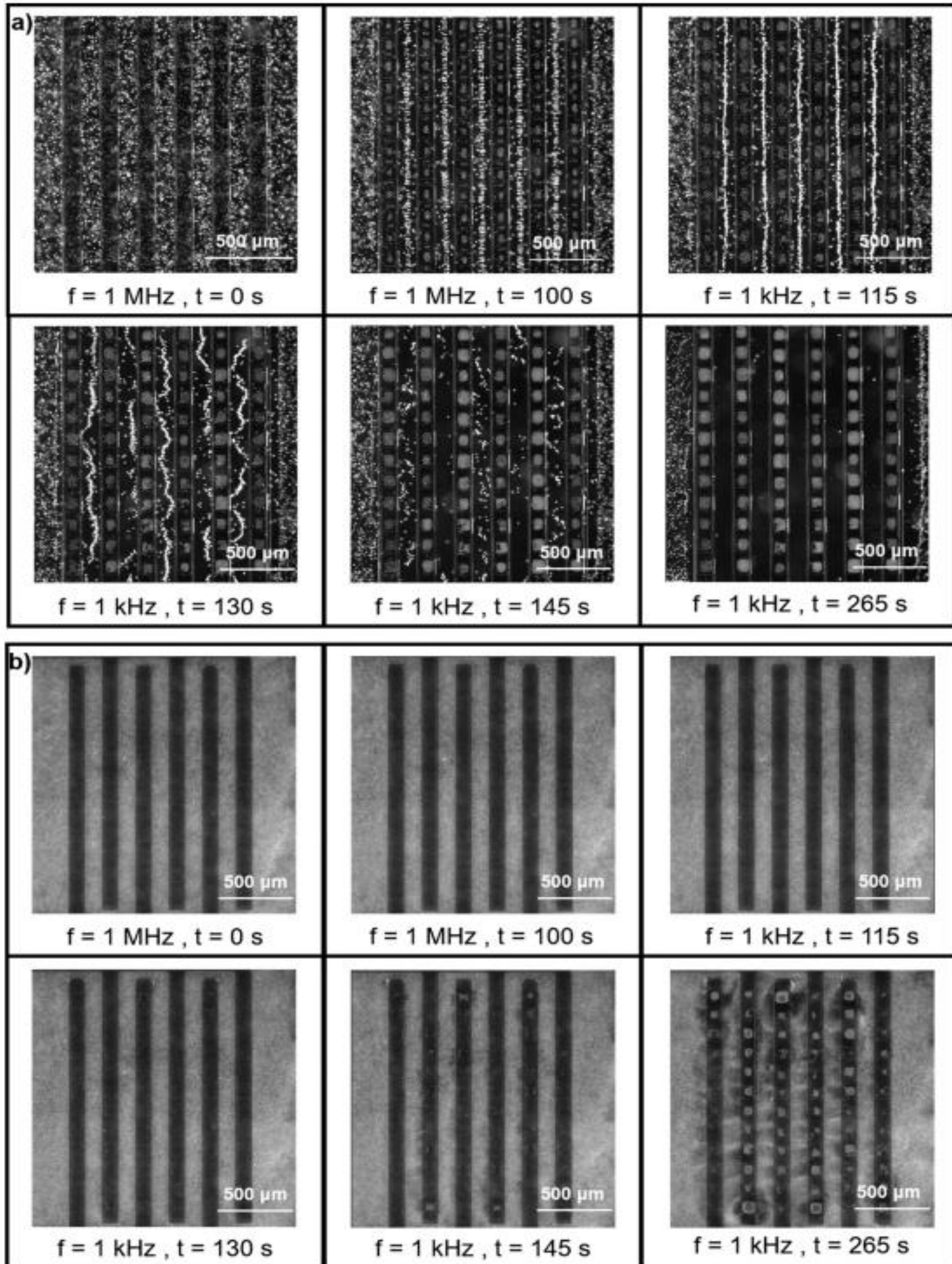

Figure 6: Process of template electrokinetic assembly (TEA) of (a) 5 µm and (b) 1 µm polystyrene microbeads[81].

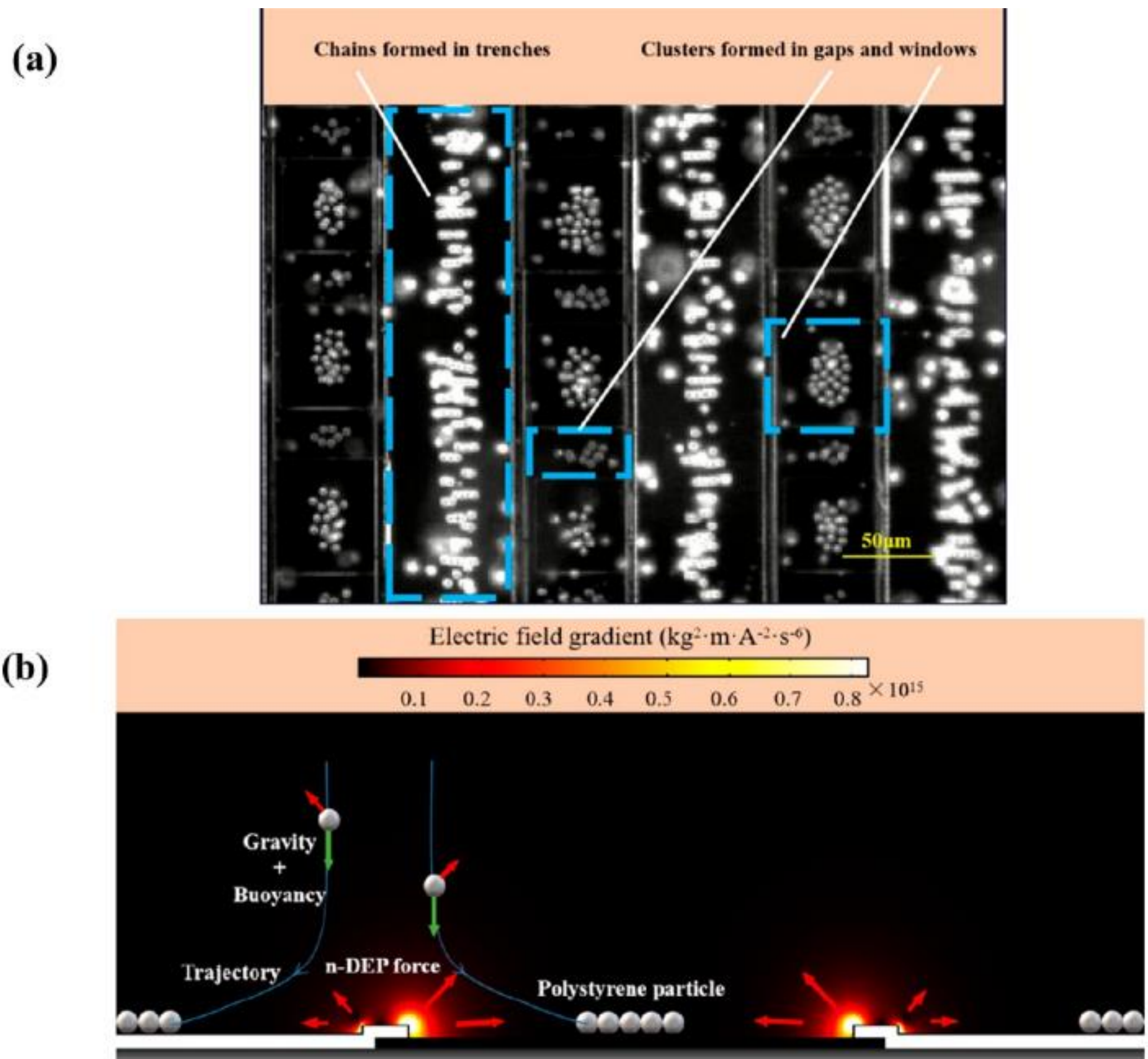

Figure 7: (a) Patterns formed by 5 μm particles under the effect of nDEP under 1 MHz, 4 Vpp AC bias; (b) COMSOL simulation results reflect the combination of gravitational sedimentation and nDEP on polystyrene beads and explains the formation of the observed initial bead pattern[81].

Once the beads are settled onto electrodes, the activation of the nDEP force repels the beads from the edges of the resist and pushes them in place within the wells of the electrodes and into other regions described above. In contrast, because the 1 μm beads remain suspended

above the electrodes, nDEP force repels the beads away from the surface of the electrodes. Once the nDEP step is performed, the frequency is lowered to 1 kHz, where the beads experience a positive DEP force. At this point, the 5 μm particles located in the trenches and gaps become attracted to the edges of the resist windows and are subsequently pulled into the centers of the wells, joining the cluster of particles as shown in Figure 7.

Demonstration of this guided electrokinetic assembly process can be seen in the video clips in the Supporting Information. Furthermore, these clips offer comparison between the kinematics of the 1 and 5 μm beads under the influence of positive DEP. Here, one can observe that the 1 μm particles were propelled from the bulk of the medium toward the wells at velocities larger than those of the 5 μm beads. This difference in velocities is likely due to the smaller drag forces associated with the 1 μm beads as previously mentioned.

2.3.2: Movement of 5 μm Beads under DEP.

The initial nDEP pattern formed by the 5 μm beads can be explained by the concentration of electric field lines near the edges of the photoresist windows in a process called insulator DEP (iDEP). The strong negative DEP forces are produced around the photoresist edges that cover the electrodes. Some 5 μm beads will settle to the bottom of the electrode chip, including into the wells. Once nDEP is applied, the beads already located inside the wells will be pushed together into the center of each well away from the well sides, whereas beads located between the wells (on top of the resist) are also repelled away from the edges and form lines at the centers of these gaps. Similarly, within the bulk fluid surrounding the electrodes, the beads are pushed away from the resist-covered edges of the electrodes and

form lines in the trenches between the electrodes as shown in Figure 7a. The influence of this nDEP force on the beads is demonstrated by the results of the COMSOL multiphysics simulation shown in Figure 7b.

Once the applied frequency is lowered to 1 kHz and the microbeads begin to experience a pDEP force, in addition to the edges of the resist, the clusters of microbeads inside the wells now also serve as points of highest electric field intensity. Under the influence of that pDEP force, remaining beads in the bulk of the fluid and in the gaps are attracted toward the wells. From the sequence of pictures shown in Figure 6, and in Supplemental Videos for 5 µm beads, it can be seen that the positive iDEP forces near the edges of the wells begin attracting the particles previously positioned in the gaps between wells. Simultaneously, pearl chains in the trenches between the electrodes become attracted to the outer sides of the wells, where they eventually reposition themselves as demonstrated in the optical micrographs and multiphysics simulation results presented in Figure 7.

2.3.3: Movement of 1 µm Beads under the Influence of Electro-osmosis

For 1 µm beads, because of their small size, the DEP force is weak in comparison to the ACEO, and consequently, the beads act as tracers to reveal the nature of the ACEO flow. It has been demonstrated in the literature that electro-osmosis-driven vortices are induced at the edges of coplanar bar electrodes as well as over the surface of the electrodes [72][83]. For the patterned electrodes, these EO vortices are generated above the wells at frequencies of 10 kHz and lower. Figure 8 a demonstrates the interplay between the positive DEP force and ACEO flow and its corresponding frequency dependence that affects the size of the bead

clusters inside the wells. In general with decreasing frequency, the vortices would expand from the edges of the wells toward their centers and push the beads inside the wells closer together. Figure 8 b presents a plot that quantifies the area of the 1 μm polystyrene bead clusters as a function of the frequency and magnitude of the applied potential. As 1 μm beads are propelled toward the windows by EO flow, they pass over the outer resist edges and are positioned near the edge of the windows, where they experience a positive iDEP force. Although some of the microbeads become attracted to this edge, most of the beads are carried toward the exposed regions of the electrodes inside the windows. As the clusters of beads inside the windows continue to grow, the iDEP force near the clusters will also become increasingly larger. The velocity of the flow under the electrokinetic influence and the resulting movement of the microbeads was simulated in COMSOL and is presented in Figure 8 c below.

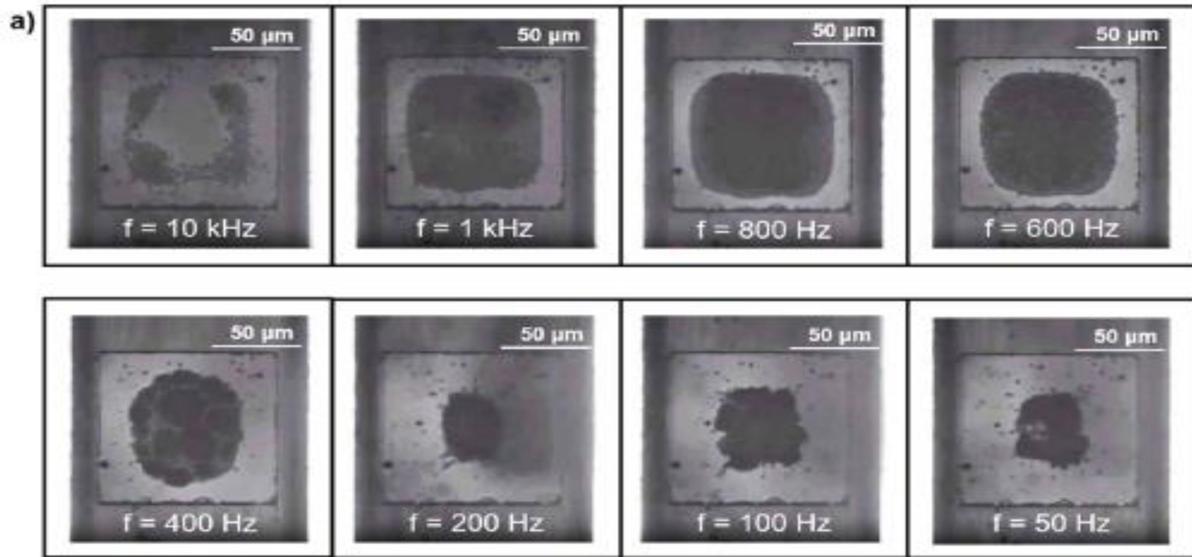

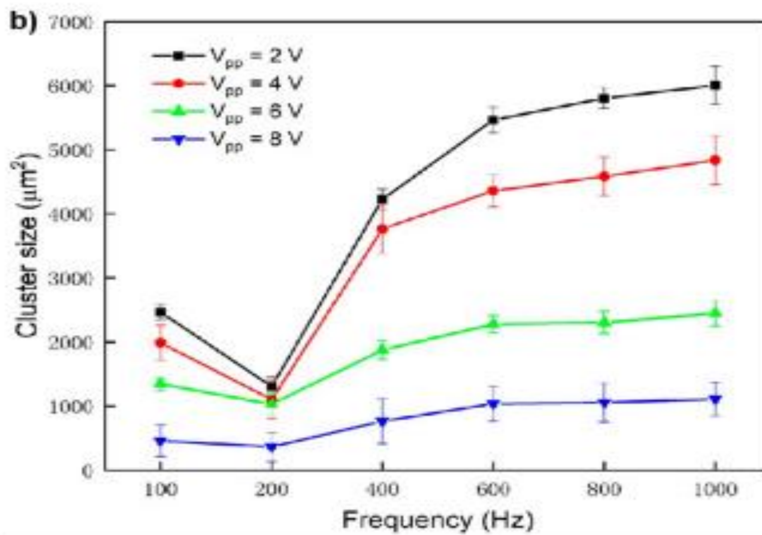

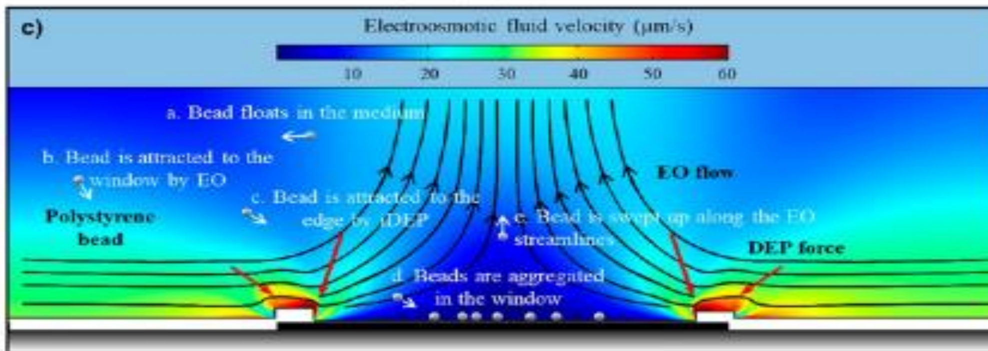

Figure 8: (a) 1 µm polystyrene beads are pushed together under the influence of electro-osmosis inside the wells at 3 Vpp as the applied frequency is decreased from 10 kHz to 50 Hz. (b) Frequency and voltage dependence of the 1 µm polystyrene bead clusters in 100 µm windows. (c) COMSOL model of EO streamlines around the resist window[81].

2.3.4 : Template Electrokinetic Microassembly of 5 µm Beads inside Windows.

As we discussed in previous sections, at applied frequencies below 10 kHz, the 1 µm beads will fill the windows while under the influence of electro-osmosis. However, 5 µm beads under the same range of frequencies were observed to aggregate at the edges of the windows under the influence of the positive iDEP forces rather than in the windows because larger beads are more inertial and less influenced by the flow streamlines and more influenced by DEP forces that depend on the cube of particle radius. One strategy to facilitate the filling of windows by 5 µm beads is to allow some of the polystyrene beads to sediment inside the windows. These initial bead clusters inside the windows will later serve as areas of higher electric field intensity when the pDEP force is activated and will facilitate the assembly of the microbeads inside the windows. . Figure 9 a presents a COMSOL simulation of the iDEP forces for a cluster of polystyrene microbeads inside a window. Once the beads have been successfully localized in the wells, gaps, and trenches under the nDEP force, and once the pDEP force is activated, at this point, there is a competing pDEP influence between the cluster of the beads inside the window and the resist edge of the window (both regions serve as areas of high electric field intensity). Figure 9 b demonstrates the observed movement of a 5 µm bead traveling from a gap toward a growing cluster of beads inside a well. The movement of the beads from the edge toward the centers of the wells is assisted by the electro-osmotic flow whose streamlines are simulated in Figure 9 c.

Thus, to fill the windows in the resist with 5 μm beads, one can start with depositing of the bead suspension over the electrode array and waiting for several minutes for gravitational sedimentation to take place and then applying 1 MHz frequency to utilize negative DEP (see Figure 6). That initial step will ensure that some beads will already be inside the windows. Following that nDEP step with lowering frequency to 1 kHz to start positive DEP will result in filling the windows with 5 μm beads as seen in Figure 7 a.

To avoid the need for gravitational sedimentation of the 5 μm beads, we explored an alternative strategy for attracting them to the windows. It was observed that when 1 μm beads were added to the 5 μm bead suspension, these smaller beads would begin filling the windows under the influence of ACEO at a frequency of 1 kHz. The formation of 1 μm clusters then serve as areas of high electric field intensity, which subsequently allow for the successful attraction of 5 μm beads to the windows under positive DEP. Figure 9 d illustrates this process of attracting 5 μm beads with the initial formation of 1 μm cluster using positive iDEP attraction. Figure 10 summarizes the interplay of the DEP and EO forces for 5 μm beads in the template electrokinetic assembly (TEA) process.

2.3.5. Permanent Entrapment of the Beads with Polypyrrole.

The permanent entrapment of 1 and 5 μm beads through polypyrrole electrodeposition is presented in Figure 11 a–c. Because the PPy deposition is initiated by a DC offset, only one side of the electrode experiences PPy deposition. Deposition on the other side can still be achieved by switching the live and ground wires to reverse the polarity of the DC offset.

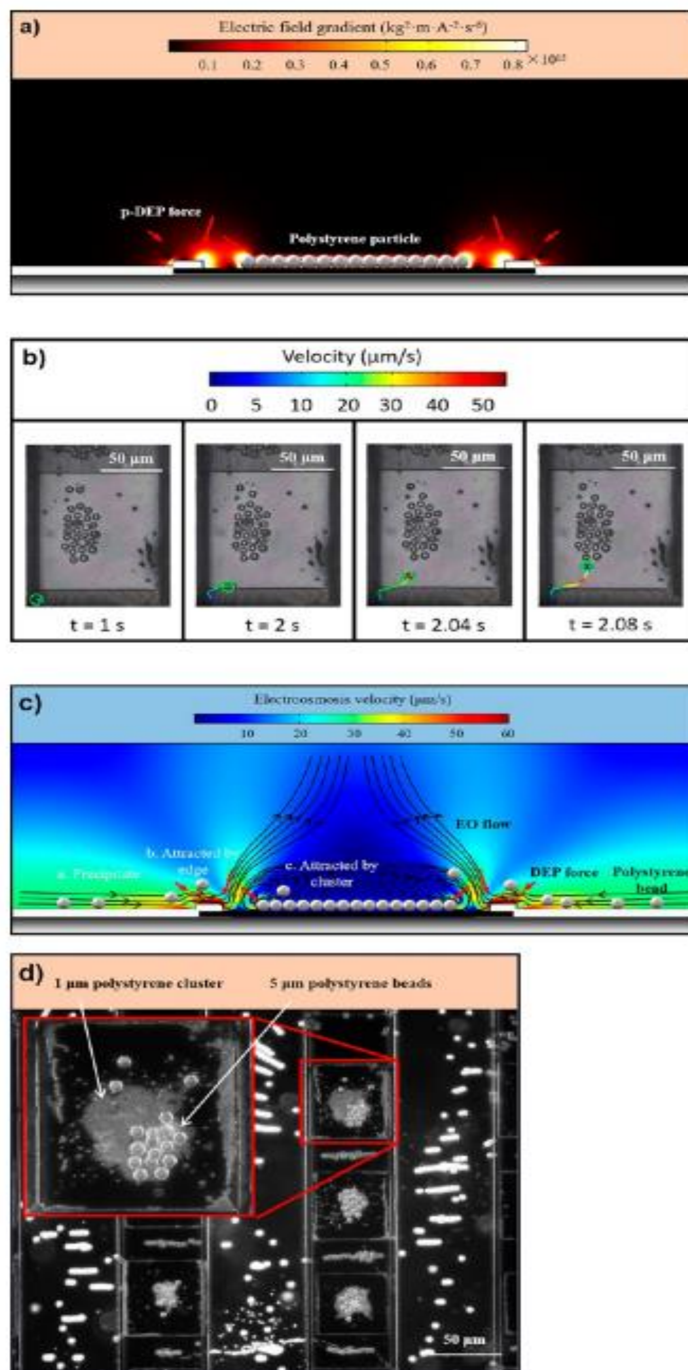

Figure 9: (a) COMSOL simulation result demonstrating two areas of high electric field gradients: around the edges of resist windows and around the particle cluster inside the window; (b) a series of optical micrographs tracing the movement of 5 µm bead toward the cluster of 5 µm beads inside the well under 1 kHz, 3 Vpp bias. (c) COMSOL model of EO streamlines around the resist window and cluster of the beads inside the window; (d) attraction of 5 µm particles by the cluster of 1 µm particles inside the wells[81].

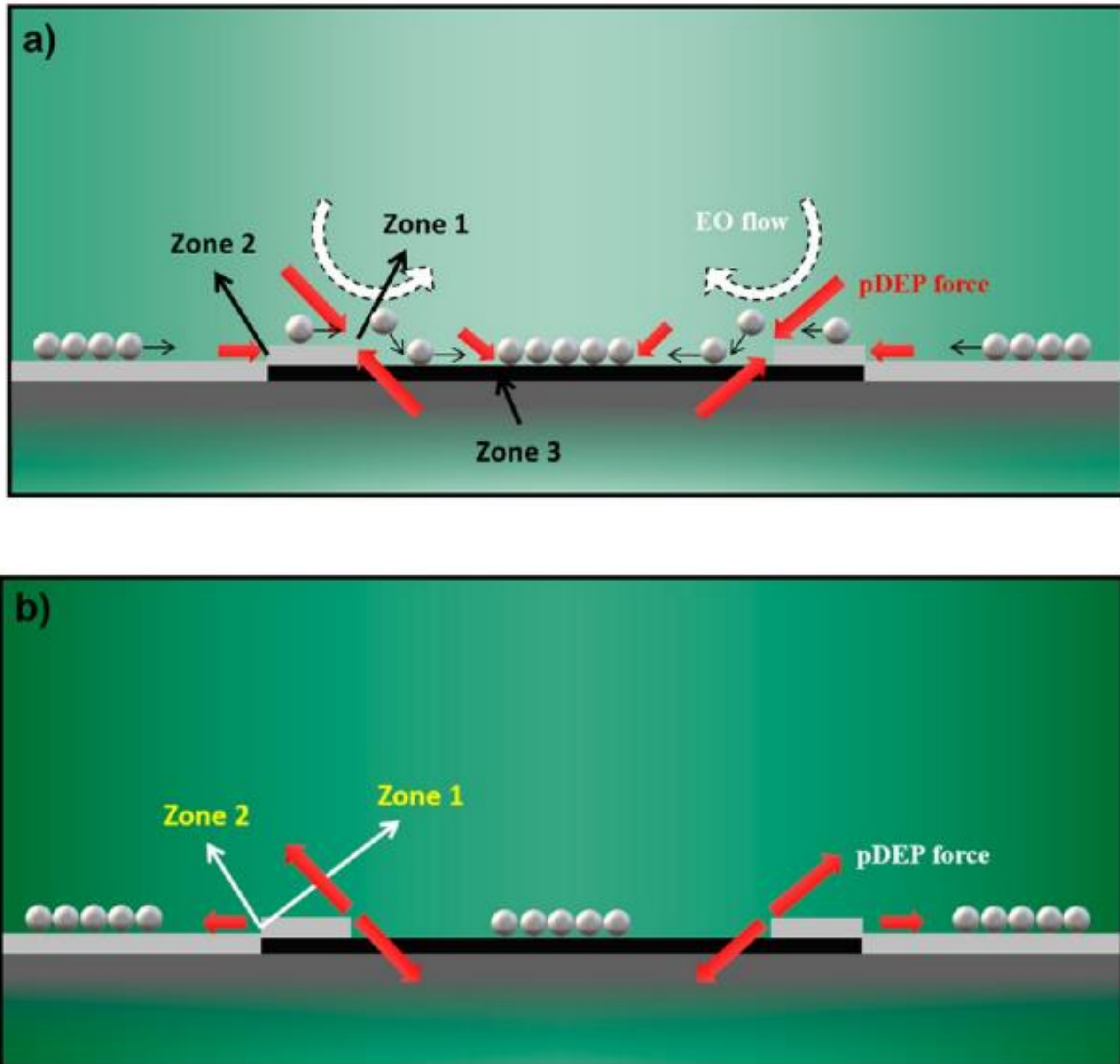

Figure 10: Mechanism of the guided electrokinetic assembly for 5 μm microparticles. The schematics represents a cross-section of the IDEA chip where the carbon electrodes are black, resist is gray, and the DEP forces are represented by red arrows and electro-osmotic forces by blue arrows. (a) Clustering of the 5 μm beads under the influence of n-DEP forces. (b) Schematics of the beads' motion under p-DEP forces and electro-osmotic (EO) forces that become significant under the low applied frequency. Zone 1 is the local maximum of iDEP forces at the inner edge of the resist well, Zone 2 is the local maximum of iDEP forces around the outer edge of the resist well, whereas Zone 3 is the local maximum for iDEP forces because of clustering of the polystyrene beads inside the wells[81].

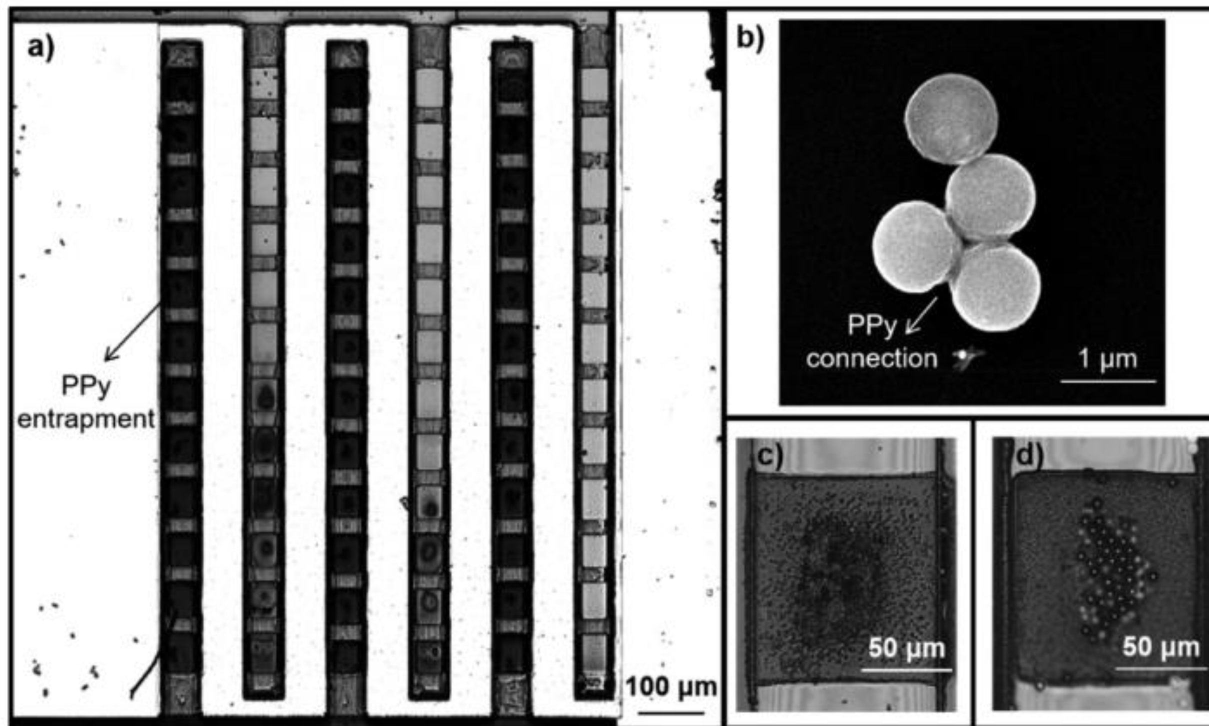

Figure 11: Entrapment of beads by PPy deposition. (a) Optical image of the IDEA with the polystyrene beads entrapped by PPy; (b) scanning electron microscopy (SEM) image of 1 µm bead agglomerate covered with PPy; (c) close-up of the well with PPy-entrapped 1 µm beads; (d) close-up of the well with PPy-entrapped 5 µm beads[81].

2.3.6: The Entrapment of Fluorophore Conjugated Beads

Enzyme-linked immunosorbent assays (ELISA) is a conventional technique that can detect protein analytes for the purpose of disease diagnosis. But it usually requires a large amount of time form loading, incubating, and washing samples[84]. However, the platform in this study can be used to detect specific protein more efficiently than conventional ELISA. In this case, we use 1um beads conjugated with antibodies(IgG) and fluorophore (Alexa) to prove the concept. The procedures used to prepare the conjugated beads are provided by Thermal Fisher Scientific[85].

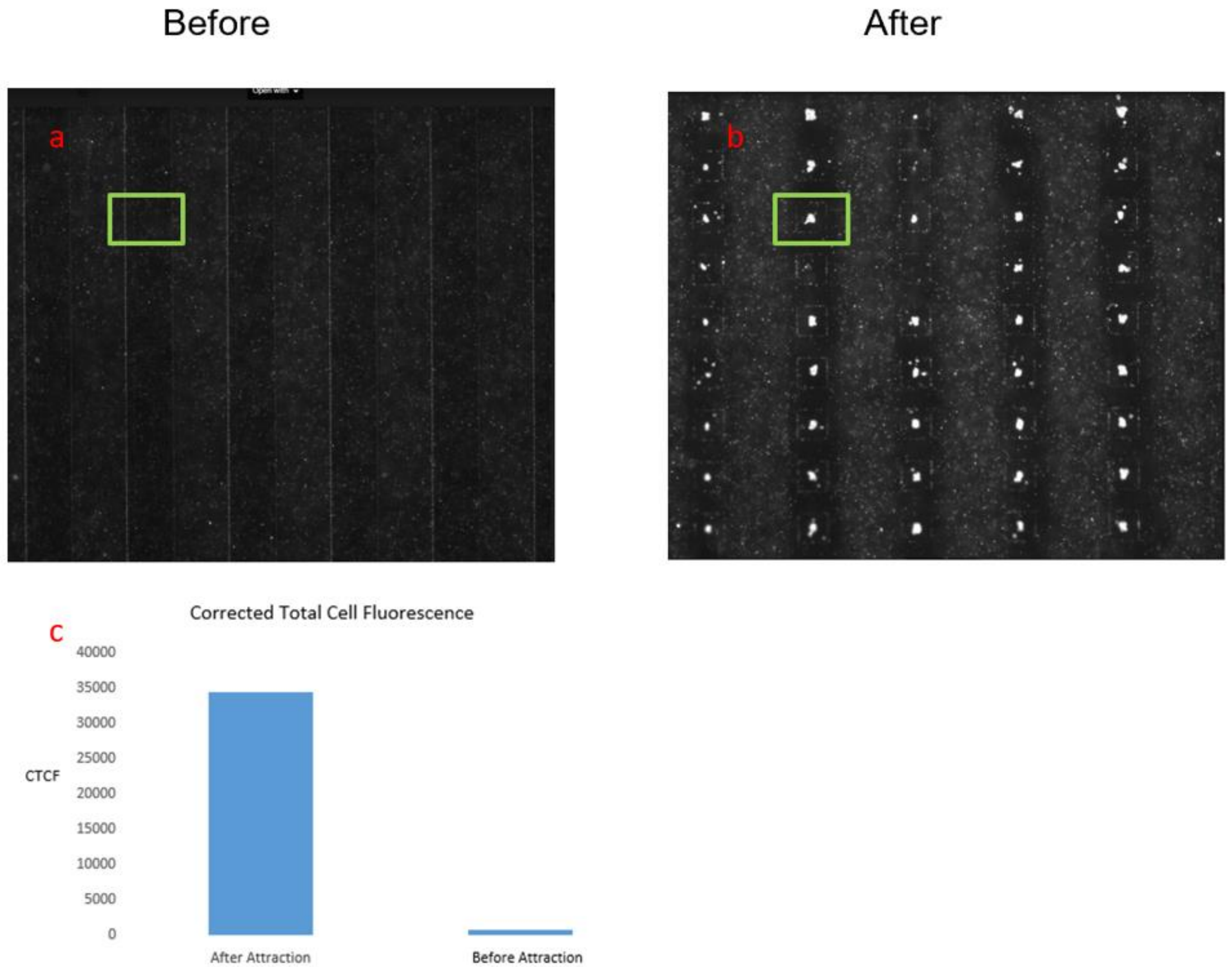

Figure 12: Entrapment of fluorophores conjugated beads before (a) and after (b) attraction; (c) The absolute value of Corrected Total Cell Fluorescence (CTCF) before and after entrapment.

According to Figure 12, even though the beads are spread evenly across the electrode, the signal of CTCF is extremely low. However, after the attraction the effect of EO (1kHz 1V peak to peak Voltage), the signal of beads concentrated inside the wells is enhanced dramatically.

Chapter 3

Characterization of the Positive and Negative Dielectrophoretic Ranges of Applied Frequency

3.1: Introduction.

The present work describes an artificial intelligence (AI)-based phenomenological approach that automatically determines the ranges of the applied frequency that cause positive and negative DEP for the population of 3-μm diameter polystyrene beads in deionized water. Specific crossover frequency can be calculated from the DEP Equations in the introduction part, setting the real part of K to be equal to zero. In this system, the electrical conductivity and permittivity of DI water and polystyrene beads would be required for such calculation. From the literature, we know the relative permittivity of DI water to be around 78 and relative permittivity of the latex beads to be around 2.5, while the electrical conductivity of DI water to be around 2 × 10−4 S/m[86]. The problem confronts the researchers trying to gauge the conductivity of the polystyrene microbeads, since polymer beads' conductivity is highly dependent on their functionalization and bead radius. The beads' electrical conductivity is not measured directly. Typically, the conductivity of the beads is deduced indirectly by observing the crossover DEP frequency and back-calculating the conductivity of the beads from the following equation:

$$K = \left(\varepsilon_p^* - \varepsilon_m^*\right)/\left(\varepsilon_p^* + 2\varepsilon_m^*\right) \qquad [6]$$

where ε_i^* stands for complex permittivity of the materials and subscripts p and m identify particles and suspension media, respectively [87]. Therefore, the described phenomenological approach of finding the cross-over frequency is critically important because it can't be predicted beforehand but can only be observed directly through experimentation.

Our AI-based automated approach involved a custom-developed closed-loop system where the function generator (that applied AC signal to the electrodes) was connected to the computer and Python program was used to change the applied frequency of the signal. The movement of the microbeads was digitally captured by the camera attached to the microscope and the resulting images were automatically analyzed to determine if the beads are moving towards the electrodes or away from the electrodes. On the basis of that determination, the applied frequency used by the function generator was algorithmically changed to a new frequency value and the analysis was repeated. The outcome of the automated analysis is the frequency ranges where DEP force is positive, negative, or too weak to cause significant particle motion.

The phenomenological approach to directed micro assembly detailed in this research will find application across many fields including microsystems and electronics, biotechnology, drug delivery, and tissue engineering.

3.2: Materials and Methods

3.2.1:Interdigitated Electrode Fabrication

The gold interdigitated electrodes arrays (IDEAs), used to generate non-uniform electric fields in this study, were fabricated via conventional photolithography and e-beam evaporation. Positive photoresist (Shipley) was spin coated onto a 4 inch silicon wafer (University Wafer, South Boston, MA, USA) at 3000 revolutions per minute (rpm) for 30 seconds, after an initial spin-coating at a speed of 500 rpm for 10 seconds, using a Laurell photoresist spinner (Laurell Technologies, North Wales, PA, USA). Next, the coated wafer was soft-baked on a hot plate (Dataplate, PMC, 732 Series, Dubuque, IA, USA) at 90 °C for 30 minutes. After soft-bake, the photoresist coated on wafer was exposed to UV light utilizing MA56 Mask Aligner (Karl Suss, Garching, Germany) for 4 seconds at an energy intensity of 10 mW/cm^2, through a photomask (CadArt, Bandon,OR, USA). Exposed photoresist was then removed by the deionized (DI) water rinse.

Temescal CV-8 E-beam evaporator (Airco Inc., Berkeley, CA, USA) was used to deposit metal layers. Following the deposition of a 300 Å first layer of Cr, a 3000 Å layer of Au were deposited onto the underlying chromium layer. Then the unexposed photoresist was dissolved in acetone. After this photoresist stripping step, only the metals that covered the wafer, rather than photoresist, was left in so-called lift-off process. The resulting electrode system, presented in Figure 13, consists of 12 interdigitated fingers separated by the gaps of 70 μm.

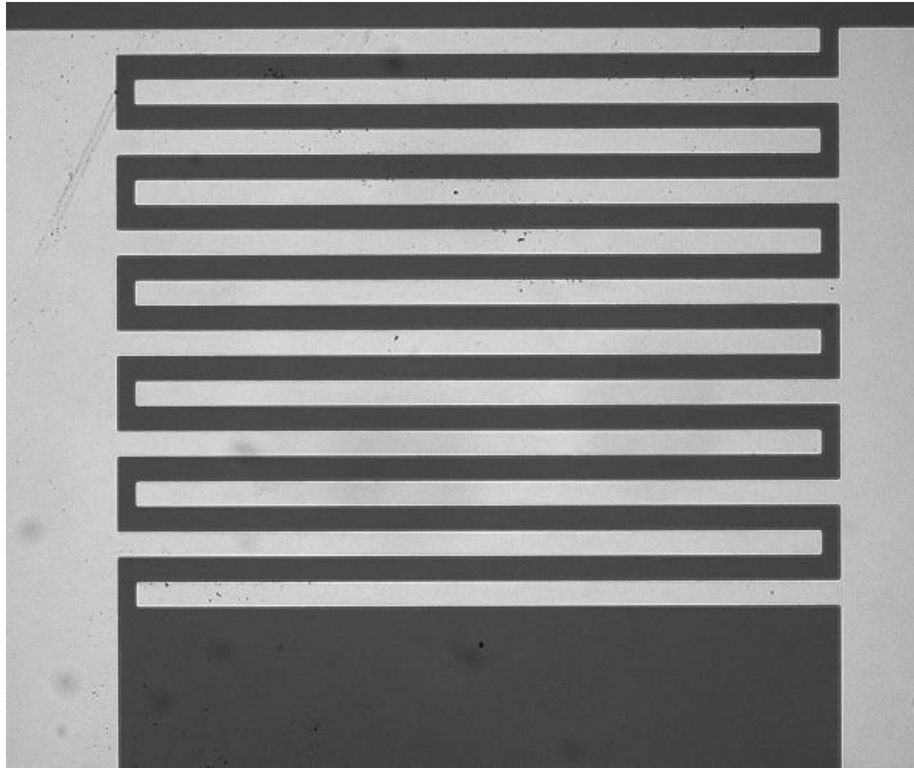

Figure 13: The schematic of the IEDA. The gold electrode fingers (light against the dark background of the substrate) have the spacing between the adjacent fingers of 70 μm[88].

3.2.2: Experimental Setup

The IDEA, with wire contacts soldered by indium, was connected to a function generator (Stanford Research System, CA, USA) as illustrated in Figure 14. The double-sided adhesive tape (3M, MN, USA) was cut to construct a polymer cage to confine liquid with suspension of microbeads. The peak-to-peak voltage and frequencies applied by the function generator are controlled via digital input from the computer via Standard Commands for Programmable Instruments (SCPI) programming language and the Virtual Instrument Software Architecture (VISA) API.

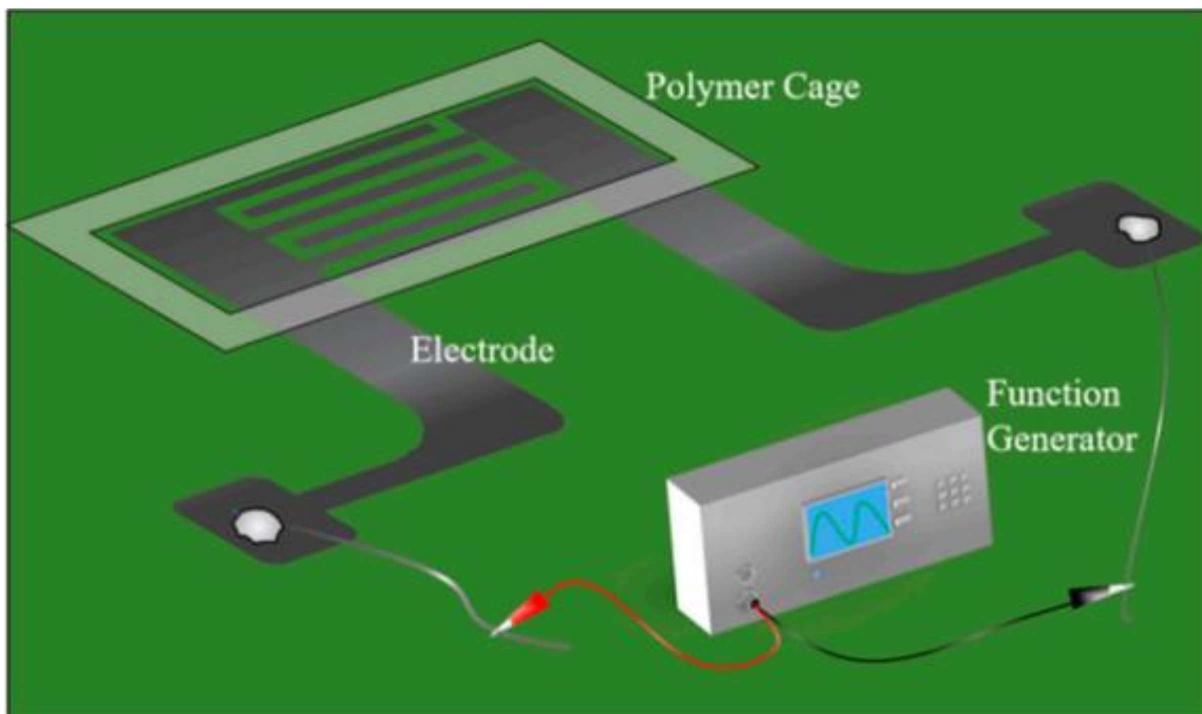

Figure 14: Sketch of the experimental setup including IDEAs connected to a function generator[88].

Aqueous solutions of 3 μm diameter carboxyl modified latex (CML) polystyrene beads (Thermo Fisher Scientific, Invitrogen, MA, USA), which was originally at 4 wt% concentration, was diluted to a new concentration of 0.39 wt% in DI water by first placing the original solutions in a centrifuge (Eppendorf, Germany) for 20 minutes at 2000 rpm, then removing the supernatant with pipette, and eventually remixing the remaining beads with pre-calculated amount of DI water.

A 10 μL droplet of prepared beads suspension was pipetted onto region of IDEA surrounded by polymer cage, then a 3V peak-to-peak sinusoidal voltage with a sequence of discrete frequencies was applied to study the motion of the beads. A Nikon Eclipse microscope

(Nikon, Japan) and SPOT Basic video editing program (SPOT Imaging, MI, USA) were used to observe and record the movement of the particles.

3.3: Software Architecture and Methodology

3.3.1: Architecture Overview

As Figure 15 illustrates, we have implemented the monitoring of the experimental testbed (a suspension of the microparticles on the IDEA chip) where particles movements are captured by the camera and that information is passed in the digital form to the computer where the particles are recognized, their positions are detected, and computer algorithm is run to compare the mean present location of the particle cloud with the mean location of the particle cloud as captured in the prior frames. Based on the comparison of these mean past and present locations of the particle clouds, the function generator is given a command by the computer to either increase or decrease the applied frequency. Therefore, a real-time control and feedback of the embedded system is implemented that allows for the dynamic control of the movement of the particles. Specifically, our system tracks the overall particle movement by a watching window W which is maintained from the result of Particle Detection & Feature Extraction for each new frame. Our system analyzes W with Particle Movement Determination and Adjustment Determination to determine the amount of adjustment made to the Function Generator. Subsequently, the system applies the predetermined changes (such as step up or step down in the applied frequency) to the experimental testbed. We will describe each of the functional components below.

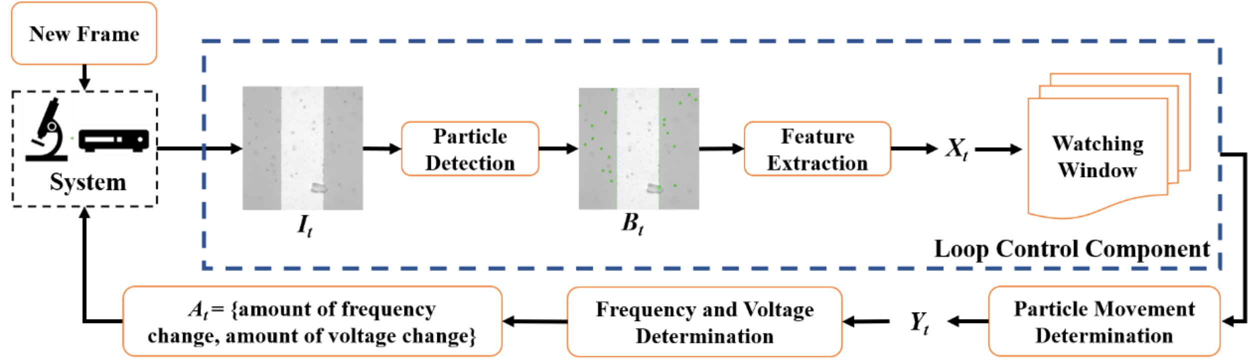

Figure 15: Architecture of the Feedback Control System Design[88]

3.3.2: Particle Detection and Feature Extraction

For each frame $I_t \in I$, we utilize the *Hough Circle Detector* [29] to detect particles from each sliced image I_t. We leverage the implementation of the Hough Circles Detector in OpenCV which can perform Hough Gradient Method on detecting the circle-shaped objects on grey-scale images. To ensure the performance of particle detection across different experimental setups, we tune the four parameters (*param_1, param_2, min_radius, max_radius*) provided by OpenCV's implementation. Specifically, the parameter *param_1* is for adjusting the internal Canny detector threshold while the parameter *param_2* is for modifying the center detection threshold. We denote the result of detecting particles as B_t which is a container of a collection of detected particles $\{P_1, P_2, \ldots P_N\}$ where N is the total number of detected particles. In this paper, we denote the particle detecting process using function F. Thus, the relation between a new frame I_t and a container B_t can be written as: $F(I_t) = B_t =$

$\{P_1, P_2, \dots P_N\}$, where each particle is represented with the center 2-D coordinates (i.e. $P_n = \{x_n, y_n\}$).

We then transform each container B_t into a corresponding feature X_t. In our paper, two assumptions are made. First, we assume that the movement of particles (moving toward/away from the electrodes) can be captured and represented by the values derived from formulaic methods. Second, since the direction of DEP force is perpendicular to the electrodes installed in our testbed, we only consider a particle's movement along the x-axis in our system. In our paper, we abstract this feature extracting process using a function G. In our system, we implement G by calculating the average absolute distance to the reference line where the reference line refers to a vertical line that stays in between and in the middle of two electrodes. We denote the x-coordinate of the reference line as r and use it along with the x-coordinate of each particle in a container $P_n = \{x_n, y_n\} \in B_t$ is used to calculate the feature X_t. In short, the relationship between a new frame I_t to the extracted feature X_t is illustrated as:

$$X_t = \mathrm{G}\big(\mathrm{F}(I_t)\big) = G(B_t) = \sum_{n=1}^{N} \frac{|x_n - \mathrm{r}|}{N} \qquad [7]$$

3.3.3: Particle Movement Determination

In order to determine the overall movement of particles at each timestamp t, our system performs a linear trend analysis by considering a subset of features between current frame and few frames prior. We define this set as a watching window $W = \{X_{t-k}, X_{t-k+1}, \dots X_t\}$, where k denotes the length of W and is a tunable system parameter in our system. Our

particle movement determination process begins with post-processing the features with Missing-Value Sampling and Data Smoothing. As our particle detector might end up not detecting any particle for I_t, we need an alternative value of X_t for minimizing the negative influence of missing values in our linear trend analysis. To be more specific, we sample the missing value by averaging the features u frames before X_t ($\{X_{t-u-1}, X_{t-u}, \dots X_{t-1}\}$), where $u \leq k$. The determination of u depends on the velocity and frame rate of the testing setup.

Next, we perform the *Data Smoothing* on W to decrease the influence of noise or random errors and to acquire a cleaner trend during our linear trend analysis later. Specifically, we perform linear convolution on $W = \{X_{t-k}, X_{t-k+1}, \dots X_t\}$ with an unweighted filter. The 1's array performs as an unweighted filter and u is a tunable parameter for manipulating the level of smoothing.

Finally, our *Particle Movement Determination* adopts a *Linear Trend Model* (LTM) in determining the overall movement of particles. In our system, we perform LTM over the features $\{X_{t-k}, X_{t-k+1}, \dots X_t\}$ in the watching window W to derive the trend of the data. Specifically, we first convert the features in W into a set of data points where each data point corresponds a timestamp x to a feature X_{t-k+x} (e.g., (x, y) = (0, X_{t-k}), (1, X_{t-k+1}), ..., (k, X_t)). Then, LTM applies the least-squares regression to generate a unique trend line represented by equation $y = bx + c$ that minimizes the vertical distance over the data points, and the coefficient, b, is calculated according to the equation below:

$$b = \frac{\sum(x-\bar{x})*(y-\bar{y})}{\sum(x-\bar{x})^2} \qquad [8]$$

The coefficient b represents the velocity (e.g., the slope of the regression line) of overall particle movement. The system uses b and a decision threshold δ to classify the macroscopic

motion of particles with a categorical label Y_t. If $|b| \leq \delta$, the system classifies the motion as NO_DEP because as b is too little to be considered as a DEP polarity. In the case where $|b| > \delta$, the system classifies the DEP's polarity as either Positive-DEP or Negative-DEP according the practical experimental setup (i.e., can be flipped).

3.3.4: Feedback Control Design

The system we propose is a real-time closed loop controlling system, also known as a feedback control system. The proposed feedback control design is illustrated in the Figure 15. In our system, the process variable is the motion of particles. Therefore, with a predefined sampling rate m, our system repeatedly collects the new frame from the sensory camera and performs the Particle Detection & Feature Extraction for each frame I_t to acquire a feature X_t. The new feature X_t is then inserted to the end of the watching window W which is realized as FIFO (First-In First Out) Queue with k as the size in our system. Next, if not in SETTLE state, our system performs the Particle Movement Determination over the watching window $W = \{X_{t-k}, X_{t-k+1}, \dots X_t\}$ and acquires Y_t indicating the current state of the testbed. Then, according to Y_t and b, our system calculates the amount of frequency or voltage to be adjusted to the testbed.

Ultimately, these adjustments are encapsulated as a command packet and sent to the function generator. Once the function generator is adjusted, our system will enter the SETTLE state for a period. SETTLE is the time required for the system to detect the change in movement of particles due to the function generator change, and it is calculated based on two values: the particle response time and the system response time. The particle response

time refers to the time needed for particles to show the effect of a function generator change, and the value depends on the environmental setup. System response time refers to the time needed for the proposed computer-vision based system to detect the movement of particles, which depends on the length of the watching window, k, as we discussed in the section above. In general, a larger k will require longer system response time. In SETTLE state, our system just keeps acquiring inputs from the camera and performing Particle Detection and Feature Extraction. In Non-SETTLE state, our system will additionally make decisions and adjustments according to the results from Particle Movement Determination.

Table 1: Pseudo code governing the control loop

Algorithm 1 Pseudo code governing the control loop.

```
   Data: particles, watching_window, detected_movement, not_move_count system initialization;
1  while not_move_count < threshold do
2        Detect particles in the current frame;
3        Append detection results to the watching_window;
4        Analyze the direction of particle movement and save result to detected_movement;
5        if |detected_movement| < threshold then
6              STATE <= NOT_MOVE;
7              not_move_count += 1;
8        else if detected_movement > 0 then
9              STATE <= POSITIVE_DEP;
10             function_generator.decrease();
11       else
12             STATE <= NEGATIVE_DEP;
13             function_generator.increase();
14       end
15  end
```

3.4: Results

3.4.1: Particle Detection

The cyber-physical system was setup and run as detailed in sections 2 and 3 above. As the test proceeded, the program converted the live video stream (transferred from the optical microscope via the digital camera) into still frame images. The OpenCV package, utilizing the Hough Circle Detector function, identified beads within each frame. Figure 16 below shows examples of bead detection.

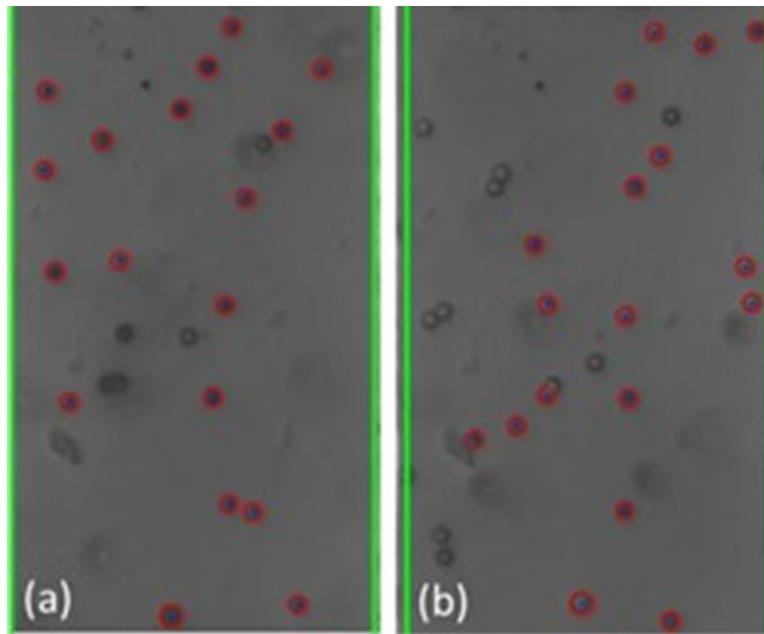

Figure 16: Examples (a) and (b) of bead detection using The Hough Circle Detection function of the OpenCV package. The recognized beads are circled in red. The green lines identify the frame window nearly coincident with the edges of the electrodes[88].

Based on the analysis of the individual still frame images, it is estimated that the OpenCV package was successful at accurately identifying an average of 20-30 percent of the beads in each frame, typically with higher bead detection as shown in Figure 16.

This detection rate provides an adequate sampling of bead position for each frame to estimate overall movement of the beads. Experimentally, bead detection rate and accuracy was found to be dependent on several different factors including the amount of illumination

and focal settings of the optical scope as well as the density and size of the beads. In general, larger beads at lower concentration led to greater bead detection rate and accuracy. This is thought to be due to the fact that the Hough Circle detector function utilizes pixel color gradient to detect the beads and larger beads provide a larger circumference for the program to detect such gradient. Additionally, lower bead concentration led lower likelihood of agglomeration formation which hindered the ability for OpenCV to recognize their shape as circular. Figure 16 presents examples of the beads in close proximity that were not recognized as individual beads. Additionally, given that OpenCV uses color gradient to detect the edges of the bead, optical settings which provided high contrast between the beads and the silicon chip background yielded better particle detection and accuracy. This is illustrated in Figure 17 below.

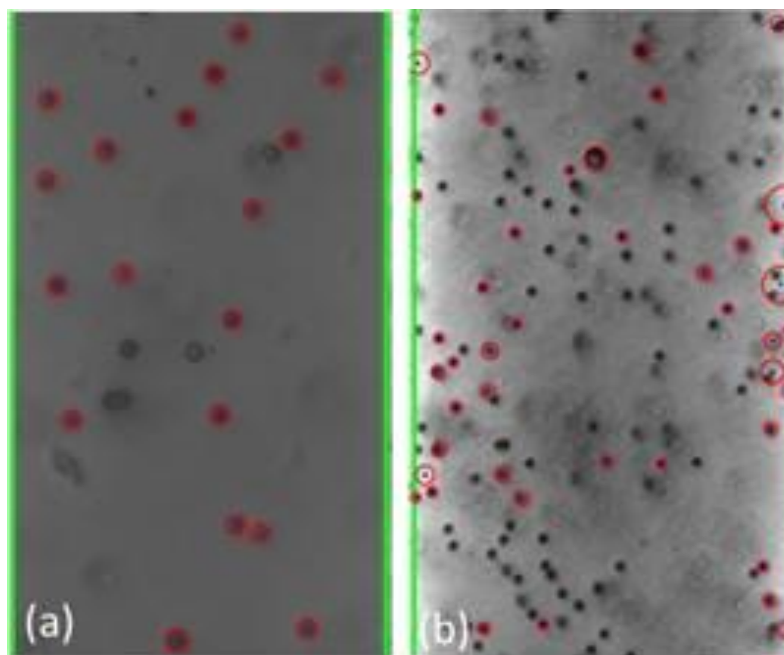

Figure 17: Different bead detection efficacy between samples (a) and (b) depended on bead size and illumination conditions[88].

3.4.2: Bulk Cloud Behavior

The cyber-physical system was set up as detailed in the previous sections and two trials were performed with 3μm diameter beads. The video segments of the bead movement under the influence of the applied voltage signal with a given frequency is provided as a Supplementary Material accessible online. The program calculated the average absolute distance of all detected beads from the center of the electrode gap for each frame. The results of each trial, overlaid with the changes to the frequency of the applied electric field, are shown in Figure 18 and 19 below.

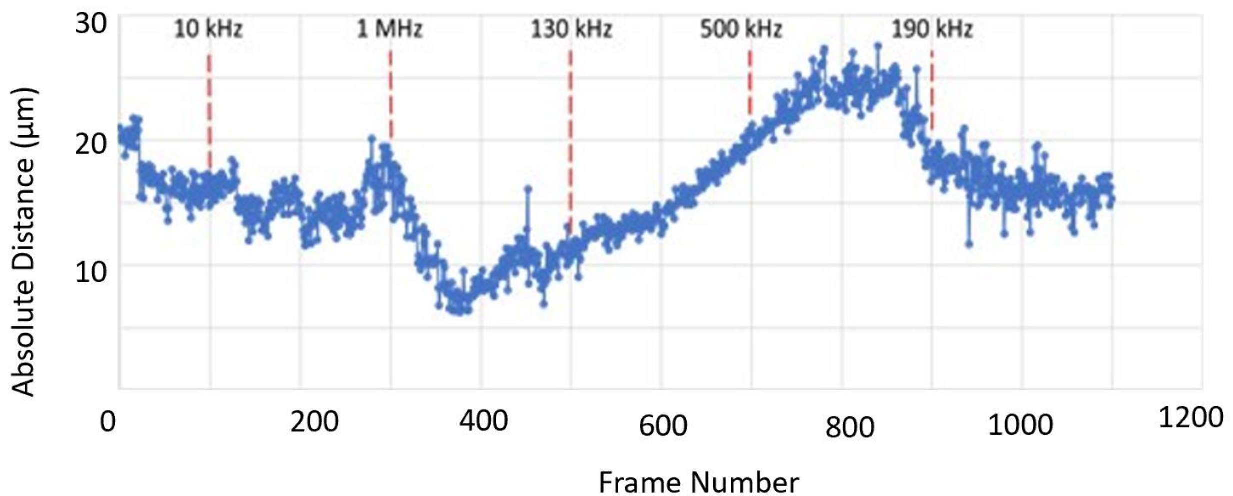

Figure 18: Average Absolute Distance from Center by Frame (Trial 1)[88].

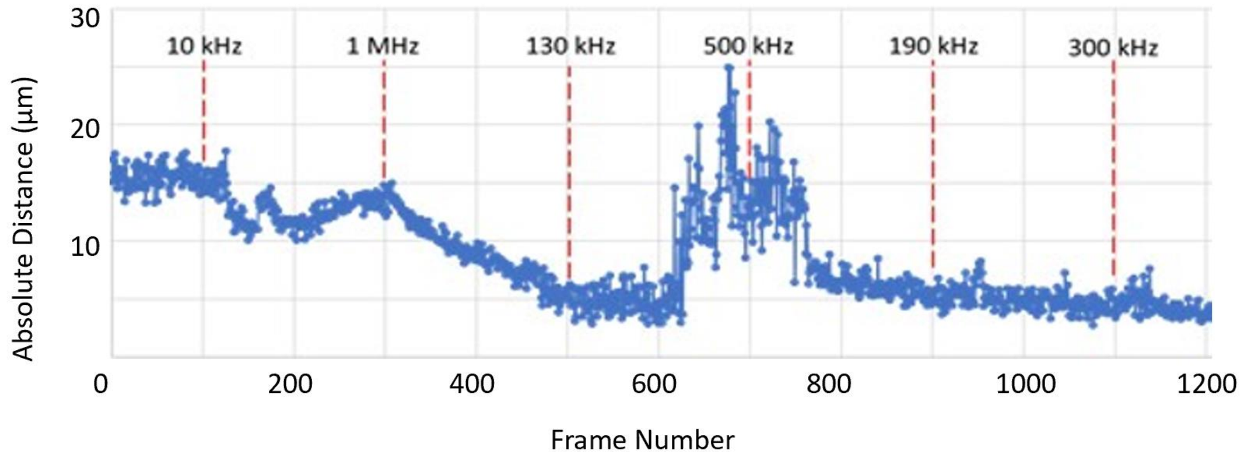

Figure 19: Average Absolute Distance from Center by Frame (Trial 2)[88].

In this analysis, increasing absolute value from the center of the testbed indicates the particles are moving toward the edges of the electrodes, a result of attractive forces such as positive DEP and EO. Conversely, decreasing absolute value from the center indicates the beads are moving away from the surface of the electrodes in response to an induced repulsive force under negative DEP. The graphical results from both trials shown above clearly depict regions of attractive and repulsive force. For example, in both trials frequency increase from 10 kHz to 1MHz resulted in a decrease in the beads' absolute distance, indicating a change from attractive to repulsive force. The bulk response of the beads indicates attraction at lower relative frequency and repulsion at higher frequencies which aligns with the established literature on DEP force [89]. As the applied frequency approached the crossover frequency, the magnitude of bead movement decreased.

The results above also indicate a delayed bead response to changes in the applied frequency. This is thought to be the result of residual bead momentum that must be overcome prior to a reversal in bead movement. This interesting result is important in understanding the

fundamental physics of this DEP-based particle manipulation system. Such time-delayed response would need to be accounted for when designing such a system for a particular application.

3.4.3: Individual Particle Behavior

Still frame image results from trial 2 were analyzed to assess the response of individual beads to changes in the frequency of the applied electric field. Figures 20 through 23 below show subsequent still frame images from select regions of interest within the Trial 2 results. Specific beads are indicated within each frame for clarity.

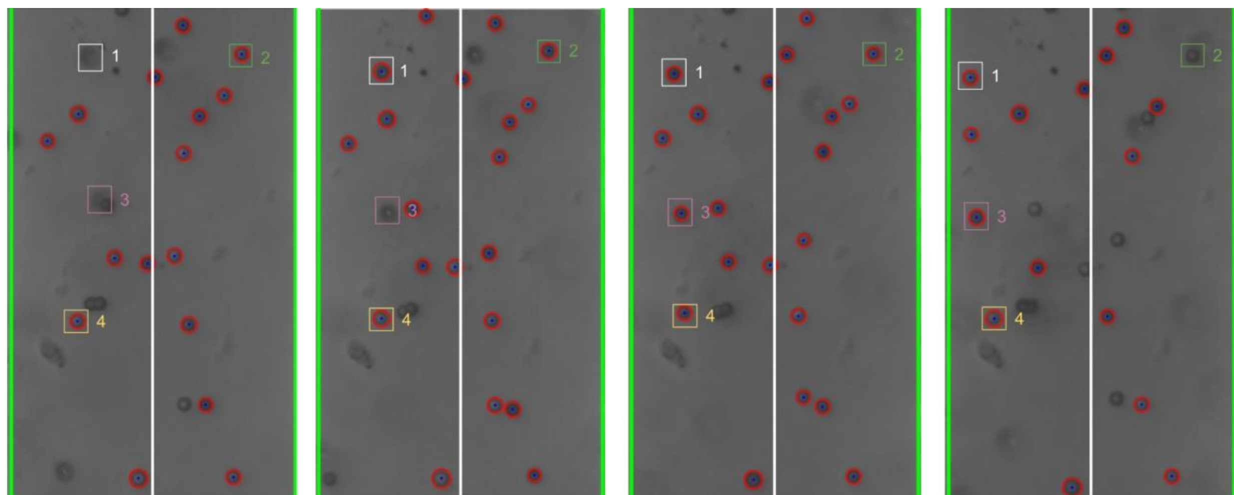

Figure 20: Individual bead movement during trial 2 from frames 195 to 298[88].

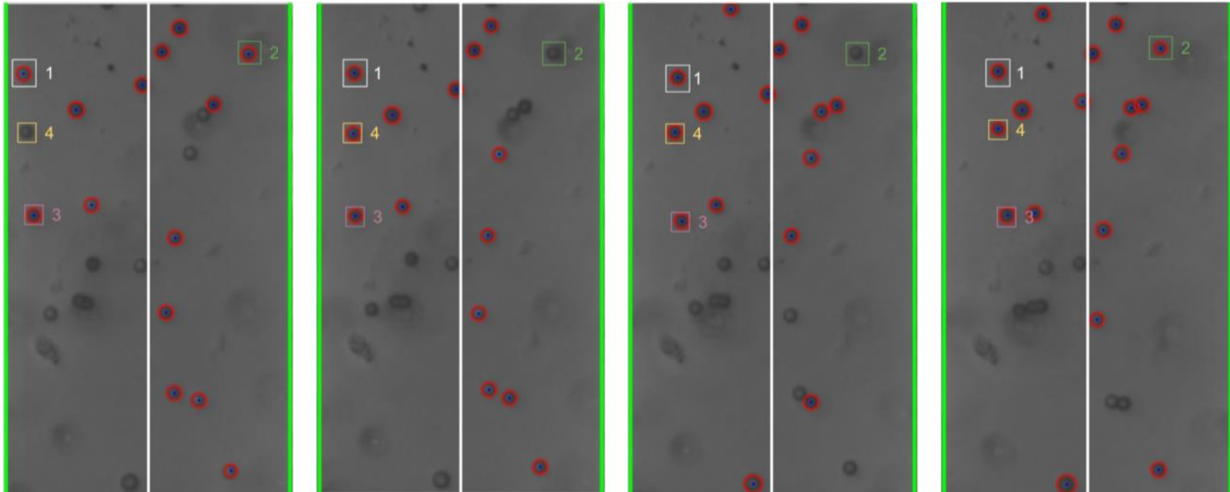

Figure 21: Individual bead movement during trial 2 from frames 300 to 340[88].

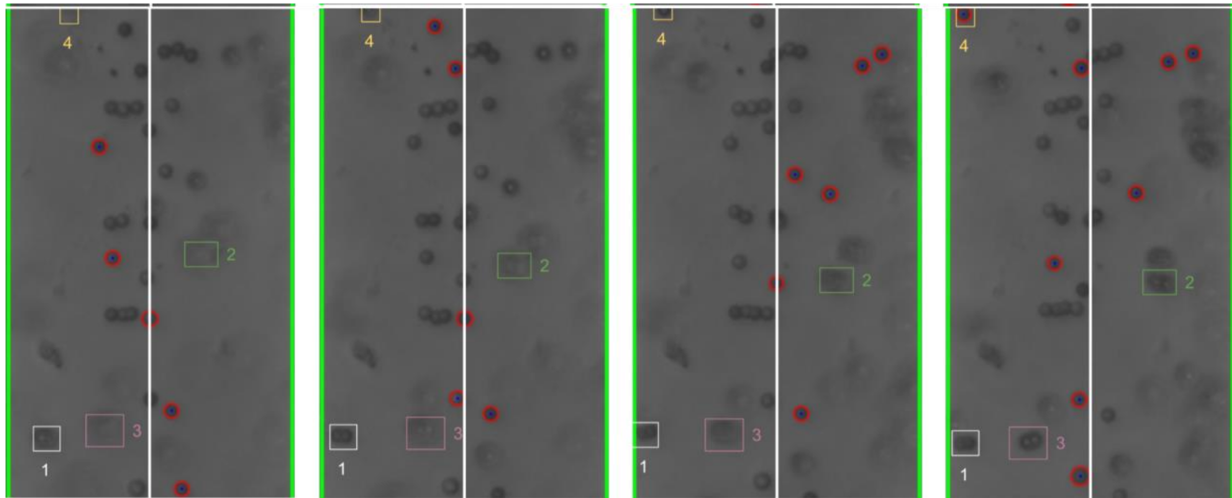

Figure 22: Individual bead movement during trial 2 from frames 570 to 685[88].

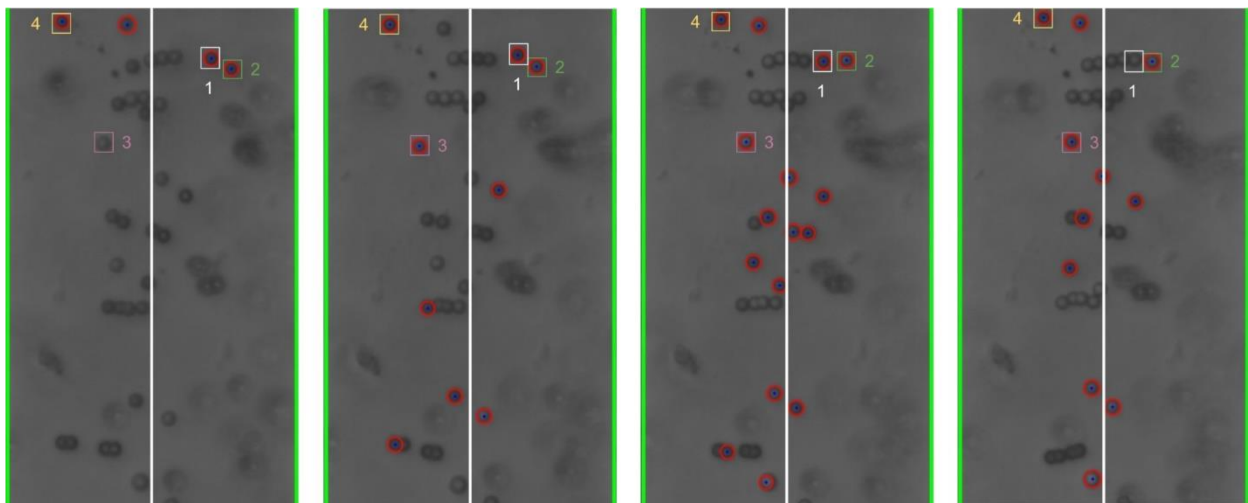

Figure 23: Individual bead movement during trial 2 from frames 735 to 812[88].

As the images indicate, individual beads responded to changing input frequency. In Figure 21 the beads move toward the edges of the electrode at an applied frequency of 10 kHz. Additionally, when the frequency was increased to 1 MHz, the same beads can be seen moving away from the electrode as shown in Figure 23.

3.4.4: Correlation of Bead Cloud Behavior and Individual Bead Position

3.4.4.1: Bulk Motion

The individual bead analysis correlates closely with the assessment of the cloud bead behavior made by the cyber- physical system. For instance, in Trial 2 the steady decrease in average absolute distance which occurred after the frequency was set to 1 MHz as shown in Figure 19 correlates to individual bead movement toward the center of the electrode gap in Figure 23.

This result supports the assertion that the proposed algorithmic artificial intelligence program can effectively estimate the response of beads to varying input frequency. The proposed system successfully identified frequency regimes in which the beads were attracted to the electrode surface due to positive DEP and EO, as well as regimes in which the beads were repelled from the electrodes due to negative DEP. Results from the system testing revealed a lag in particle movement in response to changes in frequency. This is seen in Trial 1 when the frequency was changed to 500 kHz at frame 700 as compared to the more immediate particle movement at frame 300 when frequency was changed to 1 MHz. This lag is thought to be the result of particle momentum in relation to the strength of the DEP force generated at a given frequency. 1 MHz produces strong negative DEP which more quickly overcomes the inertia of the moving particle and results in a rapid change in direction. Alternatively, a frequency of 500 kHz produced a weaker negative DEP force. As a result, the

plot shows a gradual slowing of the particles before final reversal of direction roughly 100 frames after the change to frequency was made.

3.4.4.2: Regions of DEP Influence

As the applied frequency approached the theoretical crossover frequency, the DEP forces exerted on the beads becomes weaker, resulting in slower bead movement. Additionally, DEP force is strongest at the surface of the electrode and becomes weaker as distance from the surfaces increases. As a result, as the applied frequency approaches the crossover frequency, the response of beads further from the electrodes was diminished. This can be seen in the relative magnitude of particle motion in the individual still frame analysis (Figures 19 to 22) as well as the leveling-off of average absolute distance in Figure 19. Analysis of the bulk particle movement as a function of the applied frequency indicates that when the frequency is increased to 1MHz the distance to the center decreases sharply pointing to negative DEP (nDEP) and indicating that the crossover frequency is below 1 MHz. Meanwhile, at 500 kHz there is still an attractive influence since the distance from the center is increasing (pDEP). Therefore, the crossover frequency is between 500 kHz and 1 MHz. While we can't calculate the exact cross-over frequency, because the surface conductivity of the CML modified polystyrene beads is unknown, we can conclude that our range of cross-over frequency is consistent with the data for cross-over frequency of polystyrene microbeads found experimentally by other researchers[90][86].

The cyber-physical system was successful at identifying a frequency range in which little to no bead movement was detected, indicating the DEP crossover frequency exists somewhere

within the range. Additionally, the system successfully identified frequency regimes in which positive and negative DEP force was strong and resulted in associated bead movement. Bead-to-bead interaction and the formation of pearl chains, as described in the following section is a primary limiting factor in the system's ability to further refine these regions of DEP influence.

The cyber-physical system was successful at identifying a frequency range in which little to no bead movement was detected, indicating the DEP crossover frequency exists somewhere within the range. Additionally, the system successfully identified frequency regimes in which positive and negative DEP force was strong and resulted in associated bead movement. Bead-to-bead interaction and the formation of pearl chains, as described in the following section is a primary limiting factor in the system's ability to further refine these regions of DEP influence.

3.4.5: Bead-to-Bead Interaction

Previous research has established that in addition to DEP and EO force, particles within an applied non-uniform electric field experience bead-to-bead attraction and form what is known as "pearl chains" which align along the electric field lines [91].

These pearl chains can be seen within the individual still frames images such as Figure 24 below.

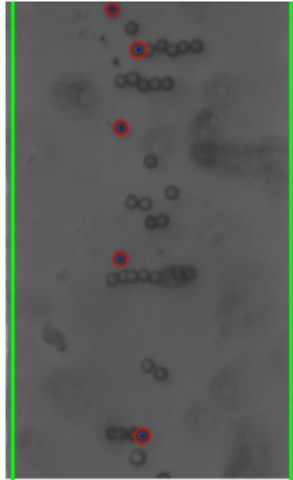

Figure 24: Pearl chain formation as a result of bead-to-bead interaction[88].

The formation of pearl chains as a result of bead-to-bead interaction impacts bead response to DEP force. As the pearl chains grow, the motion of such particle chains are inhibited due to inertia and the increased drag force.

Chapter 4

Step-Wise Deposition Process for Dielectrophoretic Formation of Conductive 50-Micron-Long Carbon Nanotube Bridges

4.1: Introduction

Carbon nanotubes (CNTs), high-aspect ratio tubular carbon structures [92], have drawn considerable interest due to their extraordinary physical, mechanical, and electrical properties [8]. CNTs are often used for the enhanced performance of electronic devices such as chemical and biological sensors [93], field-effect transistors [94] [95][96], energy storage systems [97], computing devices [98][99], and conductive interconnects[100][101]. Therefore, the integration of CNTs onto predetermined positions in micro- and nanosystems is a critical technology that has been extensively studied [102][103][104][105]. A variety of techniques have been developed to assemble or manipulate individual CNTs or CNT bundles onto desired electrode locations. For example, an atomic force microscope (AFM) tip was used to handle the conveyance of a single multiwalled carbon nanotube to a specific location[106], the capture of nanotube bundles was carried out by magnetic field[107], a combination of conventional and optically induced dielectrophoresis was used to create a line of CNTs between two electrodes[108], CNT transfer technology was developed to transfer CNT bundles [109], CNTs were collected in microgrooves via fluidic assembly[110], and photosensitive chemically binding agents were used to secure CNTs to specific sites. However, the majority of these techniques are slow, laborious, and expensive, and in many cases the aligned CNTs do not produce conductive bridges. In the present work, we describe

a step-wise process that can produce conductive bridges, selfassembled out of a CNT suspension and constructed within the high field areas between adjacent electrodes under the influence of dielectrophoresis (DEP).

As the distance between adjacent electrodes increases, so does the difficulty in creating conductive bridges made of nanoparticulates, as the bridges tend to branch into dendritic structures away from the electrodes, as observed previously[111]. Many researchers have bridged gaps reaching submicrons to several micron meter distances, sizes comparable to the lengths of the CNTs[52][112][113][114][115]. Researchers have also created dense forests of nanotube bridges between electrodes that were 25 microns apart[116]. Here, we report for the first time on the process of creating conductive CNT bridges spanning over 50 microns. In order to achieve this result, we employ the technique of step-wise DEP deposition described below.

4.2: Materials and Methods

4.2.1: Fabrication of IDEAs

The carbon interdigitated electrode arrays (IDEA) (utilized to generate the nonuniform electric field and form the conductive CNT bridges via DEP attraction and alignment) were fabricated with the standard lithographic process using photosensitive SU-8 resin[52], followed by pyrolysis in a nitrogen environment to convert the photo-patterned resist precursor into glassy carbon electrodes [25]. Each IDEA consisted of three electrode finger pairs, as seen in Figure 25. The width and length of each individual electrode finger was 120

μm and 1200 μm, respectively. The distance between the adjacent parallel electrode fingers was 120 μm, and the smallest distance between the electrodes (at the tip of the electrode finger) was 50 microns.

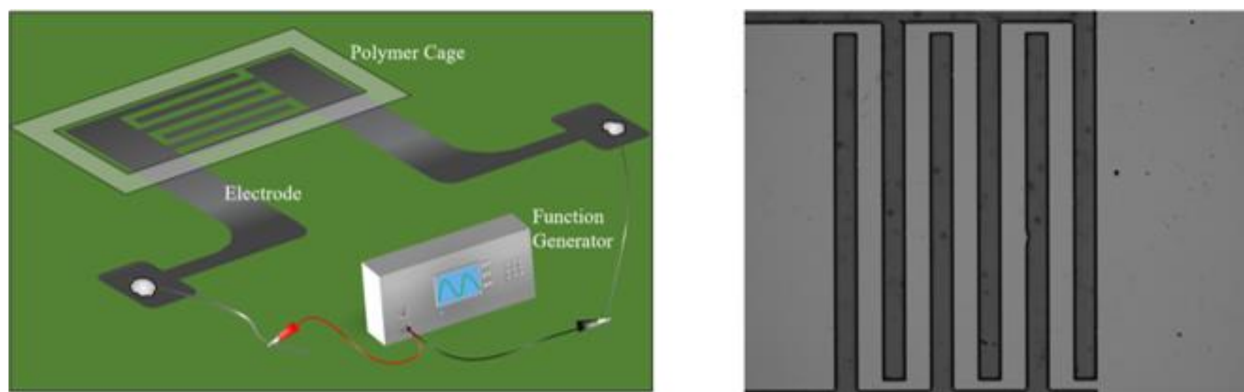

Figure 25: Experimental Setup (**left**) and Interdigitated Array of carbon electrode fingers 120 micron wide with 120 microns inter-electrode spacing (**right**)[117].

SU-8 2025 photoresist (Microchem Corp. Ltd, Westborough, MA, USA) was spin coated onto a 4" silicon wafer covered with 1 μm thick thermal oxide layer (University Wafer, South Boston, MA, USA) using a Laurell photoresist spinner (Laurell Technologies, North Wales, PA, USA) at an initial speed of 500 rpm for 10 seconds, followed by 4000 rpm spin for 30 s. The soft-baking was carried out on a programmable hot plate (Dataplate, Pmc 732 Series, Dubuque, IA, USA) at 95 °C for 5 min. The wafer was then exposed through a photomask (CadArt, Bandon, OR, USA) to UV light at an energy intensity of 10 mW/cm^2 for 6s using the Karl Suss MA56 Mask Aligner (Karl Suss, Garching, Germany). The subsequent postbake procedure was performed on the same hot plate by initially heating the wafer at 65 °C for 1 min, followed by a 95 °C step for 5 min. The uncrossed-linked resist was washed away in SU-8 developer (Microchem Corp. Ltd, USA). The remaining cross-linked resist layer was then hot-baked at 150°C for 20 min. The carbonization of the IDEAs was performed by gradually

heating up the wafer containing them to 900 °C inside a pyrolysis furnace (Thermo Fisher Scientific, Waltham, MA, USA), within a nitrogen environment. The pyrolysis started at 25 °C for two h, followed by a 69 min ramp to 300 °C, where the temperature was held for one hour before a subsequent 90 min ramp to 900 °C, where the temperature was held again with a dwell time of one hour before being allowed to naturally cool to room temperature overnight. Individual IDEA chips were diced from the wafer. Indium solder was used to attach wires to the carbon IDEA chips. During the pyrolysis step, the polymer precursor shrinks laterally as the carbon electrodes are formed. Since the top of the electrodes shrinks to a larger degree than its base, the sidewall of the carbon electrode becomes tapered. This taper can be clearly seen in the high-resolution SEM pictures below.

4.2.2: Preparation of Carbon Nanotube Suspension

The CNT suspension was prepared by dispersing 0.005 g of CNT powder containing a mix of single-wall and multiwall nanotubes (Aldrich Chemistry, St. Louis, MO, USA) into 10-mL of isopropyl alcohol (IPA). The suspension was then centrifuged in an Eppendorf 5702 Centrifuge (Eppendorf AG, Hamburg, Germany) at 3000 rpm for 15 min. A pipette (Labnet, Edison, NJ, USA) was used to collect the supernatant with homogeneously distributed CNTs.

4.2.3:Preparation of Pyrrole Solution

A mixed solution of 0.1M pyrrole monomers (Aldrich Chemistry, St. Louis, MO, USA) and 0.1 M NaDBS (sodium dodecyl-benzene-sulfonate) (Aldrich Chemistry, USA) was prepared by

dissolving 0.693 mL of pyrrole monomers and 3.48 g of NaDBS into 100 mL of deionized (DI) water. The solution was stirred at room temperature for 20 min using a magnetic stirrer (Fisher Scientific, Hampton, NH, USA).

4.2.4: Deposition of CNT bridges, Resistance Measurement, and Heat Treatment

Wires soldered to an IDEA chip were connected to the function generator (Stanford Research Systems, Sunnyvale, CA, USA) to apply a constant 5V peak-to-peak (Vpp) voltage at various frequencies (see Figure 25). A polymer cage cut out of double-sided stick tape (3M, St. Paul, MN, USA) was used to contain the suspension of CNTs atop of the IDEAs. The CNT suspension was deposited in a series of 10 μL drops. A microscope glass slide (Thermo Fisher Scientific, Fisherbrand, Waltham, MA, USA) was placed atop of the IDEA chip/polymer cage assembly to decrease the evaporation rate of the solution. The resistance between the fingers was measured with a 3320 Innova multimeter (Innova, Irvine, CA, USA). In order to facilitate solvent evaporation after deposition, the IDEA chips were placed on a hot plate (Fisher Scientific, Hampton, NH, USA) at 200 °C for 20 min. The resistance of the CNT bridges was measured again after the heat treatment. This was done to understand the extent to which the evaporation of the residual solution induces closer contact between the nanotubes.

4.2.5: Polypyrrole (PPy) Deposition

The perpetual capture of CNT bridges was achieved by micropipetting 10 μL of pyrrole/NaDBS solution (see above) over the finger regions of the IDEAs where the CNT

bridges formed, and by applying a DC voltage of 0.9 V for about 90 s (deposition was stopped when PPy reached across the CNT bridge). After PPy deposition, the resistance was measured, and the IDEA chips were placed on the hot plate at 200 °C for 20 min followed by another resistance measurement. An optical microscope (Nikon Eclipse, Minato, Japan) and video editing program (SPOT Basic) were utilized to observe and record resulting CNT bridges on IDEA chips. Scanning Electron Microscope (SEM) images were recorded under low current setting using Magellan 400 XHR SEM (FEI, Hillsboro, OR, USA).

4.26: Finite Element Analysis Multiphysics Simulation

The finite element analysis simulation was carried out with Comsol Multiphysics package (version 5.2) (Comsol, Burlington, MA, USA). 2-D CAD models of the electrode were constructed as presented in Figure 26. The electrode was modelled to be 2.5 μm thick, with the space above the electrodes and top of the water being 75 μm, and the CNTs as being attached to the edge of the electrode.

The meshing condition was set up to be a physical-controlled mesh with a defined element size set to "extremely fine" and refined near the electrode surface to yield about 18,000 triangular mesh elements. The model was solved by a built-in linear solver. Boundary conditions were set up to be 0 V for the surfaces of three connected electrodes and 4 V for the other three connected electrode fingers. The material of the electrodes was selected to be glassy carbon. In order to simply the model, the permittivity was defined to be $1E8 \cdot \varepsilon_0$, while the liquid medium was isopropyl alcohol with conductivity of $6 \cdot 10^6$ pS/m and relative permittivity of $18.23 \cdot \varepsilon_0$

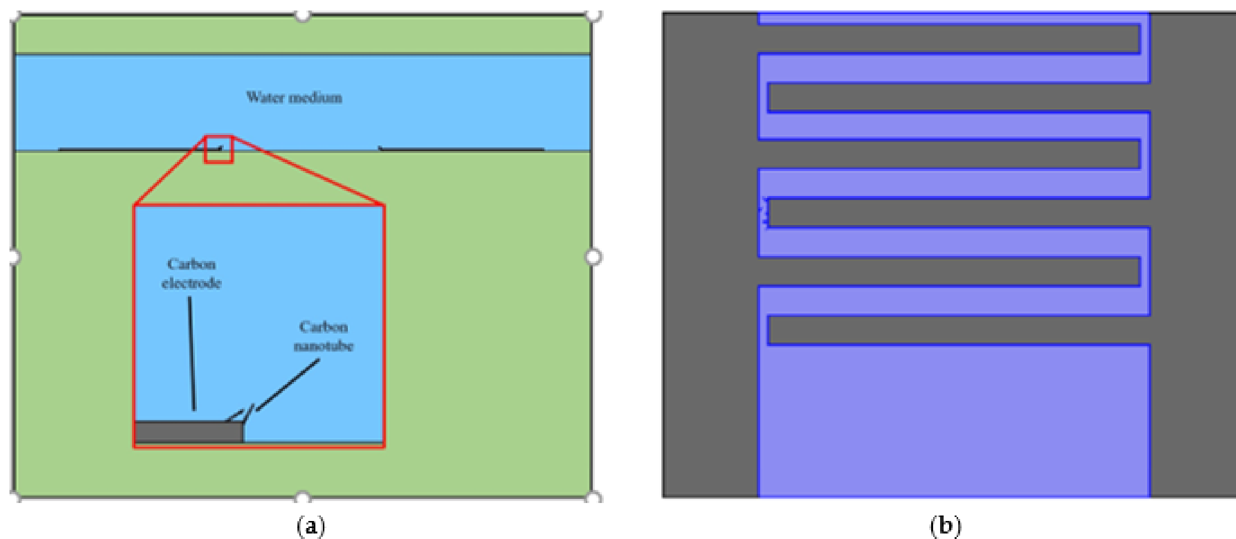

Figure 26: CAD drawings of the interdigitated electrode arrays (IDEA) used in Comsol simulation: side view (**a**) and top view (**b**)[117].

4.3: Results and Discussion

4.3.1: Continuous vs. Step-wise CNT Bridge Formation

The mechanism leading to the formation of the CNT bridges has been explored. First, a one-step procedure of continuous deposition was tested: when one 30 µL drop of CNT suspension was placed onto the IDEA chip with a 5 Vpp bias and applied frequency of 100 kHz, only short segments of CNT chains formed after several minutes, as seen in Figure 27b. The likely reason for the inability of this single-step continuous deposition process to form a long CNT bridge is the fact that the resulting CNT line that forms via DEP alignment lacks sufficient nanotube-to-nanotube contact. Thus, as the CNT chain is being built, the CNT line becomes more and more resistive until the electric field strength ceases to be sufficient enough for further attraction and alignment of the CNTs.

We are proposing an alternative to continuous CNT deposition—a step-wise deposition where first one droplet of CNT suspension is deposited over the electrodes to enable CNT segments to begin forming under the influence of DEP forces. We then dry the solution from CNT suspension, or simply wait until the droplet of solvent evaporates (it usually takes just a few minutes as the CNT suspension is not covered by the glass slide). As solvent evaporates, surface tension of shrinking droplets surrounding the deposited CNTs will pull CNTs together, enabling better contact, and consequently forming a CNT spike that results in an area of high field as demonstrated by the results of the Comsol simulation shown in Figure 28.

A step-wise deposition of CNT bridges was successfully performed under a wide range of frequencies. Figure 27a presents the results of CNT bridge formation after the deposition and drying of three 10 μL drops of CNT suspension (in contrast to a single 30 μL CNT suspension drop used in a single step continuous deposition trial). The applied voltage and frequency of 5 Vpp and 100 kHz were also used as in the single-step continuous deposition trial. It can be seen in the sequence of optical micrographs in Figure 27a how the CNT bridge forms gradually after deposition of each CNT droplet, until a continuous conductive CNT bridge is formed that spans the entire 50 μm inter-electrode spacing.

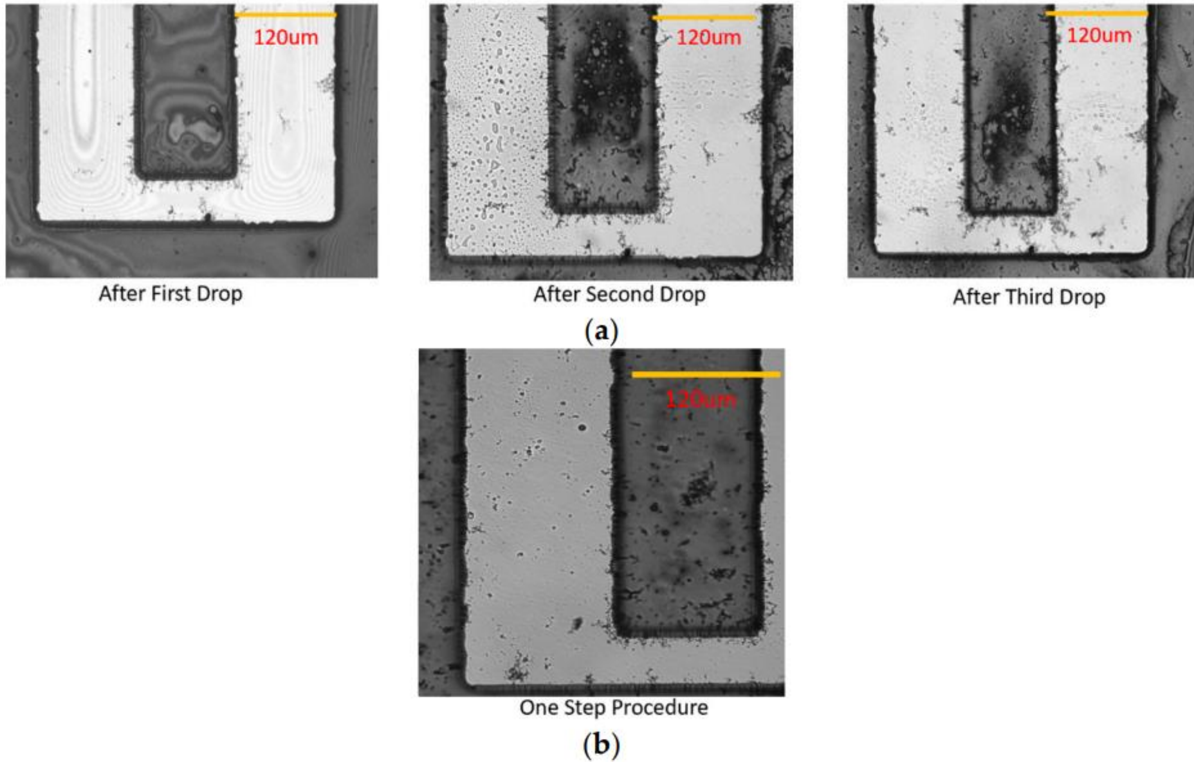

Figure 27: Comparison between the CNT bridges formed by step-wise procedure (**a**) and the CNT bundles attracted by the one-step procedure (**b**). Both deposition procedures used an AC 5 Vpp bias at 100 kHz[117].

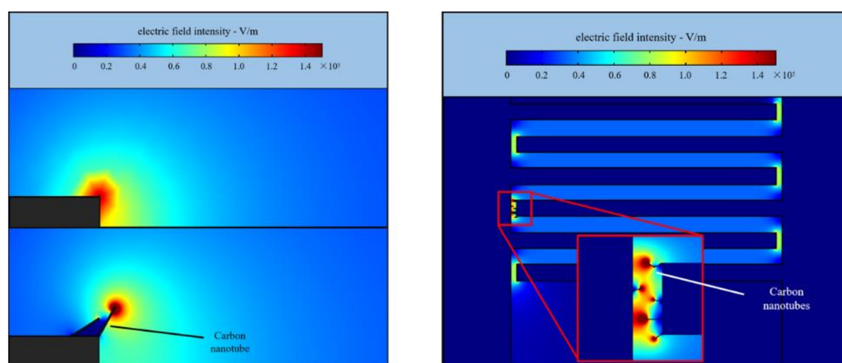

Figure 28: Comsol simulation of electric field intensity around the end of CNTs in the step-wise CNT bridge formation process. (**a**) Field distribution near an individual CNT bundle (**b**) Results of the simulation show that during bridge formation, regions of highest field intensity shift from the edges of electrodes to the ends of the CNT bridges[117].

4.3.2: Applied Frequency Influence on the Morphology of CNT Bridges

The formation of the bridges was demonstrated under the AC bias of 5 Vpp at frequencies of 1 kHz, 10 kHz, 100 kHz, 1 MHz, and 10 MHz (see optical micrographs on Figure 29 and Scanning Electron Microscopy (SEM) images in Figure 30). The morphologies of the CNT bridges depended on the applied frequencies. At relatively low frequencies, such as 10 kHz and 1 kHz, electro-osmotic (EO) forces [74][73][83] generate fluidic circulation near the edges of the fingers of the IDEAs where the electric field intensity is strongest. In the presence of these electro-osmotic forces, the alignment of the CNTs is disturbed. Outside the frequency range of EO flow, and within frequencies ranging from 100 kHz to 10MHz, the positive DEP attraction of CNTs to the edges of the fingers of the electrodes dominates vanishingly small EO forces. Since the magnitude of the electro-osmotic force increases with decreasing frequency [83], larger amounts of CNTs needed to be deposited at the bridge sites for the bridges to form. This relationship between EO and DEP forces at various frequencies helps to explain the observed morphologies of the CNT bridges.

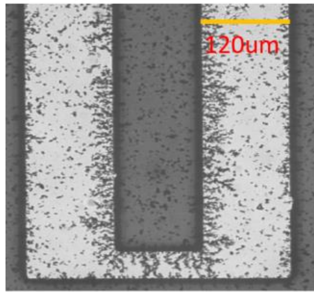

10MHz 5V peak to peak

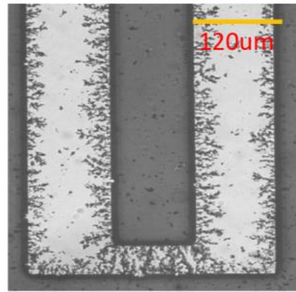

1MHz 5V peak to peak

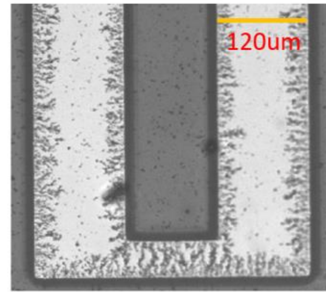

100kHz 5V peak to peak

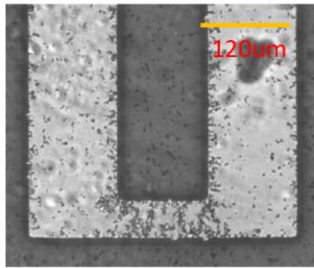

10kHz 5V peak to peak

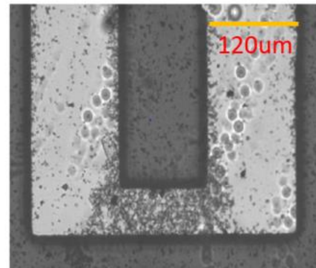

1kHz 5V peak to peak

Figure 29: CNT bridges deposited under 5 Vpp AC bias at 1 kHz, 10 kHz, 100 kHz, 1 MHz, and 10 MHz applied frequencies[117].

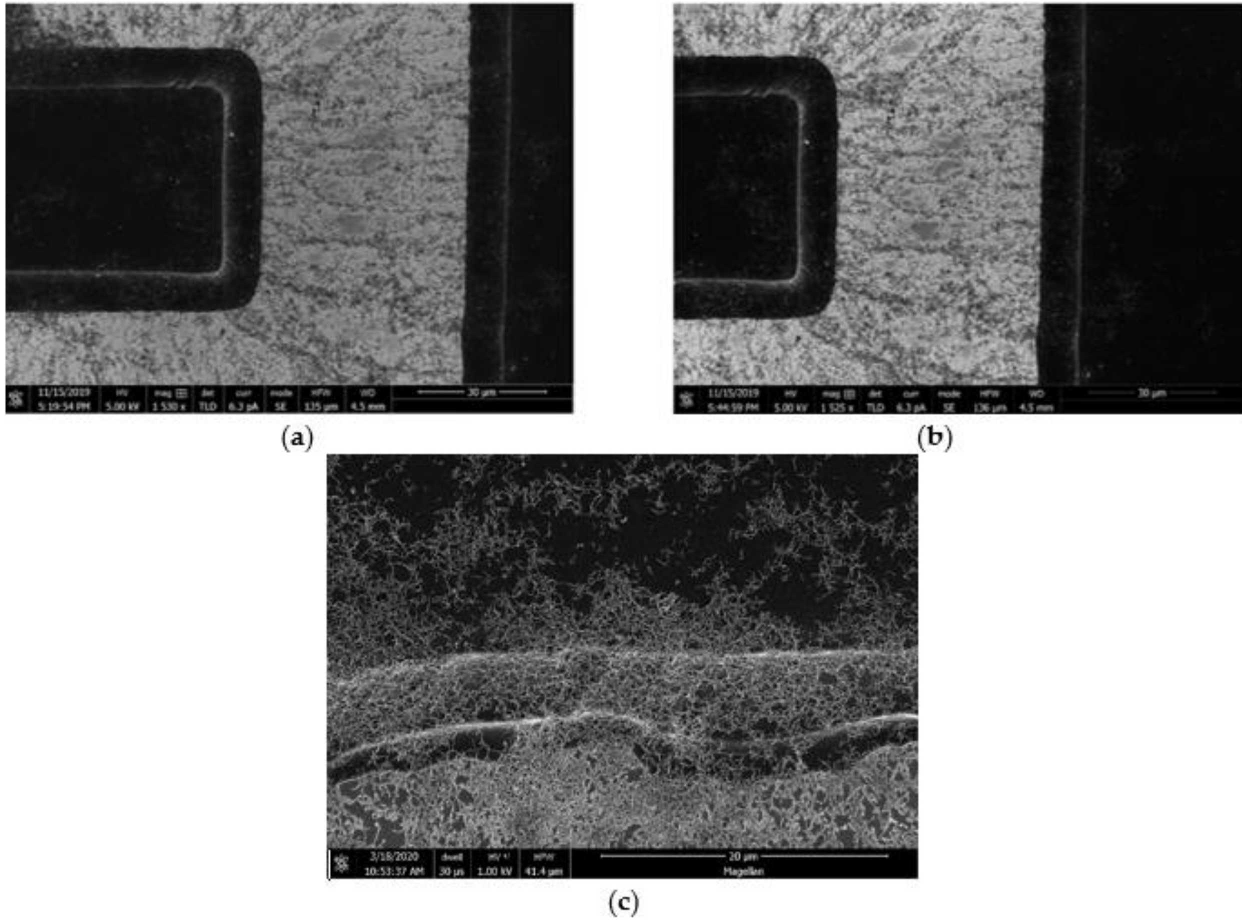

Figure 30: The SEM images of CNT bridges deposited under 100 kHz frequency. (**a**, **b**) SEM images of electrodes at 1530 and 1525 magnification, respectively; (**c**) SEM image of the edge of electrode at 5000 magnification[117].

4.3.3: Influence of Postdeposition Heat Treatment on Resistance of CNT Bridges

Dependence of postdeposition heat treatment on the resistance of fabricated CNT bridges has been explored on two samples (identified as Samples 1 and 2 in Table 2 and in the resistance measurement plots in Figure 32). First, initial resistance of the IDEA array was measured. As expected, prior to CNT bridge deposition, the resistance was infinite. After the CNT bridges formed, the IDEA chip was blow dried with a nitrogen gun for about a minute until the chip was visibly dry, then the resistance of the IDEA was measured by placing the probes of the multimeter on the contact pads of the IDEA chip. That measurement is termed R1. The IDEA chip was then placed on a hot plate at 200 °C for 20 min; afterward, the resistance was measured again (R2). In order to permanently secure CNT bridges in place, a layer of polypyrrole was electrodeposited as discussed in the Materials and Methods section above and on subsection 3.4 below. After PPy deposition over CNT bridges, the chip was blow dried and the resistance was measured again (R3) and once again (R4) after another heat treatment. The flowchart of these steps is presented in Figure 31. Table 2 contains the resistance measurements for CNT bridges deposited under the variety of applied frequencies, while Figure 32 represents a graph of these measurements for clear identification of the trends.

It is clear that as a result of the heat treatment (200 °C for 20 min), the resistance of the CNT bridges decreases dramatically. For example, for CNT bridges deposited under 5 Vpp at an AC frequency of 1 MHz, the resistance is reduced six-fold from around 12 kΩ prior to heat treatment to roughly 2 kΩ after the heat treatment. Our hypothesis is that this decrease in

the resistance can be attributed to the evaporation of any residual CNT solution existing between the individual CNTs. These pockets of liquid remaining after blow drying steps start to further shrink and evaporate under the heat treatment. As the liquid surrounding the CNTs evaporates, the surface tension of these shrinking droplets pulls CNTs together as depicted in Figure 33, leading to a dramatic increase in conductivity of CNT bridges. This formation of microaggregates due to surface tension during solvent evaporation was observed by other researchers [118].

Table 2: Resistivities of samples 1 and 2 showing mean values and standard deviation after CNT deposition (CNT), drying on hot plate for 20 min at 200 °C (CNT + HT), polypyrrole deposition (CNT + HT + PPy), and final drying on hot plate for 20 min at 200 °C (CNT + HT + PPy + HT)[117].

	CNT (kΩ)	**CNT + HT (kΩ)**	**CNT + HT + PPy (kΩ)**	**CNT + HT + PPy + HT (kΩ)**
Sample 1				
10 MHz	5.86 ± 0.09	1.03 ± 0.11	2.82 ± 0.02	1.98 ± 0.01
1 MHz	12.43 ± 0.1	2.04 ± 0.01	3.11 ± 0.04	2.17 ± 0.10
100 kHz	9.75 ± 0.12	1.05 ± 0.01	2.88 ± 0.04	2.05 ± 0.02
10 kHz	12.83 ± 0.08	1.41 ± 0.02	7.01 ± 0.21	3.31 ± 0.05
1 kHz	31.27 ± 0.15	3.34 ± 0.33	9.54 ± 0.20	6.74 ± 0.25
Sample 2				
10 MHz	6.26 ± 0.05	1.08 ± 0.01	2.01 ± 0.17	1.31 ± 0.02
1 MHz	12.04 ± 0.08	1.76 ± 0.02	4.61 ± 0.10	4.17 ± 0.03
100 kHz	10.39 ± 0.18	1.07 ± 0.01	2.83 ± 0.51	1.76 ± 0.02
10 kHz	10.31 ± 0.23	1.82 ± 0.02	6.65 ± 0.40	4.04 ± 0.06
1 kHz	13 ± 0.07	1.88 ± 0.01	2.57 ± 0.19	2.13 ± 0.06

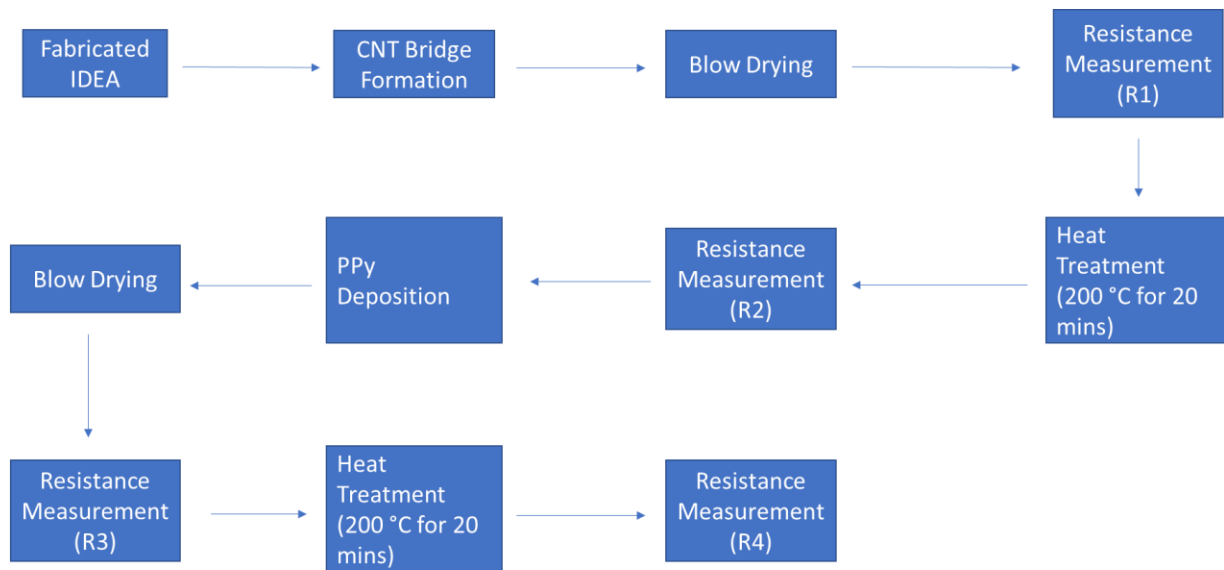

Figure 31: The flow chart of the experimental procedure[117].

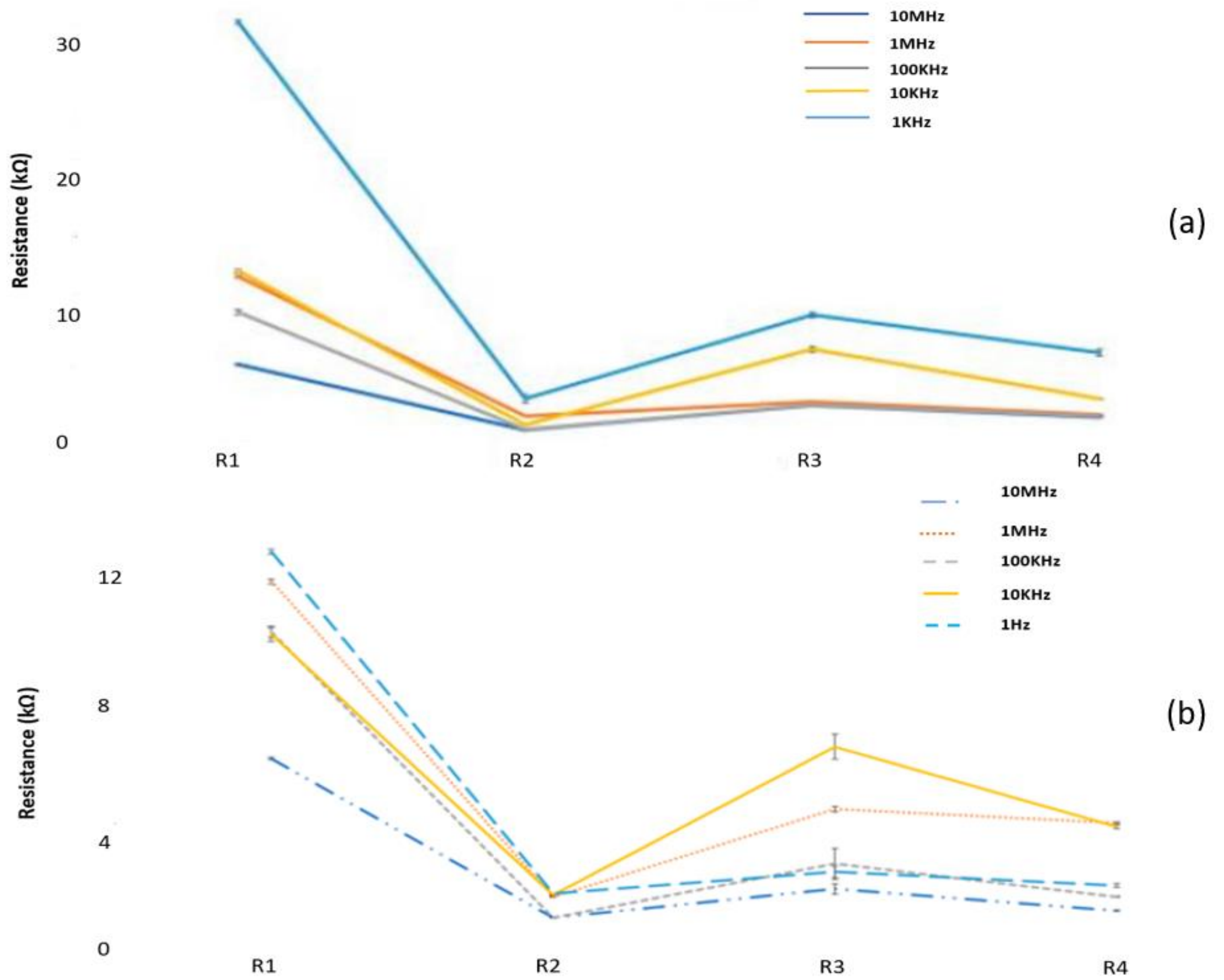

Figure 32: The resistance of CNT bridges of sample 1 (**a**) and sample 2 (**b**) as function of deposition parameter and postdeposition heat treatment including after CNT deposition (R1), drying on hot plate for 20 min at 200 °C (R2), after polypyrrole deposition (R3), and after final drying on hot plate for 20 min at 200 °C (R4)35[117].

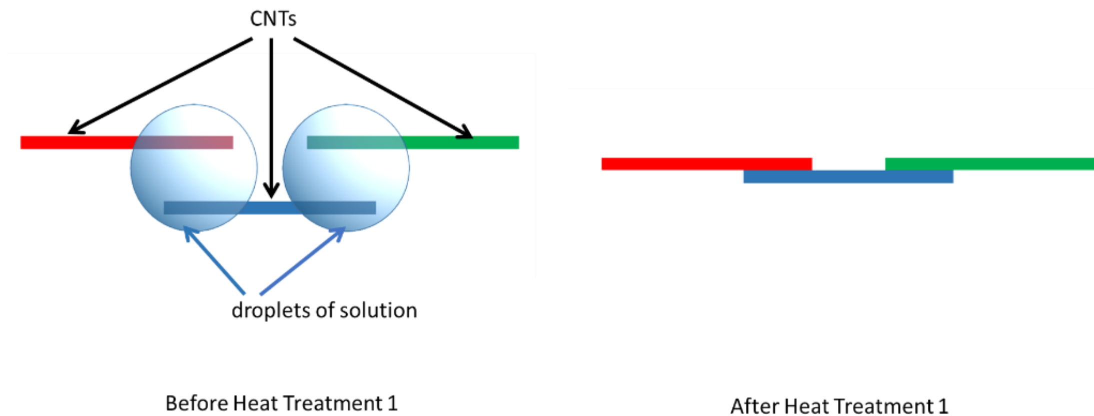

Figure 33: The illustration of the influence of postdeposition heat treatment on CNT bridges. (**a**) Remaining droplets present after blow drying keep CNTs separated; (**b**) Evaporation of remaining solvent after heat treatment and the resulting changes in surface tension act to pull CNTs together, improving CNT-CNT contact[117].

4.3.4: PPy Deposition over CNT Bridges

After CNT bridges were deposited under the influence of electrokinetic forces as discussed in previous sections, pyrrole solution was dispensed over the IDEA and electropolymerization was performed to permanently entrap and fix the fabricated CNT bridges [119]. The PPy was initially electropolymerized at the surface of the electrode fingers and subsequently grew along the CNT bridges until a PPy layer completely covered the CNT bridge, as shown in Figure 37. The resistances were measured after the PPy deposition (R3) and after the 20 min heat treatment at 200 °C (R4). These electrical resistance measurements are listed in Table 2

and graphed on the plot in Figure 8. The increase in the resistance (R3 > R2) after the PPy deposition can be attributed to the introduction of PPy solution that tends to separate CNTs within the bridge. The heat treatment after PPy deposition was not as effective as before (R4

> R2) because there was a polymer film covering CNT bridges that slowed down solvent evaporation, as illustrated in Figure 34.

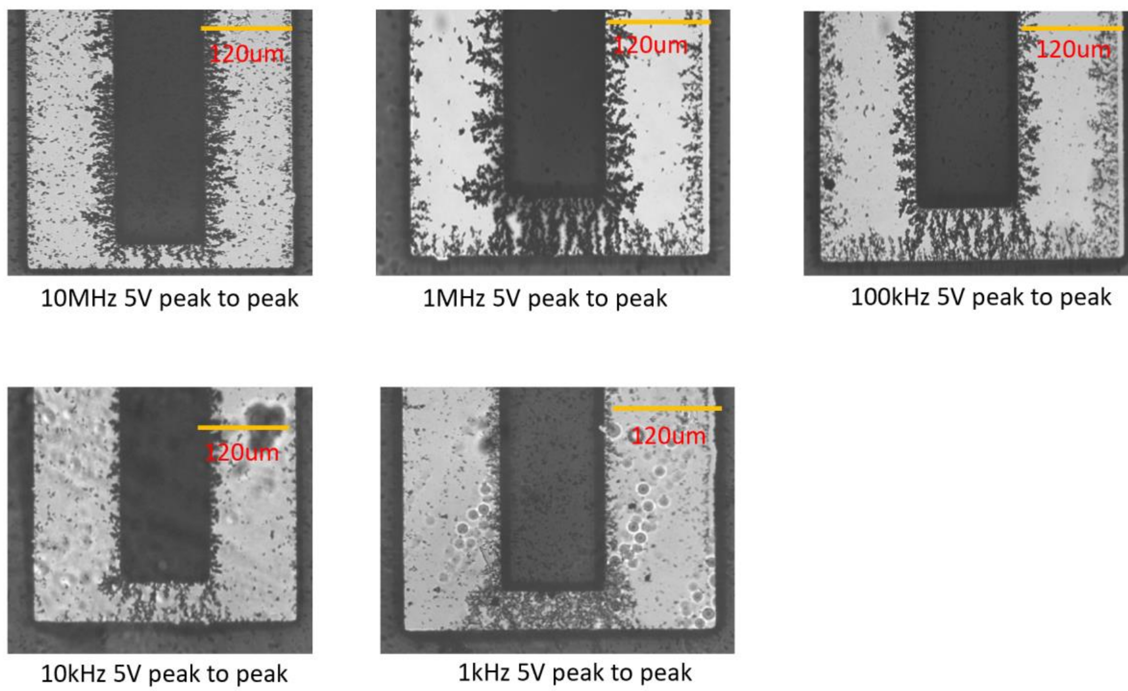

Figure 34: The CNT bridges after electrodeposition of PPy[117].

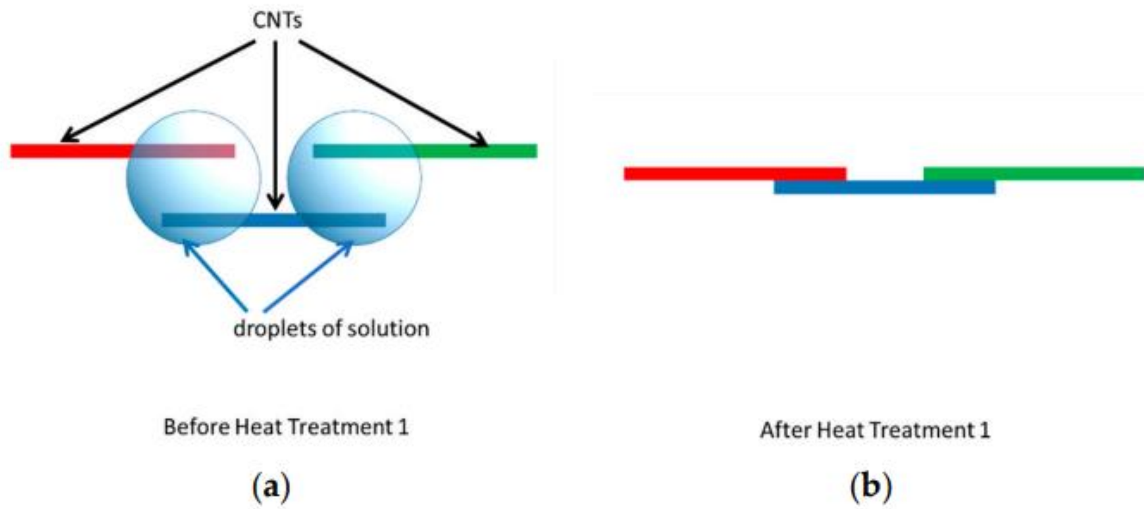

Figure 35: The illustration of the influence of heat treatment on CNT bridges after PPy deposition. (**a**) PPy deposition envelops CNT bridges with remaining solvent after blow drying (**b**) Less dramatic changes in resistance were observed before and after the final heat treatment. This is attributed to the PPy layer which prevents complete evaporation of solvent[117].

Chapter 5

Guided Healing of Damaged Microelectrodes via Electrokinetic Assembly of Conductive Carbon Nanotube Bridges

5.1: Introduction

The approach to guided repair of microelectrodes presented in this study focuses on the use of carbon nanotubes (CNTs) known for their impressive electrical and mechanical properties [8]. Our research focuses on electrokinetic assembly that employs electrical forces to manipulate small particles to create micro and nanoscale structures. Specifically, dielectrophoretic (DEP) force is utilized to manipulate and arrange the CNTs. In addition to the use of DEP force for electrokinetic assembly. this research utilizes the step-wise CNT deposition process previously reported[117]. This method involves iterative deposition of small droplets of CNTs suspended in isopropyl alcohol (IPA) and allowing the IPA to evaporate between depositions. It was hypothesized that during the evaporation step, capillary forces of the contracting liquid meniscus bring neighboring chains of CNTs into tighter contact, thus reducing the CNT-to-CNT contact resistance. This novel process is critical in enabling the construction of conductive CNT bridges across much wider electrode gaps than previously reported. The step-wise CNT deposition was successfully used to create a conductive CNT bridge over 75 micron long. However, the electrode geometry utilized in that study (a straight microelectrode surrounded by a horseshoe-shaped electrode) produced a non-uniform field conducive to strong DEP forces and the question remained

about the applicability of this approach to the conventional straight electrodes with gap in between or to the creation of the conductive CNT bridge to repair the broken electrodes. Present research conclusively demonstrates the validity and feasibility of the step-wise DEP deposition of conductive CNT bridges to heal the broken conventional microelectrodes.

The combination of DEP electrokinetic assembly paired with step-wise deposition of CNTs demonstrated in this research creates a process which is self-reinforcing, i.e., as the process progresses, the magnitude of the DEP force increases (as illustrated by the COMSOL simulation below). Additionally, the effective resistance of the contact junctions between successive CNT chains is evaluated for CNT bridges of various lengths.

Fabrication of long conductive CNT bridges, besides their application in micro- and nano-electronics will find widespread application in many other fields, including biotechnology and tissue engineering.

5.2: Materials and Methods

5.2.1: Fabrication of Carbon Electrodes

Various sets of carbon microelectrodes with electrode gaps of 20, 30, and 40 microns were produced by initially photopatterning SU-8 resist via a standard lithographic process and then pyrolyzing a SU-8 precursor in a reductive nitrogen environment of the furnace that converts organic resist into glassy carbon material. Figure 36b presents the geometry of the microelectrodes: the width of the electrode fingers is 120 μm, while the length of the opposing electrode segments are 5 mm each. These microelectrodes terminate in a square

contact pad with the sides of 2 mm wide. Additionally, a set of electrodes was produced that did not have any gaps and after these "undamaged" electrodes were produced, we scratched these electrodes, creating a realistic break that was wider than 170 microns. The details of the fabrication process of the carbon electrodes are given below.

A 4" silicon wafer covered with a 1 µm oxide layer (University Wafer, Boston, MA, USA) was spin-coated with SU-8 2015 photoresist (Kayaku Inc., Westborough, MA, USA) using a Laurell photoresist spinner (Laurell Technologies, North Wales, PA, USA) at an initial speed of 500 rpm for 10 s, followed by 4000 rpm spin for 30 s. A hot plate was used for soft-baking at 95 °C for 2 min. The subsequent exposure step was performed using a photomask (CadArt, Bandon, OR, USA) and ultraviolet (UV) light at an energy intensity of 10 mW/cm2 for 10 s in a Karl Suss MA56 Mask Aligner (Karl Suss, Garching, Germany). The wafer was then post-baked on the same hot plate at 95 °C for 4 min. The undeveloped resist was removed with SU-8 developer (Kayaku Inc., Westborough, MA, USA). The remaining developed resist layer underwent hot-baking at 150 °C for 20 min. After hot-baking, the resist layer was carbonized inside a pyrolysis furnace (Thermo Fisher Scientific, Waltham, MA, USA), within a nitrogen-rich environment. The pyrolysis process was initiated at 25 °C for two hours, followed by a 69 min ramp to 300 °C, where the temperature was maintained for one hour before a subsequent 90 min ramp to 900 °C, where the temperature was maintained again for one hour before being allowed to naturally cool to room temperature overnight. Finally, 34-gauge buss wire (Guasti Wire and Cable, Ontario, Canada) was soldered onto the contact pads of the electrode using Indium solder.

5.2.2: Preparation of Carbon Nanotube Suspension

The CNT suspension was prepared by adding 0.005 g of multi-wall CNT (MWCNT) powder (Sigma-Aldrich, St. Louis, MO, USA) into 15-mL of isopropyl alcohol (IPA). The solution underwent centrifugation in an Eppendorf 5702 Centrifuge (Eppendorf AG, Hamburg, Germany) at 3000 rpm for 4 h. The large agglomerates of CNTs had precipitated and the supernatant containing low concentration of suspended CNTs was pipetted out.

5.2.3: Experimental Setup and Deposition of Carbon Nanotube Suspension

The chip containing the carbon electrode array was placed under an optical microscope (Nixon Eclipse, Minato, Japan) which was connected to a video camera (SPOT Imaging, Sterling Heights, MI, USA). The buss wires soldered onto the carbon electrode were connected to a function generator (Stanford Research Systems, Sunnyvale, CA, USA) which was set up to apply AC bias at a frequency of 100 kHz and the constant peak-to-peak voltage (Vpp) of 4 V. The experimental setup is depicted in the diagram in Figure 36a.

A 0.5 μL of the CNT suspension was pipetted (Labnet, Edison, NJ, USA) on top of the electrode gap. The droplet of CNT suspension was allowed to fully evaporate, which could be visually confirmed under the optical microscope. Once fully evaporated, the next droplet of CNT suspension was deposited. This step-wise deposition continued until the CNT bridge could be seen spanning the entirety of the gap. Once the conductive CNT bridge was completed, the wires were disconnected from the function generator and a resistance measurement across

the electrode was taken using a multimeter (Wavetek, San Diego, CA, USA). In order to assess the efficacy of the healing process, resistance across a reference electrode containing no gap was also measured. Finally, high magnification images of the CNT bridges were taken using a Magellan 400 XHR scanning electron microscope (FEI, Hillsboro, OR, USA).

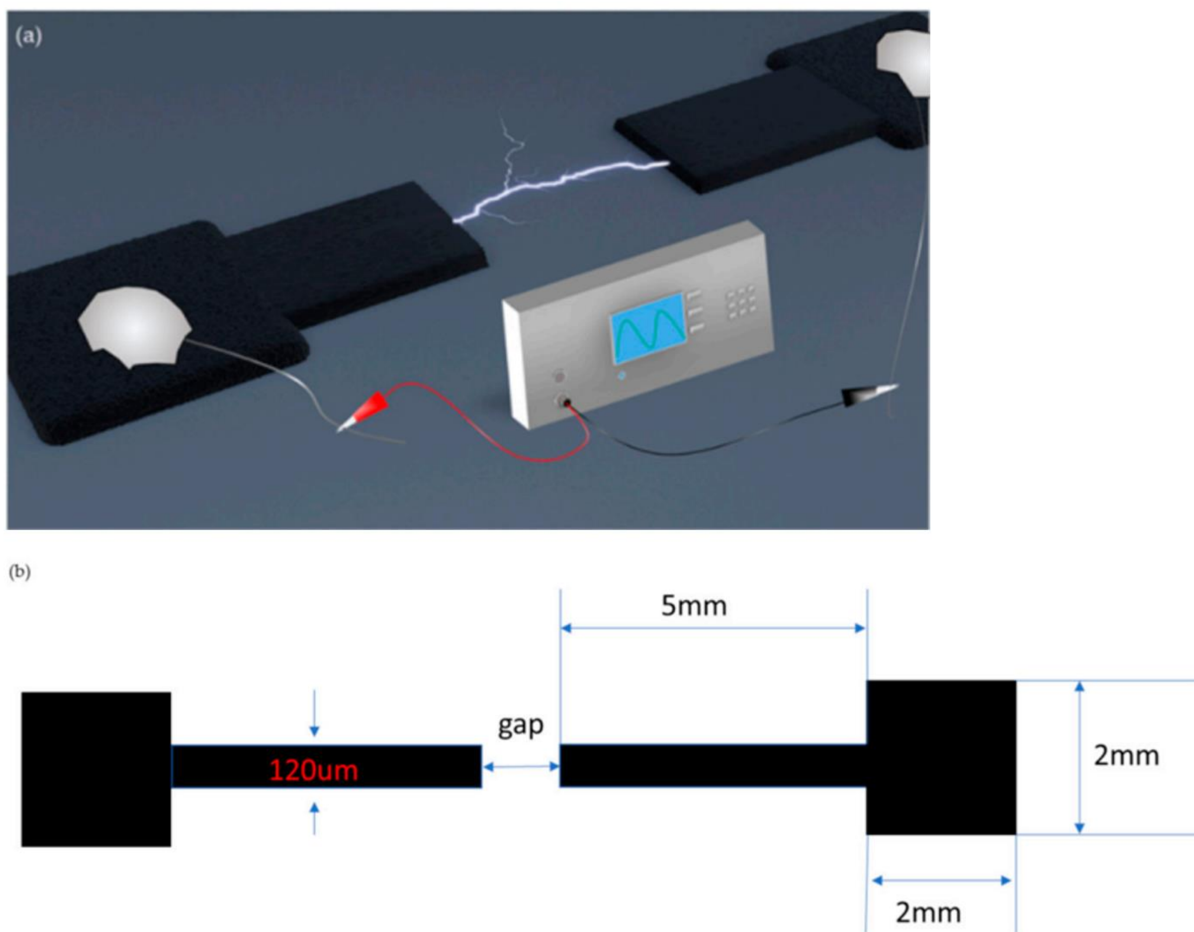

Figure 36: (**a**) Carbon nanotube (CNT) electrokinetic assembly experimental setup design. (**b**) Dimensions of the carbon electrodes[120].

5.2.4:Preperation of Pyrrole Solution

A 0.1M pyrrole monomers (Sigma-Aldrich, St. Louis, MO, USA) and 0.1 M NaDBS (sodium dodecylbenzenesulfonate) (Sigma-Aldrich, St. Louis, MO, USA) were mixed with 100 mL of deionized water and stirred for 20 min at room temperature.

5.2.5: Polypyrrole Deposition

In order to permanently affix the CNT bridge to the electrodes and the substrate, the layer of electroactive polymer polypyrrole (PPy) was electrodeposited atop of the CNT bridge. The pyrrole solution was pipetted (Labnet, Edison, NJ, USA) over the deposited CNT bridge while a 0.9V direct current (DC) bias was applied by the function generator (Stanford Research Systems, Sunnyvale, CA, USA). Two different methods were evaluated for the deposition of PPy. In one approach, the DC bias was applied between the working electrode (one of the microelectrodes) and the counter-electrode (the microelectrode across the gap) and the deposition proceeded from one microelectrode and across the CNT bridge until the PPy layer reached the other microelectrode on the other side of the gap. In the alternative deposition technique, the initial deposition started as previously described, but once the PPy layer reached the approximate position of half-way through the CNT bridge, the electrodes for DC bias were switched and the PPy deposition will start from the opposite side of the bridge and the deposition will be finished when the PPy layers will merge. The differences between these two PPy deposition methods are evaluated in Section below.

5.2.6: Stress-Testing of Carbon Nanotube (CNT) Bridges

Once fabricated, samples with the CNT bridges across 30 μm gaps, with and without PPy coat, were tested to determine how resilient they were to several types of environmental stress, including the forceful blasts of compressed nitrogen gas, placing the samples under the running water stream, and exposing the sample to thermal cycling.

Each sample was subjected to 10 rounds of thermal cycling during which they were brought to 200 °C using a hot plate and then cooled to 3 °C using an ice pack. There was no resident time at the top or bottom temperature—once the temperature was reached, the sample was immediately moved to the other temperature extreme. Next, each sample were placed under a stream DI water running with a volumetric flow rate of 0.06 L per minute (LPM) for a total of 30 s. Finally, each sample was blown with nitrogen gas at 88 pounds of force per square inch (psi) for 30 s. After each test, the resistance of the electrode was measured.

5.2.7:Finite Element Analysis of Electric Field Magnitude

A simulation was conducted in the Comsol Multiphysics Software package (v. 5.2) (Comsol, Burlington, MA, USA) to analyze the strength of the electric field strength resulting from applied AC bias across electrode gaps of various lengths. The square of the electric field strength was also analyzed. The fine geometry-controlled triangular mesh containing more than 18,000 elements was implemented. The model used a glassy carbon electrode material and the surrounding IPA medium with permittivities of 108 $\cdot\varepsilon_0$ and 18.23$\cdot\varepsilon_0$, respectively. A

built-in linear solver was utilized to calculate the solution of the governing (Laplace) system of equations. The boundary conditions were set to be 0 for one electrode and 4V for another electrode.

5.3: Results

5.3.1:CNT Bridges across 20, 30 and 40 µm Electrode Gaps

5.3.1.1:Assembly of CNT Bridges

Using the procedure outlined in Section 2.3 above, CNT bridges were successfully assembled across the 20, 30, and 40 µm electrode gaps. Three samples were manufactured and tested for each type of electrode. Images were taken throughout the CNT deposition process using the optical microscope equipped with the cMOS camera and are presented in Figure 37, 38, and 39.

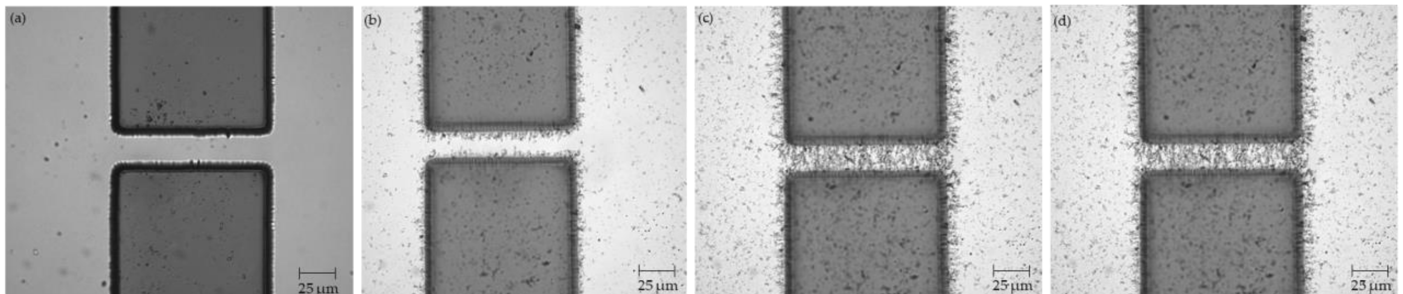

Figure 37: Electrodes with 20 µm gap (**a**) before CNT deposition; (**b**) after 2 µL of CNT suspension; (**c**) after 4 µL of CNT suspension; (d) after 5 µL of CNT suspension[120].

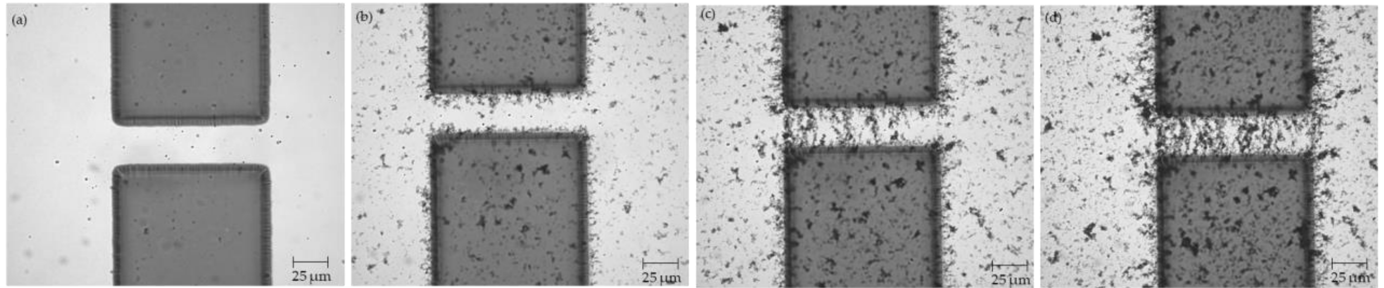

Figure 38: Electrodes with 30 μm gap (**a**) before CNT deposition; (**b**) after 3 μL of CNT suspension; (**c**) after 7 μL of CNT suspension; (**d**) after 10 μL of CNT suspension[120].

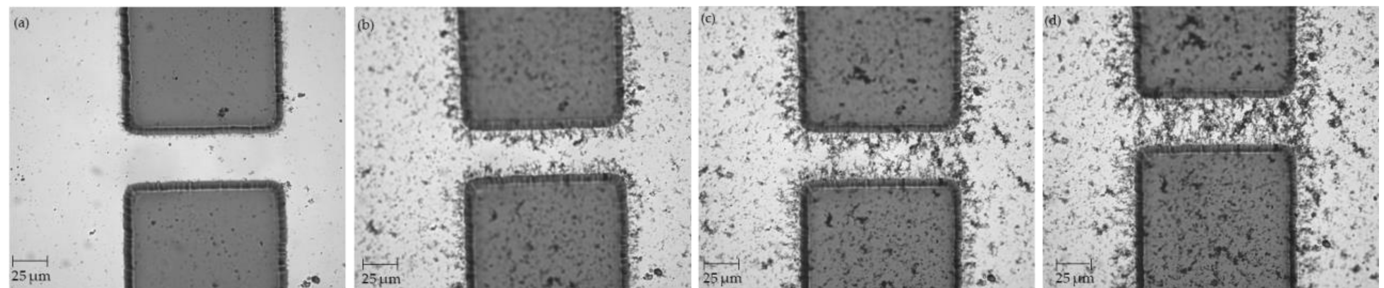

Figure 39: Electrodes with 40 μm gap (**a**) before CNT deposition; (**b**) after 5 μL of CNT suspension; (**c**) after 7 μL of CNT suspension; (**d**) after 10 μL of CNT suspension[120].

Table 3 below summarizes the resistance across the electrode with 30 μm gap after every deposition of every two 0.5 μL drops of CNT suspension.

As expected, the amount of CNT suspension required to form a complete conductive bridge increased as the electrode gaps become wider. The resistance across the electrode decreased exponentially with the increased number of the deposited CNT suspension droplets. Scanning Electron Microscopy (SEM) images in Figure 40 illustrate the morphology of the CNT bridges.

Table 3: Resistance measured across the electrode with 30 μm gap after deposition and drying of every two 0.5 μL droplets of CNT suspension[120].

Total Amount of CNT Suspension (μL)	Resistance (kΩ)	Total Amount of CNT Suspension (μL)	Resistance (kΩ)
1	open circuit	6	open circuit
2	open circuit	7	open circuit
3	open circuit	8	360
4	open circuit	9	147
5	open circuit	10	28.7

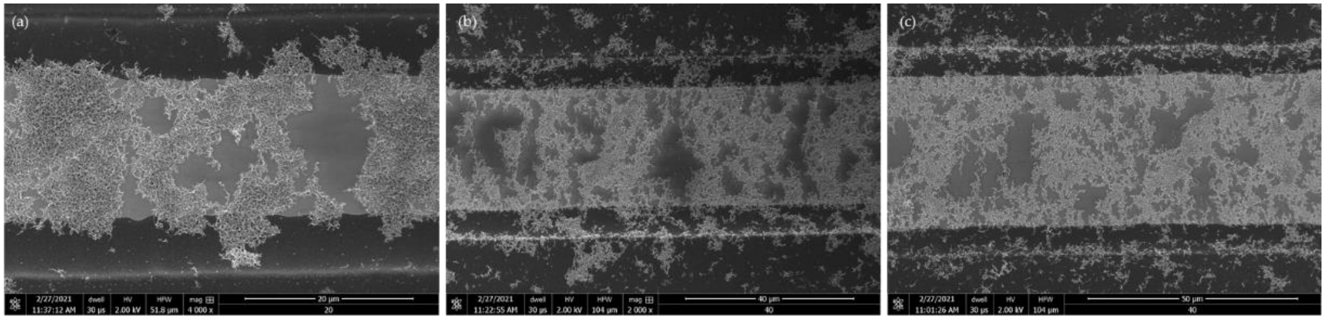

Figure 40: Scanning electron microscope (SEM) pictures of the CNT bridges formed across (a) 20 μm electrode gap (b) 30 μm electrode gap (c) 40 μm electrode gap[120].

5.3.1.2: Resistance of CNT Bridges

Resistance measurements taken across the healed electrodes are summarized in Table 5 below. Additionally, these resistance measurements are plotted as a function of CNT bridge length in Figure 41.

Table 4: Resistance of microelectrode before and after fracture and resistances of healed 20, 30, and 40 μm gap electrodes[120].

Electrode Gap Length (μm)	**Avg. Resistance Measurement (Std. Dev.) (kΩ)**
Microelectrode prior to fracture	5.80 (±0.61)
Microelectrode after fracture (>170 μm gap)	Open circuit
20	15.61 (±1.85)
30	19.11 (±1.88)
40	31.88 (±6.98)

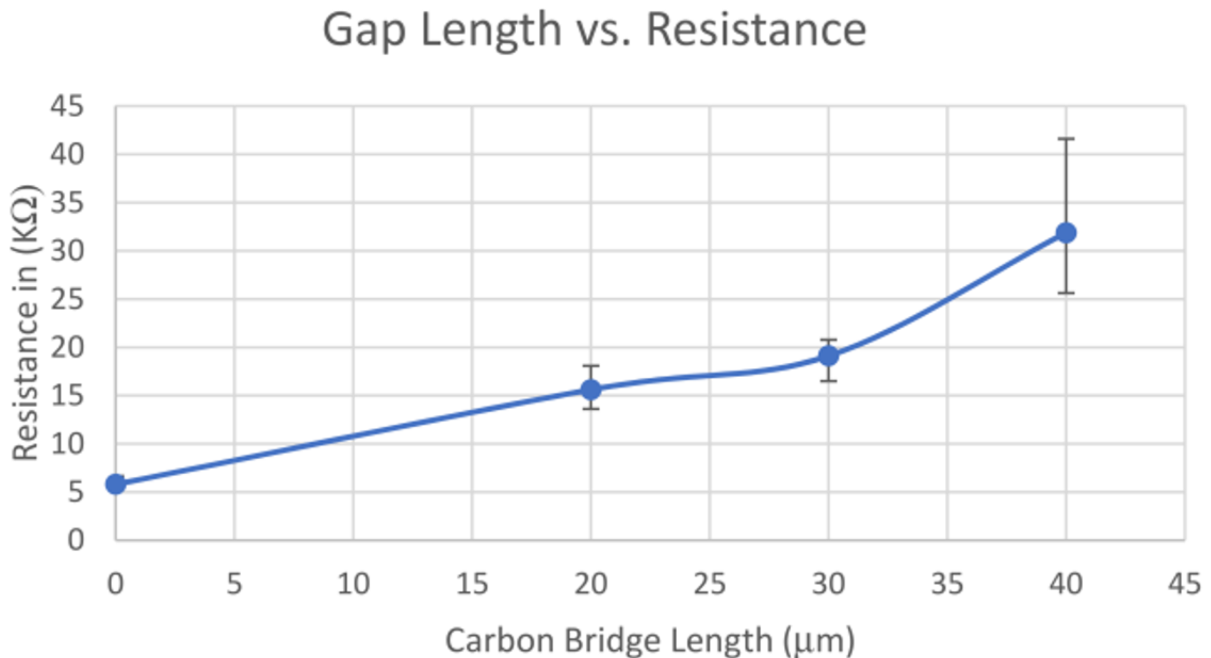

Figure 41: Plot of the measured resistance of the healed electrodes as function of CNT bridge length[120].

The graph in Figure 41 demonstrates that the resistance across the healed electrode increases with CNT bridge length. Previous research has concluded the primary contribution to the resistance across a CNT bridge is the resistance arising at the CNT-to-CNT contact

junctions[121][118]. The results presented here suggest that the contact resistance grows as the length of the CNT bridge increases, since the increase in resistance is non-linear.

Based on the comparison of the resistance of undamaged (reference) electrodes and the healed electrodes (see Table 4) we can conclude that the electrokinetically assembled CNT bridges restored conductivity to the electrodes, but we could see a significant decrease in the repaired electrodes' conductivity. The healed electrodes had resistance that was 169%, 229%, and 449% higher than the original resistance for the 20, 30, and 40 μm gap electrodes, respectively.

5.3.1.3: Electric Field Strength Simulation

A simulation of electric field strength across varying electrode gap lengths was conducted using the multiphysics Comsol framework. As shown in Figure 42 below, the strength of the electric field is inversely proportional to the distance across which it is applied. This is an expected result according to Coulomb's law describing the magnitude of on electric field[122].

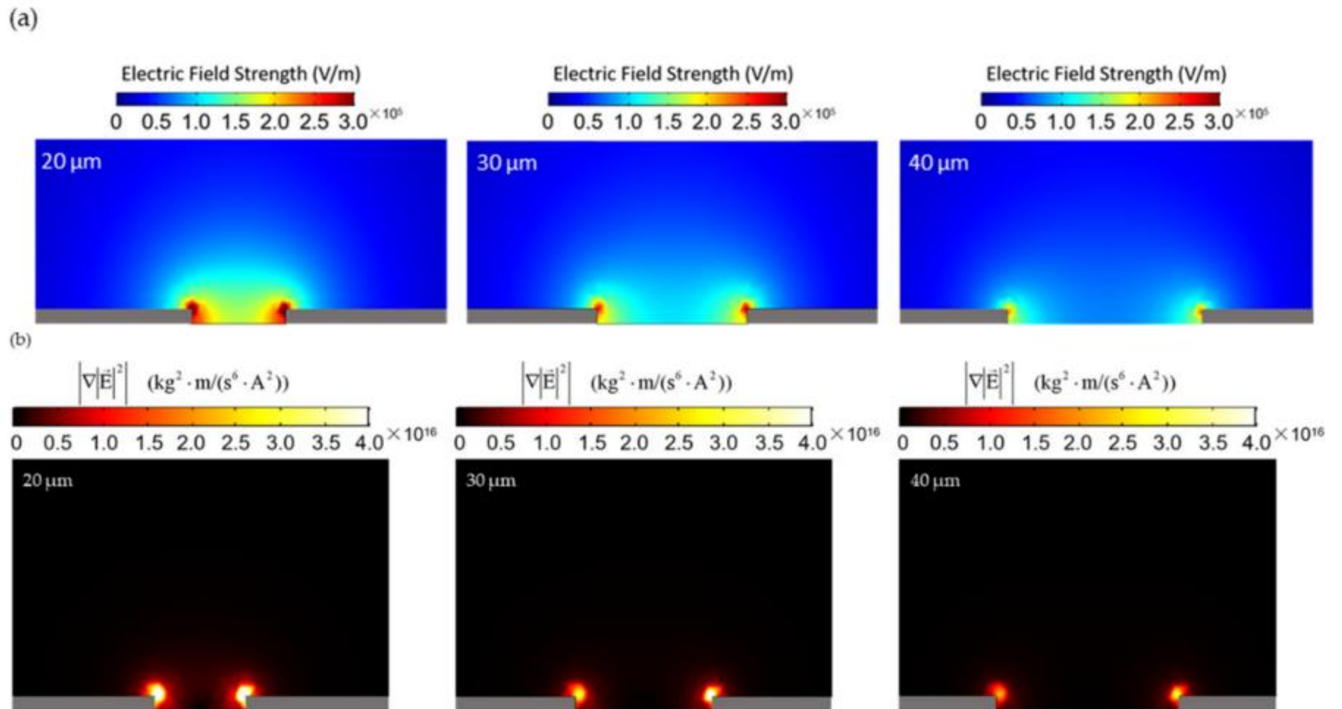

Figure 42: Simulation across electrode gap lengths of (a) the electric field strength (b) the gradient of the square of the electric field strength[120].

This result indicates that as a conductive bridge is assembled and the distance between the opposing ends of the growing bridge spans become smaller, the applied electric field increases with the attendant increase in the DEP force instrumental for the CNT bridge assembly. This self-reinforcing process is important for offset higher contact resistance of the CNT-to-CNT network away from the electrodes.

5.3.1.4: CNT Bridge across the Fractured Electrode

The same process used to assemble the CNT bridge across pre-manufactured electrode gaps was successfully applied to an electrode that was mechanically fractured using a sharp glass tip. The gap resulting from the fracture was expectedly non-uniform. At its smallest, the gap

was over 170 μm wide and the largest gap was over 310 μm wide. Once broken, it was confirmed using a multimeter that the electrode had infinite resistance. After application of 23 μL of CNT suspension (in increments of 0.5 μL) per the method detailed in previous section, a complete CNT bridge was formed across the gap as shown in Figure 43.

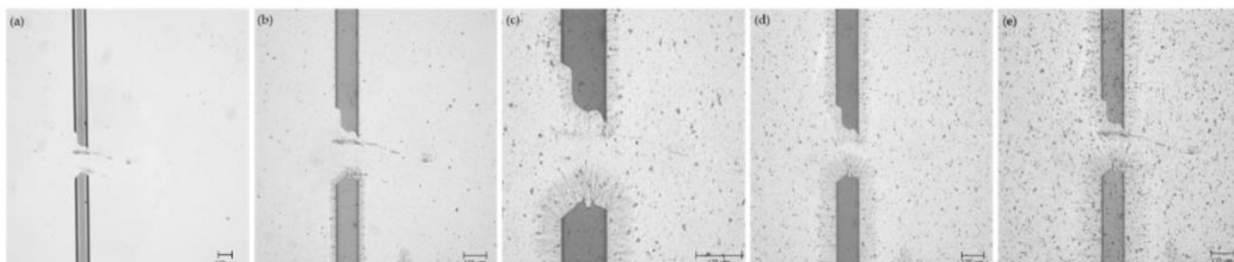

Figure 43: Fractured electrode (**a**) before CNT deposition; (**b**) after deposition of 7 μL of CNT suspension; (**c**) after 15.5 μL of CNT suspension; (**d**) after 19 μL of CNT suspension; and (**e**) after 23 μL of CNT suspension[120].

The resistance across the healed electrode was measured to be 239.6 kΩ representing a 4031% increase in resistance across the electrode. While the magnitude of this increase is large, these results serve as a successful proof of concept that the CNT bridge can be assembled across large (over 150 μm wide) gaps and restore electrical conductivity to an electrode using the electrokinetic assembly process described above.

5.3.1.5: Deposition of Polypyrrole

Using 0.9 V DC bias, PPy was successfully deposited across the CNT bridge to permanently affix it to the electrodes. Both methods for PPy deposition, as detailed in Section 2.5 were capable of covering the CNT bridge to secure it to the substrate.

In the first PPy deposition approach, the DC bias was used without changing the polarity during the deposition process. The results of this PPy deposition methodology are depicted in Figure 44. One notable feature of this PPy deposition method is the lateral growth of PPy from the side walls on the positive side of the electrode. As PPy grew towards the opposite electrode, it also grew laterally to each side of the electrode.

In the second PPy deposition methodology where the polarity of the DC bias was switched once the PPy coat reached halfway through the electrode gap, there was smaller lateral growth of PPy compared to the first PPy deposition technique (Figure 45). Therefore, depending on the intended application and desire to have larger or smaller lateral PPy coverage, either the first or second PPy deposition technique can be utilized. PPy was also deposited onto the repaired electrode that had an initial fracture as demonstrated in Figure 46.

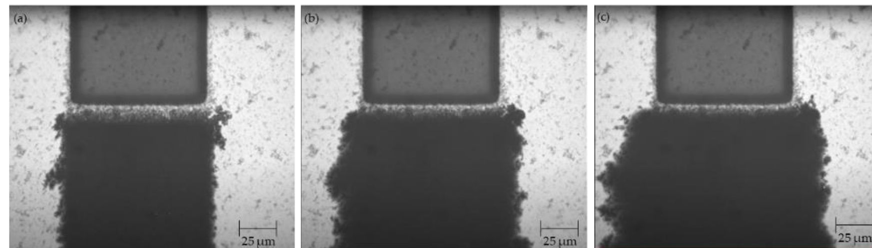

Figure 44: Results of polymer polypyrrole (PPy) deposition over the CNT bridge spanning 20 μm electrode gap without switching the polarity of 0.9 Vpp DC bias captured at approximately (**a**) 25% completion (**b**) 50% completion (**c**) 100% completion[120].

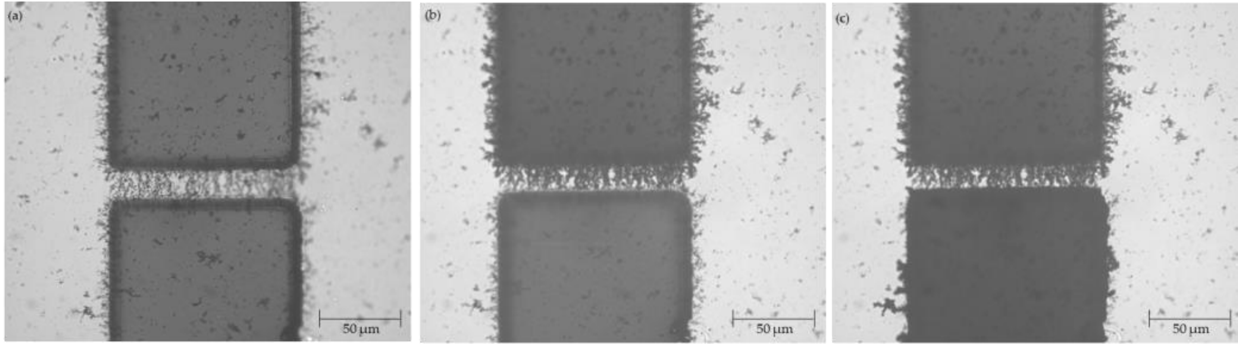

Figure 45: Results of PPy deposition over the CNT bridge spanning 20 µm electrode gap (**a**) prior to PPy application; (**b**) after the PPy deposition from the side of the top electrode reached roughly half-way through the CNT bridge and the polarity of the 0.9 Vpp DC bias was switched; (**c**) completion of PPy deposition over the CNT bridge[120].

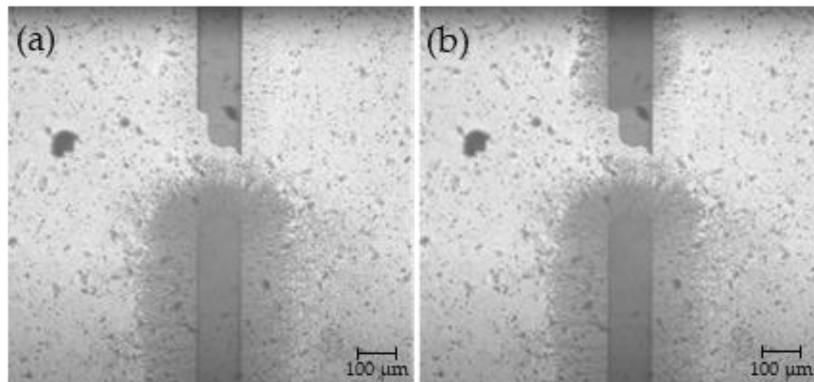

Figure 46: Results of the PPy deposition onto the CNT bridge of the healed electrode that contained a wide fracture (**a**) after the initial PPy deposition from the bottom electrode at 0.9 Vpp DC bias; (**b**) after the polarity of the DC bias was reversed[120].

5.3.2: Results of the Stress Testing of the Formed CNT Bridges

5.3.2.1: Thermal Cycling

Resistance measurements taken before and after 10 rounds of thermal cycling between 200°C and 3 °C are summarized in Table 5 below.

Table 5: Resistance measurements before and after thermal cycling[120].

Sample	Resistance before Running DI Water over Healed Electrodes (kΩ)	Resistance after Running DI Water over Healed Electrodes (kΩ)
Without PPy Coating	23.0	24.8
With PPy Coating	1.41	1.50

The CNT bridge without PPy experienced a 19% decrease in resistance as a result of thermal cycling. This is likely due to the additional evaporation that occurs as the sample is heated and the bridge expands. This additional evaporation under the influence of the surface tension forces of the shrinking liquid meniscus [117] pulls the CNTs closer together, thus reducing the CNT-to-CNT contact junction resistance. Circumstantial evidence for that suggested mechanism of the decrease in CNT-to-CNT contact resistance is offered by the fact that when the CNT bridge is covered by the PPy layer that impedes evaporation, the overall resistance did not decrease, but actually increased by 17% as a result of thermal cycling.

5.3.2.2: Placing the Healed Microelectrodes under Running Water

Resistance measurements before and after placing the samples for 30 s under a stream of deionised water (DI) with the volumetric flow rate of 0.06 LPM are summarized in Table 6 below. We can conclude that no significant increase in resistance was observed.

Table 6: Resistance measurements before and after placing the healed electrodes under the deionised water (DI) water stream[120].

Sample	Resistance before Running DI Water over Healed Electrodes (kΩ)	Resistance after Running DI Water over Healed Electrodes (kΩ)
Without PPy Coating	23.0	24.8
With PPy Coating	1.41	1.50

5.3.2.3: Exposure of the Healed Microelectrodes to Blasts of Compressed Nitrogen Gas

Resistance measurements before and after blowing nitrogen gas at 88 psi for 30 s are summarized in Table 7 below.

Table 7: Resistance measurements before and after blowing compressed nitrogen over the samples of healed microelectrodes[120].

Sample	Resistance before blowing Nitrogen over Healed Electrodes (kΩ)	Resistance after Blowing Nitrogen over Healed Electrodes (kΩ)
Without PPy Coating	23.4	23.0
With PPy Coating	1.26	1.24

There was no observed increased in resistance after blowing the compressed nitrogen gas over the samples with the healed microelectrodes.

It can be concluded from analyzing the data of the healed microelectrodes exposed to various stress tests that PPy coverage does not offer additional protection, but it does decrease overall resistance of the healed microelectrodes.

Chapter 6

Conclusion

6.1: Guided Microassembly of Latex Microbeads

In this study, the guided electrokinetic microassembly of polystyrene microparticles onto specific locations of patterned carbon microelectrodes was presented. It was discovered that AC electro-osmosis under an applied frequency of 1 kHz is sufficient to effectively agglomerate 1 μm beads in the wells, whereas a stepwise process involving the application of a 1 MHz signal, followed by a 1 kHz signal, is required for the positioning of 5 μm beads, which are mainly affected by dielectrophoretic forces. The assembly sequence is divided into two steps: guided deposition of microparticles, followed by their permanent entrapment via electropolymerization of the conductive polymer, polypyrrole. Experimental evidence and numerical simulations presented in this study demonstrate the process of the guided assembly of microparticles under the combined influence of dielectrophoretic and electro-osmotic forces. It should be noted that the influence of secondary effects, such as natural convection was neglected in our analysis. The demonstrated guided electrokinetic assembly technique has the potential to be utilized in massively parallel microassembly processes for devices employed in a wide range of applications, from biotechnology to micro- and nanoelectronics. We successfully attracted fluorophores conjugated beads by EO in to wells, and proved entrapped beads inside the wells enhanced the CTCF signal compared to the signal of unattracted beads which are distributed homogeneously in suspension.

Furthermore, the microparts to be assembled may be made of a variety of materials, such as organic and inorganic matter, dielectric, and metallic materials. Our future work will focus on the reduction of the size of the windows opened in the resist and on using various nanoparticles. We will also conduct a study on the deposition and assembly of biological cells.

6.2: Automatic Determination of the Cross-over Frequency

The cyber-physical system presented in this dissertation successfully utilized algorithmic AI and a phenomenological approach to characterize particle response to changes in the frequency of an applied non-uniform electric field. As detailed above, this approach was able to define regions of attraction and repulsion due to DEP and EO force as well as regions of weak DEP force which resulted in no bead movement. The AI-guided platform has determined that positive DEP (pDEP) is active below 500 kHz frequency, negative DEP (nDEP) is evidenced above 1 MHz frequency and the crossover frequency is between 500 kHz and 1 MHz. These results are in line with previously published experimentally determined frequency-dependent DEP behavior of the latex microbeads. The research presented in this study serves as a first proof of concept that the use of AI and closed-loop cyber-physical systems, along with a phenomenological approach, can be used to study the complex forces exerted on bodies within the micro and nano domains. Such technology can be used to enhance current microfabrication techniques, including bottom-up micro- and nano-manufacturing, and may find applications in various fields including drug delivery, micro-sensor fabrication, and bioassays. The phenomenological approach assisted by the

live AI-guided feedback loop described in the present study will assist the active manipulation of the system towards the desired phenomenological outcome such as, for example, collection of the particles at the electrodes, even if due to the complexity and plurality of the interactive forces, model-based predictions are not available. Advances in AI recognition of microbeads and various bead formations will further enhance the described phenomenological AI-guided approach to detection and control of the movement of microparticulate.

6.3: Step-wise Deposition of CNT

The present study demonstrates a novel step-wise process that incorporates electrokinetic phenomena to deposit and form long chains of CNTs along the electrical field lines of an external AC field. The deposition-drying-deposition sequence of steps allows for the creation of conductive CNT bridges between adjacent electrodes. In this work, for the first time, we demonstrate the creation of conductive CNT bridges over 50 microns in length. It has been observed that the morphologies of CNT bridges deposited at frequencies of 100 kHz and above are more orderly than for CNT bridges deposited at lower frequencies. This difference in the morphologies is attributed to the disruptive circulation of fluid caused by electroosmosis at lower frequencies. The role of postdeposition heat treatment was also explored. The observed increase in the conductivity of CNT bridges after the heat treatment step of 200 °C for 20 min is consistent with the hypothesis that the evaporating solvent and resulting surface tension pulls together CNTs and consequently decreases CNT–CNT contact resistance. Finally, electrodeposition of polypyrrole was performed to permanently secure

CNT bridges. We believe that the described step-wise electrokinetic deposition process, capable of producing long chains of conductive CNT bridges, will find applications in micro- and nanoelectronics, sensors, and energy storage and conversion.

6.4: Guided healing of damaged microelectrode via assembly of CNT

The results presented in this study establish a proof of concept that electrically conductive CNT bridges can be assembled across large electrode gaps to heal the electrodes using dielectrophoretic step-wise deposition of carbon nanotubes from the suspension. The multiphysics simulation illustrated the key concept behind the introduced electrokinetic assembly process—the self-reinforcing nature of the DEP force experienced by the CNTs as the bridge forms across the electrode gap, decreasing the effective gap distance and increasing the magnitude of the applied electric field. The relationship between the resistance of the resulting CNT bridges and the length of the gaps they span was evaluated, which confirms the dominant role played by the CNT-to-CNT contact resistance in overall bridge resistance. The present study focused on the development of technology for healing of the conventional straight microelectrodes and, if extended to healing of the closely spaced and/or interdigitated electrodes close attention should be paid to the placement of the CNT suspension droplets to avoid unintended short circuits.

While further study of the proposed electrokinetic assembly process is needed to fully understand it, the ability to create long conductive CNT bridges is an exciting prospect with many potential applications. As research into microencapsulation of self-healing agents continues to develop the self-reinforcing process presented in this paper offers impressive

benefits for the use of CNTs in such microencapsulation systems. Conceptually, if CNT suspension is microencapsulated over the electrodes, then the guided process of CNT bridge creation presented in this work can be applied for self-healing of the electrodes by the inclusion of the regime to self-test electronic trances to locate the break and then apply the required AC bias to case step-wise deposition to take place. Additionally, the described dielectrophoretic step-wise fabrication of long conductive CNT bridges will find widespread application in many fields from nanoelectronics to tissue engineering.

Bibliography

[1] M. J. Madou, *Fundamentals of Microfabrication*. 2018.

[2] A. K. Geim and K. S. Novoselov, “The rise of graphene,” *Nat. Mater.*, 2007.

[3] S. Ahmad, “Carbon nanostructures fullerenes and carbon nanotubes,” *IETE Tech. Rev. (Institution Electron. Telecommun. Eng. India)*, 1999.

[4] M. S. Dresselhaus and G. Dresselhaus, “Nanotechnology in Carbon Materials,” *Nanostructured Mater.*, 1997.

[5] L. C. Qin, X. Zhao, K. Hirahara, Y. Miyamoto, Y. Ando, and S. Iijima, “Materials science: The smallest carbon nanotube,” *Nature*, 2000.

[6] S. K. Tiwari, V. Kumar, A. Huczko, R. Oraon, A. De Adhikari, and G. C. Nayak, “Magical Allotropes of Carbon: Prospects and Applications,” *Critical Reviews in Solid State and Materials Sciences*. 2016.

[7] D. R. Dreyer, S. Park, C. W. Bielawski, and R. S. Ruoff, “The chemistry of graphene oxide,” *Chemical Society Reviews*. 2010.

[8] S. Iijima, “Helical microtubules of graphitic carbon,” *Nature*, 1991.

[9] T. Kuila, S. Bose, A. K. Mishra, P. Khanra, N. H. Kim, and J. H. Lee, “Chemical functionalization of graphene and its applications,” *Progress in Materials Science*. 2012.

[10] J. L. Delgado, M. Á. Herranz, and N. Martín, “The nano-forms of carbon,” *J. Mater. Chem.*, 2008.

[11] J. P. Salvetat *et al.*, “Elastic and shear moduli of single-walled carbon nanotube ropes,” *Phys. Rev. Lett.*, 1999.

[12] N. Grobert, “Carbon nanotubes - becoming clean,” *Materials Today*. 2007.

[13] L. de S. Vieira, “A review on the use of glassy carbon in advanced technological applications,” *Carbon*. 2022.

[14] G. M. Jenkins and K. Kawamura, “Structure of glassy carbon,” *Nature*, vol. 231, no. 5299, pp. 175–176, 1971.

[15] L. L. Ban, D. Crawford, and H. Marsh, “Lattice-resolution electron microscopy in structural studies of non-graphitizing carbons from polyvinylidene chloride (PVDC),” *J. Appl. Crystallogr.*, 1975.

[16] A. Yoshida, Y. Kaburagi, and Y. Hishiyama, “Microtexture and magnetoresistance of glass-like carbons,” *Carbon N. Y.*, 1991.

[17] P. J. F. Harris, “Fullerene-related structure of commercial glassy carbons,” *Philos.*

Mag., vol. 84, no. 29, pp. 3159–3167, 2004.

[18] R. E. Franklin, “Crystallite Growth in Graphitizing and Non-Graphitizing Carbons,” *Proc. R. Soc. A Math. Phys. Eng. Sci.*, vol. 209, no. 1097, pp. 196–218, 1951.

[19] E. I. Kurolenskin, Y. S. Lopatto, D. K. Khakimova, and Y. S. Virgul’ev, “STRUCTURE OF GLASSY CARBON.,” *Solid Fuel Chem.*, 1982.

[20] S. Berber, Y. K. Kwon, and D. Tománek, “Unusually high thermal conductivity of carbon nanotubes,” *Phys. Rev. Lett.*, 2000.

[21] S. W. Youn, M. Takahashi, H. Goto, and R. Maeda, “A study on focused ion beam milling of glassy carbon molds for the thermal imprinting of quartz and borosilicate glasses,” *J. Micromechanics Microengineering*, 2006.

[22] L. S. Pleshkova and V. I. Shesterkin, “Effect of the glassy carbon structure on the aspect ratio of micropoints of matrix field-emission cathodes prepared by thermochemical etching,” *Tech. Phys.*, 2016.

[23] M. Kuhnke, T. Lippert, E. Ortelli, G. G. Scherer, and A. Wokaun, “Microstructuring of glassy carbon: Comparison of laser machining and reactive ion etching,” in *Thin Solid Films*, 2004.

[24] O. J. A. Schneller, S. T. Brittain, and G. M. Whitesides, “Fabrication of glassy carbon microstructures by soft lithography,” *Sensors Actuators, A Phys.*, 1999.

[25] A. Singh, J. Jayaram, M. Madou, and S. Akbar, “Pyrolysis of Negative Photoresists to Fabricate Carbon Structures for Microelectromechanical Systems and Electrochemical Applications,” *J. Electrochem. Soc.*, 2002.

[26] B. Y. Park, L. Taherabadi, C. Wang, J. Zoval, and M. J. Madou, “Electrical Properties and Shrinkage of Carbonized Photoresist Films and the Implications for Carbon Microelectromechanical Systems Devices in Conductive Media,” *J. Electrochem. Soc.*, 2005.

[27] S. Ranganathan, R. McCreery, S. M. Majji, and M. Madou, “Photoresist-Derived Carbon for Microelectromechanical Systems and Electrochemical Applications,” *J. Electrochem. Soc.*, 2000.

[28] R. Martinez-Duarte, “SU-8 photolithography as a toolbox for carbon MEMS,” *Micromachines*, 2014.

[29] R. Martinez-Duarte, P. Renaud, and M. J. Madou, “A novel approach to dielectrophoresis using carbon electrodes,” *Electrophoresis*, 2011.

[30] L. Amato *et al.*, “Dense high-aspect ratio 3D carbon pillars on interdigitated microelectrode arrays,” *Carbon N. Y.*, 2015.

[31] C. Wang, L. Taherabadi, G. Jia, M. Madou, Y. Yeh, and B. Dunn, “C-MEMS for the manufacture of 3D microbatteries,” *Electrochem. Solid-State Lett.*, 2004.

[32] M. M. Wang *et al.*, “Microfluidic sorting of mammalian cells by optical force

switching," *Nat. Biotechnol.*, 2005.

[33] H. S. Min *et al.*, "Fabrication and properties of a carbon/polypyrrole three-dimensional microbattery," *J. Power Sources*, 2008.

[34] G. T. Teixidor, R. B. Zaouk, B. Y. Park, and M. J. Madou, "Fabrication and characterization of three-dimensional carbon electrodes for lithium-ion batteries," *J. Power Sources*, 2008.

[35] M. Beidaghi, W. Chen, and C. Wang, "Electrochemically activated carbon micro-electrode arrays for electrochemical micro-capacitors," *J. Power Sources*, 2011.

[36] W. Chen *et al.*, "Integration of carbon nanotubes to C-MEMS for on-chip supercapacitors," *IEEE Trans. Nanotechnol.*, 2010.

[37] H. Xu, K. Malladi, C. Wang, L. Kulinsky, M. Song, and M. Madou, "Carbon post-microarrays for glucose sensors," *Biosens. Bioelectron.*, 2008.

[38] J. I. Heo, D. S. Shim, G. T. Teixidor, S. Oh, M. J. Madou, and H. Shin, "Carbon Interdigitated Array Nanoelectrodes for Electrochemical Applications," *J. Electrochem. Soc.*, 2011.

[39] L. Amato *et al.*, "Pyrolysed 3D-carbon scaffolds induce spontaneous differentiation of human neural stem cells and facilitate real-time dopamine detection," *Adv. Funct. Mater.*, 2014.

[40] G. T. Teixidor *et al.*, "Carbon microelectromechanical systems as a substratum for cell growth," *Biomed. Mater.*, 2008.

[41] Y. Chen, "Nanofabrication by electron beam lithography and its applications: A review," *Microelectronic Engineering*. 2015.

[42] J. R. Maldonado and M. Peckerar, "X-ray lithography: Some history, current status and future prospects," *Microelectronic Engineering*. 2016.

[43] B. Wu and A. Kumar, "Extreme ultraviolet lithography: A review," *J. Vac. Sci. Technol. B Microelectron. Nanom. Struct.*, 2007.

[44] M. J. Madou, *Manufacturing Techniques for Microfabrication and Nanotechnology*. 2011.

[45] M. Itano and T. Kezuka, "Particle Adhesion and Removal on Wafer Surfaces in RCA Cleaning," in *Ultraclean Surface Processing of Silicon Wafers*, 1998.

[46] W. Kern, *Handbook of semiconductor wafer cleaning technology*. 1993.

[47] T. J. Mason, "Ultrasonic cleaning: An historical perspective," *Ultrason. Sonochem.*, 2016.

[48] J. Danglad-Flores, S. Eickelmann, and H. Riegler, "Deposition of polymer films by spin casting: A quantitative analysis," *Chem. Eng. Sci.*, 2018.

[49] S. Farjana, M. Ghaderi, S. Rahiminejad, S. Haasl, and P. Enoksson, "Dry film

photoresist-based microfabrication: A new method to fabricate millimeter-wave waveguide components," *Micromachines*, 2021.

[50] D. S. Eun *et al.*, "Photoresist spray coating for resist film performance of deep silicon cavities," *J. Korean Phys. Soc.*, 2007.

[51] R. Schnupp, R. Baumgärtner, R. Kühnhold, and H. Ryssel, "Electrodeposition of photoresist: Optimization of deposition conditions, investigation of lithographic processes and chemical resistance," *Sensors Actuators, A Phys.*, 2000.

[52] M. J. Madou, *Manufacturing Techniques for Microfabrication and Nanotechnology*. 2018.

[53] T. A. Anhoj, A. M. Jorgensen, D. A. Zauner, and J. Hübner, "The effect of soft bake temperature on the polymerization of SU-8 photoresist," *J. Micromechanics Microengineering*, 2006.

[54] K. T. M. Tran and T. D. Nguyen, "Lithography-based methods to manufacture biomaterials at small scales," *Journal of Science: Advanced Materials and Devices*. 2017.

[55] R. Martinez-Duarte and M. J. Madou, "SU-8 photolithography and its impact on microfluidics," in *Microfluidics and Nanofluidics Handbook: Fabrication, Implementation, and Applications*, 2016.

[56] A. Del Campo and C. Greiner, "SU-8: A photoresist for high-aspect-ratio and 3D submicron lithography," *J. Micromechanics Microengineering*, vol. 17, no. 6, 2007.

[57] Grégoire Genolet, "these_GenoletG.pdf," EPFL.

[58] W. H. Teh, U. Dürig, U. Drechsler, C. G. Smith, and H. J. Güntherodt, "Effect of low numerical-aperture femtosecond two-photon absorption on (SU-8) resist for ultrahigh-aspect-ratio microstereolithography," *J. Appl. Phys.*, 2005.

[59] B. Li, M. Liu, and Q. Chen, "Low-stress ultra-thick SU-8 UV photolithography process for MEMS," *J. Microlithogr. Microfabr. Microsystems*, 2005.

[60] J. D. Williams and W. Wang, "Using megasonic development of SU-8 to yield ultra-high aspect ratio microstructures with UV lithography," in *Microsystem Technologies*, 2004.

[61] J. D. Williams and W. Wang, "Study on the postbaking process and the effects on UV lithography of high aspect ratio SU-8 microstructures," *J. Microlithogr. Microfabr. Microsystems*, 2004.

[62] M. B. Cohn *et al.*, "Microassembly technologies for MEMS," in *Materials and Device Characterization in Micromachining*, 2004.

[63] C. G. Keller and R. T. Howe, "Hexsil tweezers for teleoperated micro-assembly," *Proc. IEEE Micro Electro Mech. Syst.*, pp. 72–77, 1997.

[64] J. Cecil, D. Powell, and D. Vasquez, "Assembly and manipulation of micro devices-A

state of the art survey," *Robot. Comput. Integr. Manuf.*, 2007.

[65] M. B. Cohn, Y. Liang, R. T. Howe, and A. P. Pisano, "Wafer-To-Wafer Transfer of Microsturctures for Vacuum Packaging," *Solid-State Sens. Actuator Work.*, pp. 32–35, 1996.

[66] R. J. Barsotti, M. D. Vahey, R. Wartena, Y. M. Chiang, J. Voldman, and F. Stellacci, "Assembly of metal nanoparticles into nanogaps," *Small*, 2007.

[67] J. P. Huang, K. W. Yu, G. Q. Gu, and M. Karttunen, "Electrorotation in graded colloidal suspensions," *Phys. Rev. E - Stat. Physics, Plasmas, Fluids, Relat. Interdiscip. Top.*, 2003.

[68] H. Morgan and N. G. Green, *AC electrokinetics: colloids and nanoparticles*. 2003.

[69] *Electrokinetics and Electrohydrodynamics in Microsystems*. 2012.

[70] K. Kendall, "Electromechanics of particles," *Powder Technol.*, 2002.

[71] T. M. Squires and M. Z. Bazant, "Induced-charge electro-osmosis," *J. Fluid Mech.*, 2004.

[72] N. G. Green, A. Ramos, A. González, H. Morgan, and A. Castellanos, "Fluid flow induced by nonuniform ac electric fields in electrolytes on microelectrodes. III. Observation of streamlines and numerical simulation," *Phys. Rev. E - Stat. Physics, Plasmas, Fluids, Relat. Interdiscip. Top.*, 2002.

[73] A. González, A. Ramos, N. G. Green, A. Castellanos, and H. Morgan, "Fluid flow induced by nonuniform ac electric fields in electrolytes on microelectrodes. II. A linear double-layer analysis," *Phys. Rev. E - Stat. Physics, Plasmas, Fluids, Relat. Interdiscip. Top.*, 2000.

[74] N. G. Green, A. Ramos, A. González, H. Morgan, and A. Castellanos, "Fluid flow induced by nonuniform ac electric fields in electrolytes on microelectrodes. I. Experimental measurements," *Phys. Rev. E - Stat. Physics, Plasmas, Fluids, Relat. Interdiscip. Top.*, 2000.

[75] S. Bruckenstein, "Physicochemical hydrodynamics," *Nature*, 1977.

[76] S. Sadki, P. Schottland, N. Brodie, and G. Sabouraud, "The mechanisms of pyrrole electropolymerization," *Chem. Soc. Rev.*, 2000.

[77] S. M. Sayyah, S. S. A. El-Rehim, and M. M. El-Deeb, "Electropolymerization of pyrrole and characterization of the obtained polymer films," *J. Appl. Polym. Sci.*, 2003.

[78] C. M. Li, C. Q. Sun, W. Chen, and L. Pan, "Electrochemical thin film deposition of polypyrrole on different substrates," *Surf. Coatings Technol.*, 2005.

[79] R. Pilot, R. Signorini, C. Durante, L. Orian, M. Bhamidipati, and L. Fabris, "A review on surface-enhanced Raman scattering," *Biosensors*. 2019.

[80] A. C. Lee, Y. Lee, D. Lee, and S. Kwon, "Divide and conquer: A perspective on biochips for single-cell and rare-molecule analysis by next-generation sequencing," *APL Bioengineering*. 2020.

[81] T. Zhou, J. Chen, E. Kropp, and L. Kulinsky, "Guided Electrokinetic Assembly of Polystyrene Microbeads onto Photopatterned Carbon Electrode Arrays," *ACS Appl. Mater. Interfaces*, 2020.

[82] G. G. Stokes, "On the Effect of the Internal Friction of Fluids on the Motion of Pendulums," in *Mathematical and Physical Papers*, 2010.

[83] A. Ramos, H. Morgan, N. G. Green, and A. Castellanos, "Ac electrokinetics: A review of forces in microelectrode structures," *Journal of Physics D: Applied Physics*. 1998.

[84] J. Campbell, N. R. Pollock, A. Sharon, and A. F. Sauer-Budge, "Development of an automated on-chip bead-based ELISA platform," *Anal. Methods*, 2015.

[85] ThermalFisher SCIENTIFIC, "Passive Adsorption Protocol." [Online]. Available: https://www.thermofisher.com/us/en/home/life-science/cell-analysis/qdots-microspheres-nanospheres/idc-surfactant-free-latex-beads/latex-bead-protein-coupling-protocols/passive-adsorption-protocol.html.

[86] B. Yafouz, N. A. Kadri, and F. Ibrahim, "Dielectrophoretic manipulation and separation of microparticles using microarray dot electrodes," *Sensors (Switzerland)*, 2014.

[87] T. B. Jones, "Basic Theory of Dielectrophoresis and Electrorotation," *IEEE Eng. Med. Biol. Mag.*, 2003.

[88] M. Michaels, S. Y. Yu, T. Zhou, F. Du, M. A. Al Faruque, and L. Kulinsky, "Artificial Intelligence Algorithms Enable Automated Characterization of the Positive and Negative Dielectrophoretic Ranges of Applied Frequency," *Micromachines*, 2022.

[89] B. Sarno, D. Heineck, M. J. Heller, and S. D. Ibsen, "Dielectrophoresis: Developments and applications from 2010 to 2020," *Electrophoresis*. 2021.

[90] M. Inaba, S. Hayashi, H. Li, M. Kamimura, M. Nakano, and J. Suehiro, "Dielectrophoretic properties of submicron diamond particles in sodium chloride aqueous solution," *Jpn. J. Appl. Phys.*, 2020.

[91] H. Ding *et al.*, "Particle clustering during pearl chain formation in a conductive-island based dielectrophoretic assembly system," *RSC Adv.*, 2015.

[92] V. N. Popov, "Carbon nanotubes: Properties and application," *Materials Science and Engineering R: Reports*. 2004.

[93] Y. Wang, Z. Zhou, Z. Yang, X. Chen, D. Xu, and Y. Zhang, "Gas sensors based on deposited single-walled carbon nanotube networks for DMMP detection," *Nanotechnology*, 2009.

[94] W. Xue, Y. Liu, and T. Cui, "High-mobility transistors based on nanoassembled carbon nanotube semiconducting layer and SiO2 nanoparticle dielectric layer," *Appl. Phys. Lett.*, 2006.

[95] P. Hu *et al.*, "Hysteresis suppression in self-assembled single-wall nanotube field effect transistors," *Phys. E Low-Dimensional Syst. Nanostructures*, 2008.

[96] F. Obite, G. Ijeomah, and J. S. Bassi, “Carbon nanotube field effect transistors: toward future nanoscale electronics,” *Int. J. Comput. Appl.*, 2019.

[97] M. Kaempgen, C. K. Chan, J. Ma, Y. Cui, and G. Gruner, “Printable thin film supercapacitors using single-walled carbon nanotubes,” *Nano Lett.*, 2009.

[98] G. Hills *et al.*, “Modern microprocessor built from complementary carbon nanotube transistors,” *Nature*, 2019.

[99] M. M. Shulaker *et al.*, “Carbon nanotube computer,” *Nature*, 2013.

[100] Z. Chen, Y. Yang, F. Chen, Q. Qing, Z. Wu, and Z. Liu, “Controllable interconnection of single-walled carbon nanotubes under AC electric field,” *J. Phys. Chem. B*, 2005.

[101] J. Robertson *et al.*, “Growth and characterization of high-density mats of single-walled carbon nanotubes for interconnects,” *Appl. Phys. Lett.*, 2008.

[102] L. An and C. R. Friedrich, “Process parameters and their relations for the dielectrophoretic assembly of carbon nanotubes,” *J. Appl. Phys.*, 2009.

[103] M. Duchamp *et al.*, “Controlled positioning of carbon nanotubes by dielectrophoresis: Insights into the solvent and substrate role,” *ACS Nano*, 2010.

[104] L. An and C. Friedrich, “Dielectrophoretic assembly of carbon nanotubes and stability analysis,” *Prog. Nat. Sci. Mater. Int.*, 2013.

[105] J. Li, Q. Zhang, N. Peng, and Q. Zhu, “Manipulation of carbon nanotubes using AC dielectrophoresis,” *Appl. Phys. Lett.*, 2005.

[106] H. W. Lee, S. H. Kim, Y. K. Kwak, and C. S. Han, “Nanoscale fabrication of a single multiwalled carbon nanotube attached atomic force microscope tip using an electric field,” *Rev. Sci. Instrum.*, 2005.

[107] J. S. Shim *et al.*, “The precise self-assembly of individual carbon nanotubes using magnetic capturing and fluidic alignment,” *Nanotechnology*, 2009.

[108] P. F. Wu and G. Bin Lee, “Assembly of carbon nanotubes between electrodes by utilizing optically induced dielectrophoresis and dielectrophoresis,” *Adv. Optoelectron.*, 2011.

[109] L. Zhu, Y. Sun, D. W. Hess, and C. P. Wong, “Well-aligned open-ended carbon nanotube architectures: An approach for device assembly,” *Nano Lett.*, 2006.

[110] X. Xiong, L. Jaberansari, M. G. Hahm, A. Busnaina, and Y. J. Jung, “Building highly organized single-walled-carbon-nanotube networks using template-guided fluidic assembly,” *Small*, 2007.

[111] X. Xiong *et al.*, “Directed assembly of gold nanoparticle nanowires and networks for nanodevices,” *Appl. Phys. Lett.*, 2007.

[112] H. W. Seo, C. S. Han, D. G. Choi, K. S. Kim, and Y. H. Lee, “Controlled assembly of single SWNTs bundle using dielectrophoresis,” *Microelectron. Eng.*, 2005.

[113] D. Katz, D. Lopez, A. Kornblit, and H. Grebel, "Carbon nanotubes bridges spanning across metal electrode tips," *Journal of Nanoscience and Nanotechnology*, 2008. .

[114] J. Li *et al.*, "Bottom-up approach for carbon nanotube interconnects," *Appl. Phys. Lett.*, 2003.

[115] A. Naeemi and J. D. Meindl, "Carbon nanotube interconnects," *Annual Review of Materials Research*. 2009.

[116] X. Q. Chen, T. Saito, H. Yamada, and K. Matsushige, "Aligning single-wall carbon nanotubes with an alternating-current electric field," *Appl. Phys. Lett.*, 2001.

[117] T. Zhou, E. Kropp, J. Chen, and L. Kulinsky, "Step-wise deposition process for dielectrophoretic formation of conductive 50-micron-long carbon nanotube bridges," *Micromachines*, 2020.

[118] A. Seiphoori, X. guang Ma, P. E. Arratia, and D. J. Jerolmack, "Formation of stable aggregates by fluid-assembled solid bridges," *Proc. Natl. Acad. Sci. U. S. A.*, 2020.

[119] V. H. Perez-Gonzalez, V. Ho, M. Vazquez-Pinon, S. O. Martinez-Chapa, and L. Kulinsky, "A novel micro/nano fabrication process based on the combined use of dielectrophoresis, electroosmotic flow, and electrodeposition for surface patterning," *J. Micromechanics Microengineering*, vol. 25, no. 11, 2015.

[120] T. Zhou, M. Michaels, and L. Kulinsky, "Guided healing of damaged microelectrodes via electrokinetic assembly of conductive carbon nanotube bridges," *Micromachines*, 2021.

[121] C. Schönenberger, A. Bachtold, C. Strunk, J. P. Salvetat, and L. Forró, "Interference and interaction in multi-wall carbon nanotubes," *Appl. Phys. A Mater. Sci. Process.*, 1999.

[122] *Electromagnetics Explained*. 2002.